Final Report
December 2008

IEA Wind Annex XX

HAWT Aerodynamics and Models
from Wind Tunnel Measurements

iea wind

Final Report

IEA Wind Annex XX:
HAWT Aerodynamics and Models from Wind Tunnel Measurements

Operating Agent Representative:
S. Schreck
National Renewable Energy Laboratory
National Wind Technology Center
Golden, Colorado
United States

Report Contributors:
C. Masson, École de Technologie Supérieure (ETS), Canada
J. Johansen, N. N. Sorensen, F. Zahle, C. Bak, and H.A. Madsen, Risoe DTU, Denmark
E. Politis, Centre for Renewable Energy Sources, Greece
G. Schepers, K. Lindenburg, H. Snel, Energy Research Centre, The Netherlands
R.P.J.O.M. van Rooij, E.A. Arens, G.J.W. van Bussel, G.A.M. van Kuik, F. Meng, T. Sant
Delft University of Technology, The Netherlands
A. Knauer, G. Moe, Institute for Energy Technology, NTNU, Norway
X. Munduate, A. González, E. Ferrer, S. Gomez, G. Barakos, National Renewable Energy
Centre, Spain
S. Ivanell, Gotland University and the Royal Institute of Technology, Sweden
S. Schreck, National Renewable Energy Laboratory, U.S.A.

Table of Contents

1.0 Report Introduction

1.1 Uncertainty Limits in HAWT Field-Testing

Experimental uncertainties constrain our ability to understand horizontal axis wind turbine (HAWT) aerodynamics, or to rigorously formalize understanding in accurate, reliable predictive models. Prior to undertaking Annex XX, turbine aerodynamics measurement uncertainties had been driven down substantially over the previous decade. Concurrent efforts at Netherlands Energy Research Foundation, Delft University of Technology, National Renewable Energy Laboratory, Risoe National Laboratory, and Imperial College significantly advanced the state of the art for performing research-grade measurements in the field environment. These successes in acquiring highly resolved, quantitative aerodynamic and structural measurements were fostered and documented under the auspices of IEA Wind Annex XIV and Annex XVIII.

However, improved field measurement systems and enhanced data quality further accentuated a harsh dilemma that had long confronted turbine aerodynamicists. Full-scale geometries could be densely instrumented and subsequently tested, but only in the uncontrollable and sparsely characterized inflows of atmospheric winds. Here, overriding uncertainties were introduced into the aerodynamics data by inflow fluctuations and anomalies. Alternatively, the wind tunnel environment offered controlled and uniform inflows, but at the expense of severe dynamic similarity parameter mismatches. In the wind tunnel, aggregate data uncertainties were acceptably low, but differences between experiment and field similarity parameter levels led to uncertainties regarding the validity of extrapolating otherwise high quality data to potentially dissimilar physical regimes. Thus, in years leading up to Annex XX, uncontrolled and nonuniform inflows, as well as pronounced similarity parameter level disparities had thus been deemed significant impediments to deeper comprehension of turbine aerodynamics and to further advances in turbine aerodynamics modeling capability.

1.2 Advantages of HAWT Wind Tunnel Testing

In the United States, this quandary led to plans for testing the NREL Unsteady Aerodynamics Experiment (UAE) HAWT in the NASA Ames 80 by 120 ft (24.4 m × 36.6 m) wind tunnel. This test was designed to produce accurate and reliable experimental measurements with high spatial and temporal resolution, for a realistic rotating blade geometry, under closely matched conditions of dynamic similarity, and in the presence of strictly controlled inflow conditions. To maximize test benefits, NREL convened an international scientific advisory panel consisting of wind turbine aerodynamicists and modelers from around the world. This panel provided guidance for developing a prioritized test plan to ensure that the resulting body of data would be of high quality and pertinent for attacking central issues regarding wind turbine aerodynamics and modeling. Because of concerted planning and resolute execution, this wind tunnel test was judged a decisive success at its May 2000 completion.

During this same time period, planning was initiated in Europe for a complementary wind tunnel wind turbine test designated MEXICO (Model Rotor Experiments In Controlled Conditions). The MEXICO project would acquire high quality experimental data by testing a well-instrumented model rotor of appropriate dimensions in a high-quality large wind tunnel.

MEXICO culminated in December 2006 with testing in the DNW 9.5 m × 9.5 m wind tunnel, which produced 100 GB of data high-quality turbine aerodynamics data. These data will be used to validate or adapt the aerodynamic portions of design codes based on blade element momentum theory. These data also will be used as reference data to validate next generation turbine aerodynamic models, including free vortex wake calculations and Navier-Stokes models. The NASA Ames experiment and the MEXICO project shared several key high-level goals and approaches, yet subtle distinctions enabled each experiment to compensate for limitations in the other.
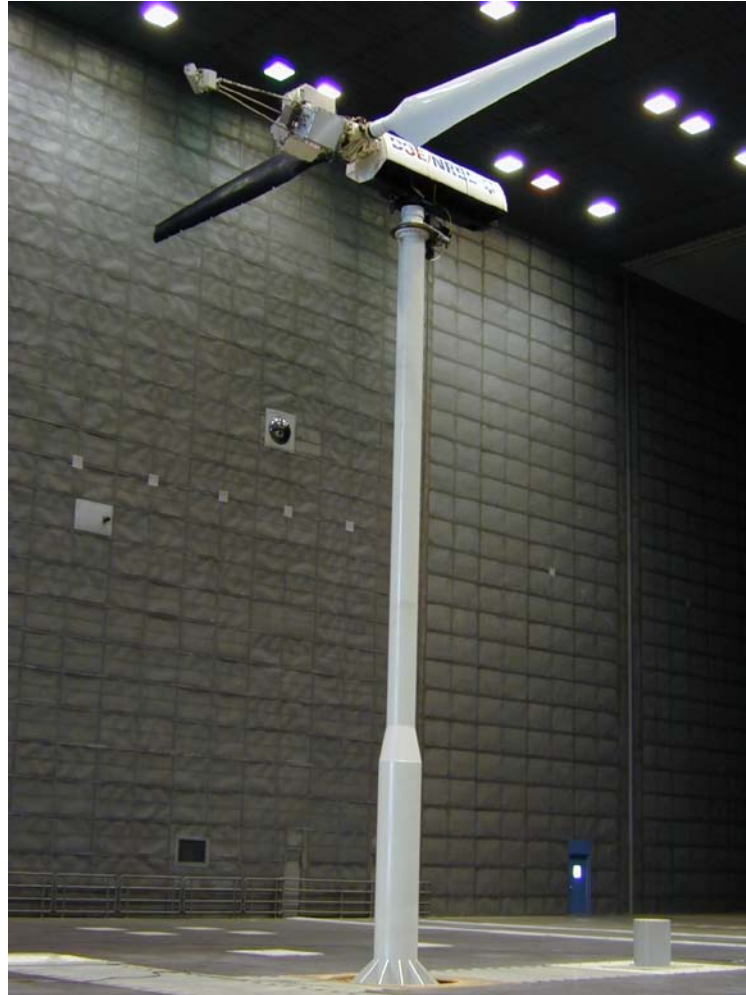
Figure 1-1. NREL UAE in NASA Ames 80 ft × 120 ft wind tunnel

1.3 Early UAE Database Findings Leading to Annex XX

Early analyses of the data acquired during the NREL UAE wind tunnel experiments in the NASA Ames 80 ft × 120 ft wind tunnel led to some findings regarding HAWT aerodynamics that previously were incompletely characterized or had remained undiscovered. Initial analyses of zero yaw aerodynamics data provided unique portrayals of rotational stall delay.

At inboard span stations, blade rotation amplified maximum normal forces to nearly three times the levels observed under nonrotating conditions. These amplified normal forces were associated with unconventional blade surface pressure distributions that have been observed infrequently in the past. In addition, detailed analyses of aerodynamics data acquired under yawed operating conditions furnished some surprising conclusions regarding the structure of the vortex generated during blade dynamic stall and responsible for force and moment augmentations. Using reconstructions of surface pressure topologies, dynamic stall vortex structure and dynamics thus inferred varied significantly along the blade span, being highly three-dimensional.

In addition to flow physics characterizations, select data were employed as a reference standard in a blind comparison exercise designed to evaluate wind turbine aerodynamics code fidelity and robustness. In this exercise, participants were given the UAE geometry and structural properties, and then attempted to predict aerodynamic response for a modest number of test cases representing diverse aerodynamic regimes. Code comparison participants did not have access to the experimental aerodynamics data until well after their model predictions were completed and submitted to NREL. Represented in the field of models were blade element momentum (BEM) models, prescribed wake models, free wake models, and Navier-Stokes codes. Model predictions were requested for axisymmetric operation, in which rotational stall delay is strongly manifest, and for yawed operation, wherein dynamic stall predominates. In general, results showed unexpectedly large margins of disagreement between the predicted and measured data. In addition, no consistent trends were apparent regarding the magnitudes or the directions of these deviations. Altogether, these early findings resulted in the Annex XX organizational structure documented here.

1.4 Research Thrust Areas

Annex XX encompassed the four research thrust areas summarized in the subsections that follow. Participants did not address all four areas nor did they proceed in a strictly sequential manner. Rather, because of the magnitude and complexity of the research tasks, participants undertook various subsets of the four areas and carried them out in ways best suited to individual research objectives.

1.4.1 Data Acquisition, Processing, and Quality Assurance
The raw data acquired during the UAE test in the NASA Ames 80 ft × 120 ft were reduced to engineering units data and were readily accessible in that form. In response to studies in conjunction with Annex XX, however, reprocessing to alternate formats occasionally was deemed advantageous or necessary. In addition, Annex XX research occasionally identified areas of HAWT aerodynamics that could benefit from supplementary experiments to complement the existing NREL UAE wind tunnel database. Regardless of the source of the data used in Annex XX, participants carried out uncertainty analyses of the data to establish error bounds before proceeding with their actual research.

1.4.2 Data Analysis and Exploitation
Once participants obtained the desired data, converted them to the desired format, and established uncertainties, data analysis and exploitation began. To facilitate flow field

comprehension, data were analyzed in a physically pertinent or rationally motivated manner that disclosed key flow physics. This analysis task posed a nontrivial challenge because of the inherent complexity of HAWT aerodynamics as well as the sheer volume of data in the UAE wind tunnel database. Because of these complexities, participants found it beneficial to construct software specifically for exploring, displaying, and analyzing database files. This enabled compiling quantitative and qualitative knowledge concerning turbine flow physics.

1.4.3 Model Subcomponent Construction or Modification

Having knowledge of the HAWT flow field gained through data analysis and exploitation, a central thrust of Annex XX was the formalization this knowledge in physics physics-based computational model subcomponents. Some participants constructed novel subcomponent models based on data analysis and exploitation, while others modified existing subcomponent models. Flow physics knowledge gained through data analysis and exploitation not only enabled model subcomponent construction, but also conferred enhanced robustness on these subcomponents. Finally, participants used UAE wind tunnel data, or data derived via analysis and exploitation in conjunction with this Annex, to validate new or modified subcomponent accuracy and reliability.

1.4.4 Subcomponent Integration and Model Validation

Once constructed and validated in isolation from other model subcomponents and code segments, the new or modified subcomponents were integrated into models. Then, the comprehensive software packages were validated, again using the UAE wind tunnel database. Global validation studies sought to establish bounds on accuracy or reliability or to quantify pertinent sensitivities to input quantities or model parameters. Validated codes were used to study turbine flow physics or for design and analysis.

1.5 Unsteady Aerodynamics Experiment Wind Tunnel Database

Below is a very abbreviated description of the UAE wind tunnel database. This brief description contains short summaries of the data sequences available in the database and an illustrated example of website appearance and operation. For complete information, please see Hand et al. (2001).

1.5.1 Sequences 8 and 9: Downwind Sonics and Downwind Sonics Parked

This test sequence used an upwind, rigid turbine with a 0° cone angle. The wind speed ranged from 5 to 25 m/s. Yaw angles of 0° to 60° were achieved, and the blade tip pitch was 3°. The rotor rotated at 72 RPM during Sequence 8, but was parked during Sequence 9. Blade pressure measurements were collected. The five-hole probes were removed and the plugs were installed. Plastic tape 0.03 mm thick was used to smooth the interface between the plugs and the blade. Teeter dampers were replaced with rigid links, and these two channels were flagged as not applicable by setting the measured values in the data file to −99999.99 Nm. The teeter link load cell was pretensioned to 40,000 N. During postprocessing, the probe channels were set to read −99999.99.

Sonic anemometers were mounted on a strut downwind of the turbine. The strut was mounted to the *T*-frame, which was rotated to align the anemometers aft of the 9% and 49% radius locations at hub height. Because of this configuration, the tunnel balance data are considered

invalid. Sequence 9 was designed to compare the downwind sonic anemometer readings with the upwind sonic anemometers without interference from the turbine. The rotor was parked with the instrumented blade at 0° azimuth. All pressure measurements obtained in Sequence 9 are invalid because sufficient time for temperature stabilization did not occur; thus all associated data values were flagged as not applicable by setting the measured values in the data file to 0.0000 Pa.

1.5.2 Sequences B and D: Downwind Baseline and Downwind High Pitch

This test sequence used a downwind, teetered turbine with a 3.4°cone angle. The wind speed ranged from 5 to 25 m/s. Yaw angles of ±180° were achieved at low wind speeds, and yaw angles of –20° to 10° were achieved for high wind speeds. The blade tip pitch was 3° for sequence B and 6°for sequence D. These two sequences were interleaved during testing because the turbine operator could easily change the pitch angle change. The rotor rotated at 72 RPM. Blade and probe pressure measurements were collected.

1.5.3 Sequence F: Downwind High Cone

This test sequence used a downwind, rigid turbine with an 18° cone angle. The wind speed ranged from 10 m/s to 20 m/s. Excessive inertial loading caused by the high cone angle prevented operation at lower wind speeds. Yaw angles of ±20° were achieved, and blade tip pitch was 3°. The rotor rotated at 72 RPM. Blade and probe pressure measurements were collected. The teeter dampers were replaced with rigid links, and these two channels were flagged as not applicable by setting measured values in the data file to –99999.99 Nm. The teeter link was replaced with a shorter bar so the load cell was not installed during this test. The teeter link load cell channel was flagged as not applicable by setting the measured values in the data file to –99999.99 N.

1.5.4 Sequence G: Upwind Teetered

Test sequence G used an upwind, teetered turbine with a 0° cone angle. The wind speeds ranged from 5 to 25 m/s. Yaw angles of ±180° were achieved at low wind speeds and angles of ±10° were achieved at the high wind speeds. The blade tip pitch was 3°. The rotor rotated at 72 RPM. Blade and probe pressure measurements were collected.

1.5.5 Sequences H, I, and J: Upwind Baseline, Low Pitch, and High Pitch

This test sequence used an upwind, rigid turbine with a 0° cone angle. The wind speed ranged from 5 to 25 m/s. Yaw angles of –30° to 180° were achieved at low wind speeds, and angles of ±10° were achieved for high wind speeds. The blade tip pitch was 3° for sequence H, 0° for sequence I, and 6° for sequence J. These three sequences were interleaved during testing because the turbine operator could easily change the pitch angle. The rotor rotated at 72 RPM. Blade and probe pressure measurements were collected. The teeter dampers were replaced with rigid links, and these two channels were flagged as not applicable by setting the measured values in the data file to –99999.99 Nm. The teeter link load cell was pretensioned to 40,000 N. In addition to the standard 30-second campaigns, yaw sweeps were done at 7 and 10 m/s. These 6-minuteute campaigns were collected while the yaw drive rotated the turbine 360° at a rate of 1°/s. The file names for these campaigns use the letter designation, followed by two digits for wind speed, followed by YS, followed by 000.

1.5.6 Sequence M: Transition Fixed
Test sequence M used an upwind, rigid turbine with a 0° cone angle. The wind speed ranged from 5 to 15 m/s. Yaw angles ranged from 0° to 90°, and the blade tip pitch was 3°. The rotor rotated at 72 RPM. Blade pressure measurements were collected. The five-hole probes were removed and the plugs were installed. Plastic tape 0.03 mm thick was used to smooth the interface between the plugs and the blade. The teeter dampers were replaced with rigid links, and these two channels were flagged as not applicable by setting the measured values in the data file to –99999.99 Nm. The teeter link load cell was pretensioned to 40,000 N. During post-processing, the probe channels were set to read –99999.99. Zigzag tape was installed near the leading edge of the instrumented blade on both the upper and lower surfaces as described in Appendix K of Hand, et al. (2001). In addition to the standard 30-second campaigns, yaw sweeps were done at 7 and 10 m/s. These 90-second campaigns were collected while the yaw drive rotated the turbine 90° at a rate of 1°/s. The file names for these campaigns use the letter designation, followed by two digits for wind speed, followed by YSU, followed by 00.

1.5.7 Sequences S and U: Upwind, No Probes; Upwind 4° Pitch
This test sequence used an upwind, rigid turbine with a 0° cone angle. The wind speed ranged from 5 to 25 m/s. Yaw angles of 0° to 180° were achieved for Sequence S, but the yaw angle remained at 0° for Sequence U. The blade tip pitch was 3° for Sequence S and 4° for Sequence U. These three sequences were interleaved during testing because the pitch angle change was easily made by the turbine operator. The rotor rotated at 72 RPM. Blade pressure measurements were collected. The five-hole probes were removed and the plugs were installed. Plastic tape 0.03 mm thick was used to smooth the interface between the plugs and the blade. The teeter dampers were replaced with rigid links, and these two channels were flagged as not applicable by setting the measured values in the data file to –99999.99 Nm. The teeter link load cell was pretensioned to 40,000 N. During postprocessing, the probe channels were set to read –99999.99. In addition to the standard 30-second campaigns, yaw sweeps were done at 7 and 10 m/s for the Sequence S configuration. These 6-minute campaigns were collected while the yaw drive rotated the turbine 360° at a rate of 1°/s. The file names for these campaigns use the letter designation, followed by two digits for wind speed, followed by YSU, followed by 00.

1.5.8 Sequence V: Tip Plate
This test sequence used an upwind, rigid turbine with a 0° cone angle. The wind speed ranged from 5 to 25 m/s, and the yaw angle was held at 0°. The blade pitch angle was 3°. The rotor rotated at 72 RPM. Blade pressure measurements were collected. The five-hole probes were removed and the plugs were installed. Plastic tape 0.03 mm thick was used to smooth the interface between the plugs and the blade. The teeter dampers were replaced with rigid links, and these two channels were flagged as not applicable by setting the measured values in the data file to –99999.99 Nm. The teeter link load cell was pretensioned to 40,000 N. During postprocessing, the probe channels were set to read –99999.99. The standard tip blocks were replaced with a tip plate to simulate the effect of an undeployed tip-mounted aerodynamic brake as shown in Appendix A. of Hand, et al. (2001). Note that the blade radius was not changed during postprocessing, so the pressure tap locations are at the same radial location,

but the reference to 30% represents 30% of 5.029 m not 4.943 m. Throughout this report, references to the blade span are made for the 5.029-m radius, not the 4.943-m radius.

1.5.9 Sequence W: Extended Blade

This test sequence used an upwind, rigid turbine with a 0° cone angle. The wind speed ranged from 5 to 21 m/s, and the yaw angle was held at 0°. The blade pitch angle was 3°. The rotor rotated at 72 RPM. Blade pressure measurements were collected. The five-hole probes were removed and the plugs were installed. Plastic tape 0.03 mm thick was used to smooth the interface between the plugs and the blade. Rigid links replaced The teeter dampers were replaced with rigid links, and these two channels were flagged as not applicable by setting the measured values in the data file to –99999.99 Nm. The teeter link load cell was pretensioned to 40,000 N. During postprocessing, the probe channels were set to read –99999.99. The standard tip blocks were replaced with blade extensions that created a 5.532-m radius rotor as shown in Appendix A of Hand, et al. (2001). The extension used the S809 airfoil throughout, and the linear taper of the blade continued along the extension. Note that the blade radius was not changed during postprocessing, so the pressure tap locations are at the same radial location, but the reference to 30% represents 30% of 5.029 m not 5.532 m. Throughout this report, references to the blade span are made for the 5.029-m radius, not the 5.532-m radius.

1.5.10 Sequence X: Elevated RPM

This test sequence used an upwind, rigid turbine with a 0° cone angle. The wind speed ranged from 5 to 12 m/s, and yaw angles of ±30° were obtained. The blade pitch angle was 3°. The rotor rotated at 90 RPM. Blade pressure measurements were collected. The five-hole probes were removed and the plugs were installed. Plastic tape 0.03 mm thick was used to smooth the interface between the plugs and the blade. The teeter dampers were replaced with rigid links, and these two channels were flagged as not applicable by setting the measured values in the data file to –99999.99 Nm. The teeter link load cell was pretensioned to 40,000 N. During postprocessing, the probe channels were set to read –99999.99. The hydrostatic correction derived for operation at 72 RPM as described in Appendix F was applied to these data.

1.5.11 Example of UAE Wind Tunnel Database Website User Session

Figure 1-2 shows the web page first seen by a user when entering the NREL Unsteady Aerodynamics Experiment database web site. Each of the 15 links shown on this page corresponds to an entire data sequence, each of which includes several individual data files. Clicking on any of the 15 links takes the user directly to the web page for that data sequence.

Figure 1-2. Web page first seen when entering the NREL Unsteady Aerodynamics Experiment database web site.

Figure 1-3 depicts the page that a user would access by clicking on the "(H) Upwind Baseline" link on the page in Figure 1-2. This data sequence contains more data files than any other sequence, and so presents a good example of the manner and effectiveness of the database organization. It is easy for the user to find the conditions they want and to click on the corresponding link to access the desired file.

NREL's National Wind Technology Center
Unsteady Aerodynamics Experiment Database

Sequence H Configuration Selection

Select the desired configuration:

Nominal WS (m/s)	0	5	10	20	30	45	60	75	90	135	180	-135	-90	-75	-60	-50	-45	-40	-30	-20	-10	-5
5.0	0 1	0	0	0	0	0	0	0	0	0	0								0		0	0
6.0	0 1		0		0																	
7.0	0 1	0	0	0	0	0	0	0	0	0	0								0		0	0
8.0	0 1		0		0																	
9.0	0 1		0	0	0		0															
10.0	0 1	0	0	0	0	0	0	0	0	0	0								0		0	0
11.0	0 1		0	0	0		1															
12.0	0 2		0		0																	
13.0	0 1		0	0	0		0															
14.0	0 1		0		0																	
15.0	0 1	0	0	0	0	0	0	0	0	0	0								0		0	0
16.0	0 1		0		0																	
17.0	0 1		0	0	0																	
18.0	0 1		0																			
19.0	3 4		1	1																		
20.0	2 3	1	2																		0	0
21.0	0 1		0																			
22.0	0 1		0																			
23.0	0 1																					
24.0	0 1																					
25.0	0 1																					

Note: Digits within table indicate configuration repetition number.

[NREL] [UAEWT Home] [UAEWT Sequence]

Figure 1-3. Web page accessed by clicking on the "(H) Upwind Baseline" link on the page in Figure 1-2

Clicking the link corresponding to 10 m/s and 60° yaw would lead to the web page shown in Figure 1-4. On this web page, the user can select the channels that they want to download and designate these using the check boxes.
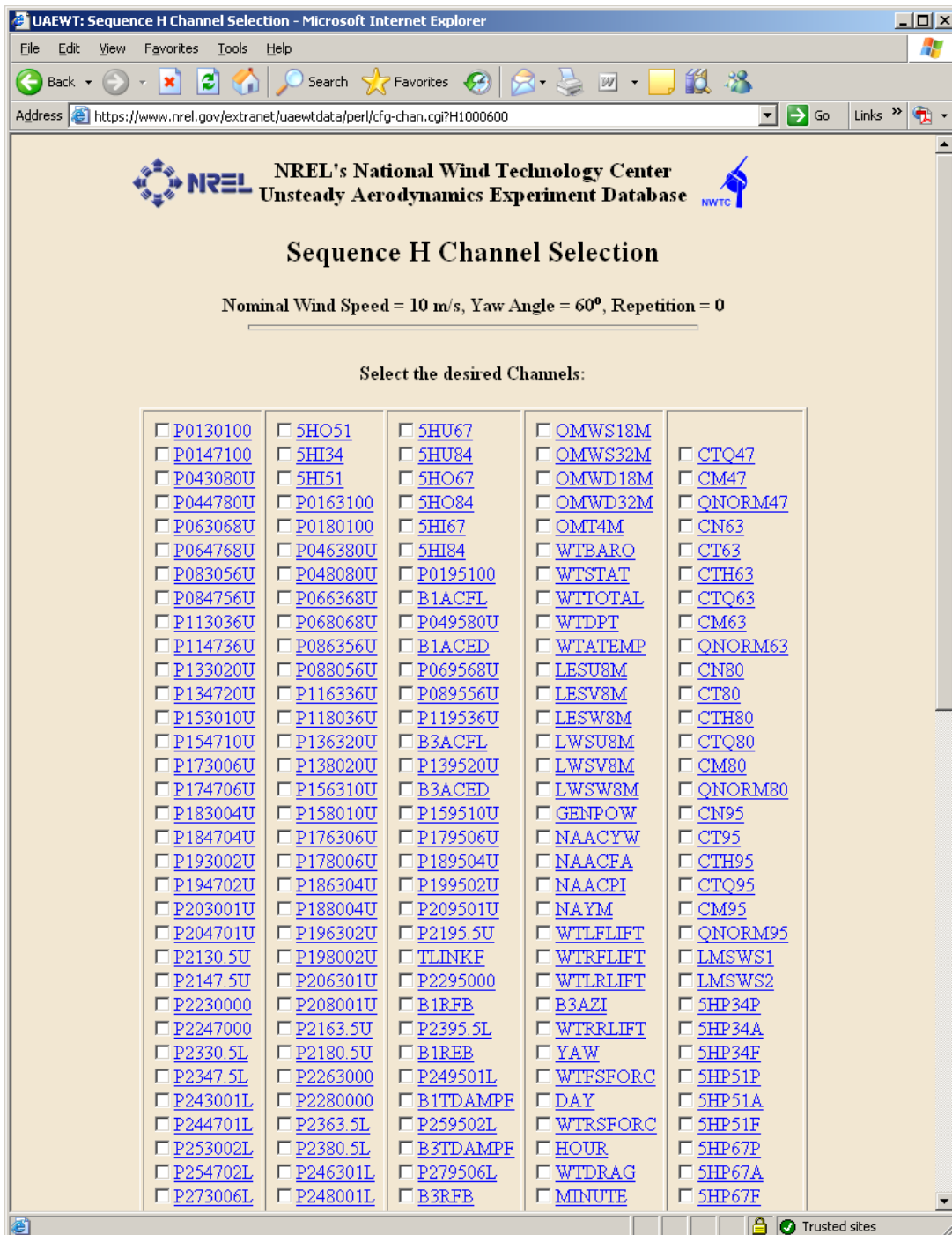

Figure 1-4(a). Web page accessed by clicking the link corresponding to 10 m/s and 60° yaw on the web page shown in Figure 1-3.

After selecting the desired channels using the check boxes, the user then has the option to download 1) entire raw channel selection, 2) channel average, 3) cycle average, or 4) azimuth average. In addition, the user may choose whether they want the file delivered to them as ASCII text or as a ZIP compressed file.

UAEWT: Sequence H Channel Selection - Microsoft Internet Explorer

File   Edit   View   Favorites   Tools   Help

Back   Search   Favorites

Address https://www.nrel.gov/extranet/uaewtdata/perl/cfg-chan.cgi?H1000600   Go   Links »

P2347.5L	P2263000	P249501L	WTFSFORC	5HP51P
P243001L	P2280000	B1TDAMPF	DAY	5HP51A
P244701L	P2363.5L	P259502L	WTRSFORC	5HP51F
P253002L	P2380.5L	B3TDAMPF	HOUR	5HP67P
P254702L	P246301L	P279506L	WTDRAG	5HP67A
P273006L	P248001L	B3RFB	MINUTE	5HP67F
P274706L	P256302L	P309514L	YAWTABLE	5HP84P
P303014L	P258002L	B3REB	SECOND	5HP84A
P304714L	P276306L	P329528L	MILLISEC	5HP84F
P323028L	P278006L	LSSXXB	YAWERR	5HP91P
P324728L	P306314L	P349544L	TEETER	5HP91A
P343044L	P308014L	LSSYYB	CONE	5HP91F
P344744L	P326328L	P369568L	RPM	VTUN
P363068L	P328028L	LSSTQ	CYCLECNT	QTUN
P364768L	P346344L	P389592L	EAEROTH	RHOTUN
P383092L	P348044L	B1PRATE	EAEROTQ	PTTUN
P384792L	P366368L	P189204U	EAERORFB	PSTUN
P183604U	P368068L	P189804U	ETEEMRFB	PATUN
P185204U	P386392L	B3PRATE	LSSTQCOR	WTLIFTF
P184104U	P388092L	P119236U	LSSHB	WTPITCHM
P185804U	P186904U	P119836U	LSSVB	WTSIDEF
P113636U	P188504U	B1FLAP	ROTPOW	WTYAWM
P115236U	P187404U	5HC91	MENSOR	WTROLLM
P114136U	P189004U	B1PITCH	CN30	ANYERR
P115836U	P116936U	5HL91	CT30	ERR36C
5HC34	P118536U	B3FLAP	CTH30	ERR4C
5HC51	P117436U	5HU91	CTQ30	ERR95
5HL34	P119036U	B3PITCH	CM30	ERR80
5HL51	5HC67	5HO91	QNORM30	ERR63
5HU34	5HC84	MENS1	CN47	ERR47
5HU51	5HL67	5HI91	CT47	ERR30
5HO34	5HL84	MENS2	CTH47	

- Entire raw channel selection
- Channel average
- Cycle average
- Azimuth average

ASCII Text or ZIP Compressed

Reset   Submit

[NREL] [UAEWT Home] [UAEWT Sequence] [Seq H Config]

Trusted sites

Figure 1-4(b). Continuation of web page begun in Figure 1-4(a).

11

1.6 Administration and Management

The following administrative and managerial provisions were established at annex inception, and were observed throughout the life of the annex. All provisions were consistent with IEA policies and regulations, and were responsive to IEA Wind Executive Committee oversight and direction.

1.6.1 Operating Agent Duties

The National Wind Technology Center (NWTC) of NREL was not the Contracting Party, but accepted the rights and powers and carried out the obligations and functions of the Operating Agent as provided in the IEA Wind Implementing Agreement. Principal Operating Agent duties consisted of the following:

- Establishing and managing the NREL UAE wind tunnel experiment database.

- Organizing annual technical meetings in cooperation with the host country representative, which were attended by participating researchers.

- Preparing semiannual reports regarding Annex XX scientific progress and administrative status, which were submitted to the IEA Wind Executive Committee.

1.6.2 Participating Countries

To be eligible to participate in Annex XX, countries were required to be members of the IEA Wind Implementing Agreement. Of those who were members of the agreement and thus eligible, the following eight countries elected to participate in Annex XX: Canada, Denmark, Greece, the Netherlands, Norway, Spain, Sweden, and the United States.

1.6.3 Funds Received and Expended

Principal costs associated with Annex XX were those for Operating Agent salary, travel, and operating expenses. The three year aggregate Operating Agent budget that was approved for Annex XX is as follows:

Salaries	3.0 person-months	$ 64,500
Travel	3 meetings travel	$ 9,000
Expenses	publishing, mailing	$ 1,500
TOTAL		$ 75,000

These Operating Agent costs were paid jointly and in equal shares by the eight countries participating in Annex XX. During 2004, 2005, and 2006, participating countries paid $57,543. Combined with the three year NREL Operating Agent cost share of $9,375, this brings total receipts for the life of Annex XX to $66,918. Total receipts fell short of $75,000 because program priorities and funding commitments for some participating countries precluded them from contributing as originally projected. By the end of December 2007, the Operating Agent had expended the entire amount of $66,918 to defray the costs of annex administration.

In addition to costs for Operating Agent administration and management, each of the eight participating countries paid their own costs for carrying out research under Annex XX, including reporting and travel expenses. Each year, the country hosting the annual technical progress meeting paid the costs associated with holding the meeting.

1.6.4 Intellectual Property

For purposes of Annex XX, proprietary information consisted of information of a confidential nature, such as trade secrets and know-how appropriately identified as such. During the course of Annex XX, no proprietary information was produced or maintained by the Operating Agent or any of the participants. Similarly, no patentable inventions were made or conceived in the course of or under Annex XX.

The NWTC as part of NREL owns and will continue to maintain the UAE wind tunnel database, and will continue to distribute data from it to former Annex XX participants as well as other researchers who need the data. Data will continue to be available from the UAE wind tunnel database website and directly from the Operating Agent Representative, Scott Schreck (scott_schreck@nrel.gov). Those who wish to request data should first consult Hand et al. (2001), which gives an excellent description of the test and the resulting data.

1.6.5 Research Documentation

Participants constructed or modified model subcomponents and integrated codes during Annex XX. Although they documented methodologies and results in detail, generally they did not exchange actual software.

All studies, assessments, analyses, and evaluations carried out in conjunction with Annex XX were formally documented. Each participant prepared at least one report a year during the Annex, and these reports were made available to all participants.

Most importantly, annex research was thoroughly and credibly documented in numerous journal articles, conference papers, laboratory reports and dissertations, which are listed in this report in the summaries provided by each of the participating countries.

In addition to these individual reports, semiannual summaries of Annex activities were submitted to the IEA Wind Executive Committee by the Operating Agent Representative.

1.7 Reference

Hand, M.; Simms, D.; Fingersh, L.; Jager, D.; Cotrell, J.; Schreck, S.; Larwood, S. (December 2001). "Unsteady Aerodynamics Experiment Phase VI: Wind Tunnel Test Configurations and Available Data Campaigns," NREL/TP-500-29955. Golden, CO: NREL. Available at http://www.nrel.gov/docs/fy02osti/29955.pdf.

2.0 Research Summary—Canada

Organization: École de Technologie Supérieure (ETS), Mechanical
Engineering Department

Researcher: Christian Masson, christian.masson@etsmtl.ca

2.1 Background and Motivation

One weakness of numerical models for analyzing wind turbine aerodynamics lies in their limited capacity to take account adequately of the induction of the wind turbine wake on the blade aerodynamics. The main objective is to improve the representation of the blade aerodynamics in Navier-Stokes/actuator disk approach by extending it to an actuator-surface model in which wake induction is naturally taken into account instead of using tip loss factor models. In the actuator-surface model, singular surfaces represent the action on the flow of the rotor blades. These surfaces are porous, have zero thickness, and carry velocity and pressure jumps. The shape and movement of these surfaces depend in fact on the object of analysis: a fixed conical disk is used for wind turbine rotor analysis in the framework of actuator disk-type analysis, and planar surfaces in rotation are used in the framework of actuator-surface analysis. Velocity jumps are prescribed so that circulation of velocity respects important physical relations linked to lift force and vorticity conservation. In the Navier-Stokes equations, this will be guaranteed by including additional surface and volume forces. These features of actuator surfaces will allow accounting for the effects of tip vortices while respecting the local physics of the flow. Using a tip loss factor in classical blade element momentum (BEM) integral methods has a similar effect. However, it is derived from a unique configuration of a turbine (zero yaw, ideal wake) that may not correspond to any configuration and loading of a rotor.

2.2 Data Used and Methods Employed

Detailed experimental data gathered when testing the National Renewable Energy Laboratory (NREL) Unsteady Aerodynamics Experiment (UAE) in the NASA Ames 80 ×120 ft wind tunnel supported developing proposed mathematical models and numerical methods and their validations.

The method developed involves a spatial resolution capable of efficiently studying the range of scales from the turbine wakes to the atmospheric boundary layer. This approach encompasses spatial resolutions between very high resolution computational fluid dynamics (CFD) modeling suitable for three-dimensional separated flow in the vicinity of the blade, and large-scale modeling typically used to model the atmospheric boundary layer over topography. The method combines the Navier-Stokes solver with the actuator-disk approach. It has been used in various wind turbine configurations, including light and strong yaw angles, dynamic inflow, rapid blade pitch changes, and rotor/tower interactions. In addition, this method has been extended to model the turbulent flow field around the turbine using a two-equation closure model to study wind turbine interactions within a wind park in stable, neutral, or unstable atmospheric conditions.

Adapting the method to modeling actuator surfaces requires prescribing the velocity jumps along one wing or blade using the spanwise lift distribution, which is calculated using blade element theory: for a blade section, simple analysis of local flow components raise values of local wind speed and angle of attack which are then used, based on experimental results—two-dimensional characteristics of the same airfoil for the simpler estimate—to derive lift values. Numerical methods based on control-volume approaches have been developed to study 2D or 3D problems. Specific contributions to the numerical methods are specialized treatments for the velocities and pressure discontinuities as well as second-order models for computing convection fluxes.

2.3 Research Results

The first results obtained have demonstrated and validated satisfactorily the new model against elementary problems for which an analytical solution is available: continuous loading of vorticity on a segment or on an actuator disk (2D) and finite wings with different shapes immersed in uniform inflow. The recent application of the model to a wind turbine using rotating surfaces has shown that the new model increases accuracy in calculating the wake induction on the blade aerodynamics compared to models based on the actuator disk representation.

2.4 Conclusions and Future Work

Future results will be produced for other case studies of wind turbines and comparisons with other models of wind turbine aerodynamics will hopefully raise interesting conclusions about the new model proposed. This model is expected to be used to study the wind turbine wake with more attention, especially regarding the far wake development (one rotor diameter downstream and more).

2.5 Bibliography

Leclerc, C.; Masson, C. (2004). "Wind Turbine Performance Predictions using a Differential Actuator Disk Modeling." Prepared for the Special Topic Conference of EWEA: The Science of Making Torque from Wind, Delft, Netherlands, April 2004.

Leclerc, C.; Masson, C. (2005). "Wind Turbine Performance Predictions using a Differential Actuator Disk Modeling," *Journal of Solar Energy Engineering* (127:2); 200–208.

Sibuet-Watters, C.; Masson, C. (2007). "Recent Advances in Modeling of Wind Turbine Wake Vortical Structure Using a Differential Actuator Disk Theory." Prepared for the Science of Making Torque from Wind Conference. *Journal of Physics*: Conference Series 75, doi:10.1088/1742-6596/75/1/012037.

3.0 Research Summary—Denmark

Organization:	Risoe DTU Department of Wind Energy
Researchers:	Jeppe Johansen, jeppe.johansen@risoe.dk
	Niels N. Sørensen, niels.soerensen@risoe.dk
	Frederik Zahle, frederik.zahle@risoe.dk
	Christian Bak, christian.bak@risoe.dk
	Helge Aa. Madsen, helge.aagaard.madsen@risoe.dk

3.1 Background and Motivation

The research has been within two main areas: one on computational fluid dynamics (CFD) modeling and one on developing and validating the aerodynamic engineering models in the aeroelastic codes HAWC and HAWC2 and correcting the airfoil data to be used in these codes.

3.1.1 CFD Background and Objectives

Risoe has for the last 15 or more years been developing CFD methods for wind turbine rotor aerodynamics, and a critical bottleneck has been the lack of detailed high quality experimental data for verification. Thanks to the National Renewable Energy Laboratory/National Aeronautics and Space Administration (NREL/NASA) Ames wind tunnel experiment, this picture has now changed. Risø participated in the NREL Blind Code Comparison, and the CFD method showed some very promising results for the upwind zero yaw computations. Since then, a large effort has been dedicated to comparisons to the NREL/NASA Ames data released after the blind comparison.

The objectives of participating in IEA Wind Annex XX were twofold: First, we wanted to improve and validate our Navier-Stokes CFD solver, both the standard Reynolds Averaged Navier-Stokes (RANS) approach and the Detached Eddy Simulation (DES) methods. Second, the details of the CFD simulations are complementary to the wind tunnel data and would provide additional insight that would help interpret the available measurements. In this respect the CFD method is one of the only methods used with wind energy that directly produces pressure data.

3.1.2 Engineering Models Background and Objectives

Aerodynamics and aeroelasticity of horizontal axis wind turbines (HAWT) is a key research area in the Department of Wind Energy at Risoe DTU. A combination of theoretical and experimental research activities is considered vital to improving the modeling tools. Risoe DTU thus conducted a comprehensive field rotor experiment from 1987 to 1993 and sent the data to the database established within Annex XIV and Annex XVIII, in which Risoe DTU participated. With the field rotor data it was possible to qualify and to some extent quantify the importance of three dimensional and unsteady effects on a HAWT rotor in stall. The turbulent inflow inherent in these experiments, however, complicated interpreting the data. Therefore the new NREL data set acquired in a wind tunnel constitutes an excellent completion of the field rotor data for further development and validation of engineering aerodynamic submodels.

The main objective was to further develop and validate the engineering aerodynamic models in the aeroelastic codes HAWC and HAWC2. The following models were considered:

- Model for delayed stall on the inner part of the blade

- Model for unsteady blade section aerodynamics – dynamic stall model

- Tip correction model

- Model for correction of induction in yawed flow

- Model for tower influence upstream as well as downstream.

3.2 Data Used and Methods Employed

Standstill. The UAE data were used to determine aerodynamics of a blade during standstill in comparison with computed results using the EllipSys3D code. Both steady blades (fixed angles of attack) and pitching blades (dynamic stall) at low and high angles of attack have been analyzed. Turbulence was modeled using both k-ω Shear-Stress Transport (SST) and DES models.

Uniform inflow conditions. The UAE data in the uniform upwind configuration have been used for validating the EllipSys3D code based on comparisons with surface pressure measurements and low-speed-shaft torque. Different turbulence models have been applied, including and Wilcox's k-ω model, Menter's k-ω SST model, and the DES turbulence model.

3D corrected airfoil data. Fully converged CFD solutions of the flow around the NREL Phase VI rotor using EllipSys3D were used to develop a new method for determining axial and tangential induction factors. Together with the sectional normal and tangential forces and local twist, airfoil characteristics C_l and C_d have been determined and applied in a standard blade element momentum method. Excellent agreement was obtained.
Investigators analyzed the pressure distributions from the measurements and compared them to measurements from 2D wind tunnel tests. An analytical model describing the difference between the pressure distributions from the two kinds of measurements made 3D corrections on 2D airfoil data. The model was validated against power and thrust for the NREL Phase VI turbine, the Tellus wind turbine at Risø, and an active stall-regulated megawatt wind turbine. The model showed good agreement with measurements and good correspondence between power and thrust.

Yawed flow conditions. With the increase in computational power, it is today both possible and affordable to do yaw computations using CFD. In contrast to the axial flow cases, the total rotor must be modeled in yaw simulations, thereby increasing the number of mesh points typically by a factor of three. Additionally, the azimuth variation inherent in yaw simulations dictates a time accurate simulation, because no steady-state solution can exist, thereby greatly increasing the computing time. The yaw data for 10°, 30°, and 60° yaw error at a wind speed of 15 m/s were used for CFD validation, with good qualitative agreement; see Figure 3-1.
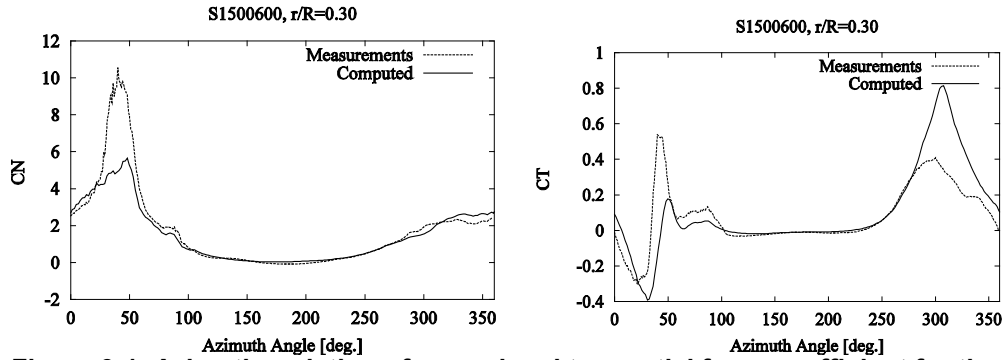
Figure 3-1. Azimuth variation of normal and tangential force coefficient for the NREL Phase VI turbine at the r/R=0.4 section during a 60° yaw error at 15 m/s wind speed

Operation with step pitch. In the design of wind turbines and their control algorithms, the transient loads, especially those generated by time-varying blade loads, are very important. In the blade element momentum method, the most widespread tool in the wind turbine industry, the time constants necessary to describe these problems are not an inherent part of the model. The present study used two different approaches to determine these time constants, the EllipSys3D Navier-Stokes solver and an actuator-disk method. The time constants estimated by the actuator disc method is afterward used in a standard BEM method and a BEM method coupled with a near wake method. The resulting transients were compared to measured values for a step pitch change taken from the unique data set of the NREL/NASA Ames experiment, with good agreement for the case with low loading.

Downwind operation. The EllipSys3D code was recently adapted for computation of rotor-tower interaction on wind turbines. As part of the validation of the code, the downwind data from the Phase VI experiment have been used extensively. The numerical results were in very good agreement with the experiment, capturing the interaction between the rotor blades and the unsteady wake from the tower.

Figure 3-2 shows the flow development downstream of the turbine and a comparison between computations and experimental data of the normal force coefficient at 80% span.
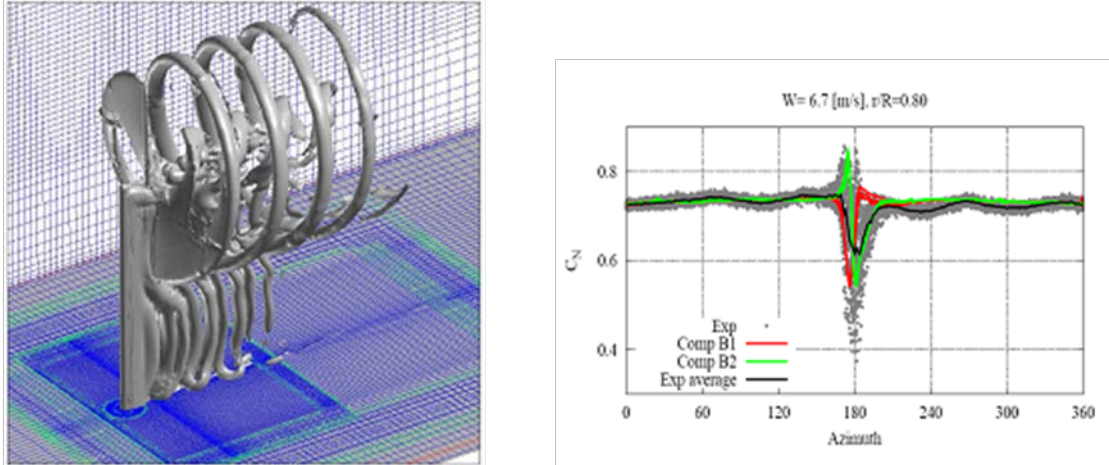
Figure 3-2. (a) Vorticity magnitude isosurface plot showing rotor tip and root vortices and tower wake, (b) normal force coefficient at 80% span showing the effect of the tower wake on the rotor load

3.3 Applied Models and Software

CFD. The in-house CFD solver EllipSys3D was used in the Annex XX work. The code was developed in cooperation with the Department of Mechanical Engineering at DTU and the Department of Wind Energy at Risø National Laboratory; see Michelsen (1992, 1994) and Sorensen (1995). The EllipSys3D code is a multiblock finite volume discretization of the incompressible RANS equations in general curvilinear coordinates, and is second order accurate in both time and space. The code is parallelized with MPI for executions on distributed memory machines using a nonoverlapping domain decomposition technique. This work modeled the turbulence in the boundary layer with the k-ω SST eddy viscosity model (Menter 1993). A moving mesh formulation in a fixed frame of reference modeled the rotation and pitch of the rotor. The moving mesh option has been implemented in the EllipSys3D solver in a generalized way, allowing arbitrary deformation of the computational mesh, following Demirdzic and Peric (1988). It has been used for doing unsteady simulations for several years for both stiff rotors in yaw and fully coupled aeroelastic computations (Bertagnolio et al. 2002, 2003; Sørensen, Michelsen, and Schreck 2002; Madsen, Sørensen, and Schreck 2003).

For the downwind configuration, the EllipSys3D code was altered to take into account the relative movement between the rotor and the tower. Using the overset grid method (also known as overlapping or chimera grid method) makes it possible to simulate the entire turbine, including rotor, tower, nacelle, and ground boundary.

Engineering models. The two aeroelastic codes HAWC and HAWC2 were used and some of the engineering submodels within these codes have been validated. In particular, this work considered the dynamic induction modeling in HAWC 2 as well as the yaw modeling.

A near wake model for dynamic induction modeling was also applied on the cases of pitch step measurements (Madsen and Rasmussen 2004).

3.4 Research Results

Since the release of the Annex XX database, much of the validation work at Risoe-DTU in connection with CFD focused on these data, using them to validate the new overset version of the EllipSys3D solver. In addition, the NREL data have demonstrated how CFD computations can produce results for rotor aerodynamics, for simple axial flow, yawed cases, and for rotors performing step pitch motions. A second issue highlighted by studying the NREL data is that CFD is a valuable tool to obtain qualitative knowledge about flow physics to interpret experimental data.

For engineering submodels, researchers verified the time constants in the dynamic induction modeling as well as the correction terms in the modeling of yawed flow.

The aerodynamic characteristics for the airfoil sections used in aeroelastic calculations are important to predict correct loads. 3D effects such centrifugal and Coriolis forces, however, change the characteristics compared to 2D wind tunnel tests. Pressure distributions measured in the NREL/NASA Ames test allowed researchers to formulate a new model to correct for these 3D effects. This model can be used to correct 2D wind tunnel data before carrying out aeroelastic calculations.

3.5 Conclusions and Future Work

The Annex XX database has been valuable for developing and validating several different models within CFD and engineering modeling. It is expected that the database will be used in for similar purposes in the future.

3.6 Bibliography

Bak, C.; Johansen, J. (2005). "3D Correction of Airfoil Data Based on Pressure." Prepared for the IEA Joint Action Committee on Aerodynamics, Annex XI and XX Aero Experts Meeting, Pamplona, Spain, May 25–26.

Bak, C.. (2005). "Metode til 3D korrektion af profildata." Forskning i Aeroelasticitet – EFP-2004, Risø-R-1509(DA), May 2005, pp. 11–25.

Bak, C.; Johansen J.; Andersen, P.B. (2006). "Three-Dimensional Corrections of Airfoil Characteristics Based on Pressure Distributions." Presented at EWEC-2006, Athens, Greece, February 27–March 2.

Bertagnolio, F.; Gaunaa, M.; Hansen, M.; Sørensen, N.N.; Rasmussen, F. (2002). "Computation of Aerodynamic Damping for Wind Turbine Applications." Prepared for the 4th GRACM Congress on Computational Mechanics, Patras, Greece, June 27–29.

Bertagnolio, F.; Gaunaa, M.; Sørensen, N.N.; Hansen, M.; Rasmussen, F. (2003). "Computation of Modal Aerodynamic Damping Using CFD." Prepared for the 22nd ASME Wind Energy Symposium, Reno, Nevada, January 6–9.

Demirdzic, I.; Peric, M. (1988). "Space Conservation Law in Finite Volume Calculations of Fluid Flow." *Int. J. Numer. Methods Fluids* (8); pp. 1037–1050.

Hansen, M.O.L.; Johansen, J. (October/December 2004). "Tip Studies Using CFD and Comparison with Tip Loss Models." *Wind Energy* (7:4); pp. 343–356.

Hansen M.O.L. and Johansen J., (2004). "Tip Studies Using CFD and Comparison with Tip Loss Models." Prepared for the Special Topic Conference, The Science of Making Torque from Wind, Delft, Netherlands, April 19–21.

Johansen J.; Sørensen, N.N. (2003a). "Method for Extracting Airfoil Data using 3D CFD Computations." Prepared for the IEA Joint Action Committee on Aerodynamics Annex XI Aero Experts Meeting, Boulder, Colorado, May 5–6.

Johansen J. and Sørensen N.N. (2003b). "Risø's CFD contribution to Annex XX." Prepared for the IEA Annex XX, Aerodynamics and Models from Wind Tunnel Measurements Meeting, Boulder, Colorado, May 7–8.

Johansen J., Sørensen N.N. (October/December 2004). "Aerofoil Characteristics from 3D CFD Rotor Computations." *Wind Energy* (7:4); pp. 283–294.

Johansen, J.; Sørensen, N.N. (2004). "Airfoil Characteristics from 3-D CFD Rotor Computations." Pages 9–15 in *Proceedings, Special Topic Conference: The Science of Making Torque from Wind, Delft (NL), 19-21 April 2004.* Delft, Netherlands: Delft University of Technology.

J. Johansen and N.N. Sørensen. (2006). "Aerodynamic Investigation of Winglets on Wind Turbine Blades Using CFD." Prepared for the IEA Annex XI/XX Joint meeting, Kiel, Germany, April 25–26.

Johansen, J.; Sørensen, N.N.; Michelsen, J.A. (2002). "Navier-Stokes Simulation of Three Tip Shapes for Wind Turbine Blades." Prepared for the 4th GRACM Congress on Computational Mechanics, Patras, Greece, June 27–29.

Johansen, J., Sørensen, N.N., Michelsen, J.A., Schreck, S. (2001). "Detached-Eddy Simulation of Flow around the S809 Airfoil." Pages 414–417 in *Wind Energy for the New Millennium. Proceedings, 2001 European Wind Energy Conference and Exhibition (EWEC '01), Copenhagen (DK), 2–6 July 2001.* Helm, P.; Zervos, A., eds. Munich: WIP Renewable Energies.

Johansen, J., Sørensen N.N., Michelsen, J.A. and Schreck, S. (2002). "Detached-Eddy Simulation of Flow around the NREL Phase-VI Blade." *Wind Energy* (5); 185–197.

Johansen, J.; Sørensen, N.N.; Michelsen, J.A.; Schreck, S. (2003). "Detached-Eddy Simulation of Flow around the NREL Phase-VI Rotor." In *Proceedings, European Wind Energy Conference and Exhibition 2003 (EWEC 2003), Madrid, June 16–19.* Brussels: European Wind Energy Association.

Madsen, H.A. (2003). "Risoe Activities in IEA Annex XX." Prepared for the IEA Annex XX, Aerodynamics and Models from Wind Tunnel Measurements Meeting, Boulder, Colorado, May 7–8.

Madsen, H.A.; Rasmussen, F. (2004). "A Near Wake Model for Trailing Vorticity Compared with the Blade Element Momentum Theory." *Wind Energy* (7); pp. 325–341.

Madsen, H.A.; Sørensen, N.N.; Schreck, S. (2003). Yaw Aerodynamics Analyzed with Three Codes in Comparison with Experiment. In: AIAA Paper 2003-519. 41. Aerospace sciences meeting and exhibit, Reno (US), 6–9 Jan 2003. (American Institute of Aeronautics and Astronautics, Inc., Reston, VA, 2003)

Menter, F.R. (1993). "Zonal Two Equation k-ω Turbulence Models for Aerodynamic Flows." AIAA paper 93-2906.

Michelsen, J.A. (1992). "Basis3D: A Platform for Development of Multiblock PDE Solvers." Technical Report AFM 92-05. Lyngby: Technical University of Denmark.

Michelsen J.A. (1994). "Block Structured Multigrid Solution of 2D and 3D Elliptic PDE's." Technical Report AFM 94-06. Lyngby: Technical University of Denmark.

Schreck, S.J.; Sørensen, N.N.; Robinson, M.C. (2006). "Aerodynamic Structures and Processes in Rotationally Augmented Flow Fields." *Wind Energy* (10); pp. 159–178.

Schreck S.J.; Sørensen, N.N.; Robinson M.C. (2003). "Aerodynamic Structures and Processes in Rotationally Augmented Flow Fields." In *Proceedings, European Wind Energy Conference and Exhibition 2003 (EWEC 2003), Madrid, June 16–19*. Brussels: European Wind Energy Association.
Sørensen, N.N. (1995). "General Purpose Flow Solver Applied to Flow over Hills." Risø-R-827-(EN). Roskilde, Denmark: Risø National Laboratory.

Sørensen, N.N.; Madsen, H.A. (2006). "Modelling of Transient Wind Turbine Loads during Pitch Motion (paper and poster). In *Proceedings, 2006 European Wind Energy Conference and Exhibition, Athens, Greece, February 27–March 2*. Brussels: European Wind Energy Association.

Sørensen, N.N.; Michelsen, J.A. (November 2004). "Drag Prediction for Blades at High Angle of Attack Using CFD." *Journal of Solar Energy Engineering*, v. 126, n. 4, pp. 1011-1016**.**

Sørensen, N.N.; Michelsen, J.A.. (2004). "Drag Prediction for Blades at High Angle of Attack Using CFD." 2004 ASME Wind Energy Symposium Technical Papers Presented at the 42nd AIAA Aerospace Sciences Meeting and Exhibit, pp. 386–393

Sørensen, N.N.; Johansen, J.; Conway, S. (2004). "CFD Computations of Wind Turbine Blade Loads during Standstill Operation KNOW-BLADE." Task 3.1 report. Risø-R-1465(EN). Roskilde, Denmark: Risø National Laboratory.

Sørensen, N.N.; Michelsen, J.A.; Schreck, S. (2001). "Detailed Aerodynamic Prediction of the NREL/NASA Ames Wind Tunnel Tests using CFD." In: Wind energy for the new millennium. Proceedings. 2001 European wind energy conference and exhibition (EWEC '01), Copenhagen (DK), 2–6 Jul 2001. Helm, P.; Zervos, A. (eds.), (WIP Renewable Energies, München, 2001) p. 48–53.

Sørensen, N.N.; Michelsen, J.A.; Schreck, S.. (2002a). "Navier-Stokes Predictions of the NREL Phase VI Rotor in the NASA Ames 80 ft × 120 ft Wind Tunnel." *Wind Energy* (5); pp. 151–169.

Sørensen, N.N.; Michelsen, J.A.; Schreck, S.. (2002b). "Application of CFD to Wind Turbine Aerodynamics." Presented at the 4th GRACM Congress on Computational Mechanics, GRACM 2002, Patras, Greece, June 27–29.

Sørensen, N.N.; Johansen, J.; Conway, S.; Voutsinas, S.; Hansen, M.O.L.; Stuermer, A. (2005). "KNOW-BLADE Task-3.2 report; Tip Shape Study." Risø-R-1495(EN). Roskilde, Denmark: Risø National Laboratory.

Zahle, F. (2006). *Wind Turbine Aerodynamics Using an Incompressible Overset Grid Method*. Ph.D. Thesis. London: Imperial College.

Zahle, F.; Sørensen, N.N. (2007a). "Investigation of the Influence of Wake Resolution on Wind Turbine Rotor Flow Simulations." Presented at the IEA Annex XI/XX Joint Meeting, Risø National Laboratory, Roskilde, Denmark, June 14–15.

Zahle, F.; Sørensen, N.N. (2007b). "On the Influence of Far-Wake Resolution on Wind Turbine Flow Simulations. International conference: The science of making torque from wind, Lyngby (DK), 28-31 Aug 2007. J. Phys.: Conf. Ser. (2007) 75, 9 p.

Zahle, F.; Johansen, J.; Sørensen, N.N. (2007). "Wind Turbine Aerodynamics Using an Incompressible Overset Grid Method." Pages 9–19 in *Scientific Proceedings, 2007 European Wind Energy Conference and Exhibition, Milan (IT), May 7–10.* Brussels: European Wind Energy Association.

Zahle, F.; Sørensen, N.N.; Johansen, J.; Graham, J.M.R. (2006). "Rotor Tower Interaction Using an Incompressible Overset Grid Method. Presented at the IEA Annex XI/XX Joint Meeting, Kiel, Germany, April 25–26.

4.0 Research Summary—Greece

Organization: Centre for Renewable Energy Sources (CRES)

Researcher: Evangelos Politis, vpolitis@cres.gr

Budgetary constraints restricted the participation of the Centre for Renewable Energy Sources (CRES) in Annex XX to less than originally planned. Nevertheless, CRES co-financed the activities of Annex XX and benefited from the knowledge gained through the results produced by the other participants. Because the results of the work of the other participants were disseminated to CRES, the Centre was able to access the state-of-the-art developments in the aerodynamics of wind turbine research for potential use in the years to come.

5.0 Research Summary—Netherlands (ECN)

Organization: Energy Research Centre of the Netherlands (ECN)

Researchers: [*]Gerard Schepers, schepers@ecn.nl
Koert Lindenburg, lindenburgl@ecn.nl
Herman Snel, snel@ecn.nl

5.1 Background and Motivation

This report summarizes the most important results of ECN's contribution to IEA Wind Annex XX. Annex XX is an international cooperation between several parties from eight countries, coordinated by the U.S. National Renewable Energy Laboratory (NREL). The Dutch contribution to Annex XX was sponsored by SenterNOVEM.
The work of this project extended from 2003 to 2007.

The main aim of Annex XX was to analyze the measurements that were taken by NREL on a wind turbine placed in the large (24.4 m × 36.6 m) National Aeronautics and Space Administration (NASA)-Ames wind tunnel. This wind turbine was two-bladed with a rotor diameter of 10 m. One blade was instrumented with pressure taps at five radial positions to measure local pressure distribution and resulting sectional aerodynamic loads. Many measurements at very different conditions were stored in a database, which was made accessible to the Annex XX participants.

The present set of measurements offers a unique base for investigating aerodynamic effects and for validating and improving wind turbine design codes. An important advantage is that aerodynamic forces are measured at different radial positions, by which local aerodynamic effects can be assessed. Usually wind turbine measurements give only integrated blade and rotor loads, which hide the details on sectional level.

Local aerodynamic loads were also measured in Annex XVIII (Schepers et al. 2002), but they were taken on turbines in the free atmosphere, where the uncertainty resulting from the nonstationary, inhomogeneous, and uncontrolled wind conditions formed an important problem (as in all field measurements). Hence a very important additional advantage of the present measurements lies in the wind tunnel environment, which yields (almost) stationary and homogeneous conditions. The huge size of the wind tunnel allows a rotor diameter of 10 m, with very few blockage effects. Obviously this rotor diameter is still (much) smaller than the diameter of today's commercial wind turbines; nevertheless the blade Reynolds number (approximately 1 million) is sufficiently high to make the aerodynamic phenomena at least to some extent representative for modern wind turbines.

In the ECN contribution to Annex XX, particular emphasis has been put on the validation of an aero-elastic code PHATAS (Lindenburg, 2005) and a free wake lifting line model AWSM

(van Garrel, 2003). Special attention was paid to 1) non-yawed conditions, 2) yawed conditions and 3) dynamic inflow at fast pitching steps. The background/motivation to select data at these particular conditions, can be described as follows.

The comparison at nonyawed flow and at relatively low tunnel speeds offers insight into the basic accuracy of design codes at normal conditions. The results at high tunnel speeds offer useful insights on three-dimensional stall effects.

The ECN study on yawed conditions offered insight into the load variations, which result from two effects:

- The variation in induced velocity caused by the skewed (asymmetric) wake geometry

- The advancing and retreating blade effect in combination with dynamic stall effects.

Both effects determine the cyclic load fluctuation (which is relevant for fatigue load calculations). The first effect also contributes to the yawing stability. The variation of the induced velocity obviously mainly plays a role at high axial induction factors (i.e., relatively low wind speeds) where the advancing and retreating blade effect is important at high tunnel speeds because the high lateral component of the skewed wind speed, which, in combination with the high angle of attack, leads to strong dynamic stall effects.

The results at fast pitching transients offer insight into the dynamic inflow phenomenon. Dynamic inflow is characterized by a load overshoot followed by a gradual approach to the new equilibrium value. These effects have a large practical importance, not only in view of the higher dynamic loads on a turbine but also because of its impact on the aerodynamic damping characteristics and in particular in the design of pitch control algorithms; see van Engelen and van 't Hooft (2004).

Furthermore a model has been developed that covers instationary effects at attached flow. These effects are important for the correct prediction of the stability of edgewise vibrations at pitching actions. This report gives a summary of only the most important results obtained by ECN. More detailed information can be found in ECN task reports; see e.g., Schepers (2007a, 2007b, 2007c).

5.2 Data Used

NREL performed measurements for a wide variety of conditions (tunnel speeds, pitch angles, and yaw angles) and different configurations (upwind, downwind, teetered, and nonteetered). The data are stored in a (password protected) database. As mentioned in Section 5.1, ECN's investigations focused on the aerodynamic effects at nonyawed flow, yawed flow, and fast pitching steps.

5.2.1 Selected Data at Nonyawed Flow
As a first step in the project, the measurements at nonyawed conditions from the NREL UAE Phase VI H, I, and J sequences. In these sequences the rotor is rigid (i.e., nonteetered) and located upwind from the tower. The difference between the sequences lies in the pitch angle:

The pitch angle for the H sequence is nominal, i.e., 3°. The pitch angle for the I sequence is 0° and the pitch angle for the J sequence is 6°.

For every sequence, time series have been selected at tunnel speeds that vary between the lowest possible speed of 5 m/s and the highest possible speed of 25 m/s, with an interval of 1 m/s. In all sequences the rotor speed is 72 rpm, which in combination with these tunnel speeds leads to a relatively low tip speed ratio.

In the analysis of the results, it is important to have a global idea on the local aerodynamic conditions at the different campaigns. The PHATAS calculation code was thus used to calculate the axial induction factor and the angle of attack at three radial positions (30% or 47% span, 63% span, and 80% span). The results are shown graphically as function of tunnel speed and the three pitch angles in Figures 5-1 and 5-2. As expected, the angle of attack increases with tunnel speed and decreases with pitch angle and radial position. Because of the low tip speed ratio, most angles of attack have already exceeded the two-dimensional (2D) stalling angle of attack of ~ 10° at a tunnel speed of 10 m/s. Furthermore, substantial induction factors are only found at a tunnel speed of 5 m/s and a pitch angle of 0°. At a tunnel speed of 10 m/s, the axial induction factors are between 0.1 and 0.15, and at 15 m/s, the induction factors are less than 0.1.
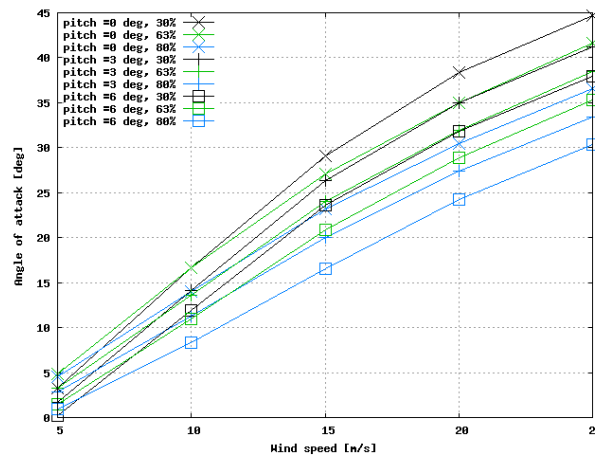
Figure 5-1. Angle of attack calculated by PHATAS for different pitch angles, radial positions, and wind speeds
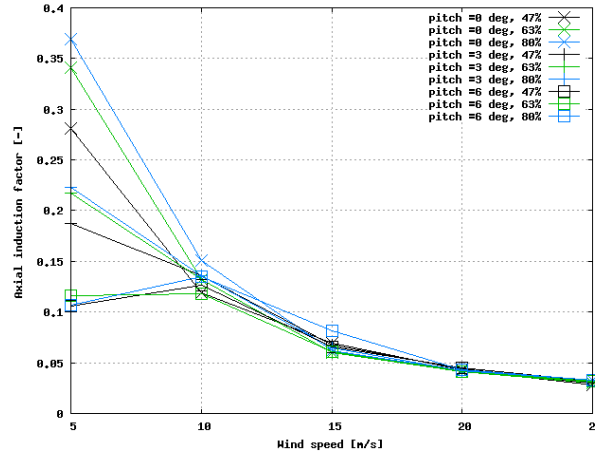
Figure 5-2. Axial induction factors calculated by PHATAS for different pitch angles, radial positions, and wind speeds

5.2.2 Selected Data at Yawed Flow

The study on yawed flow took measurements from the H, I, and J sequences; see Section 5.2.1. Two yaw angles were considered: 10° and 30°. The main emphasis here is on the results at 30°. Qualitatively speaking, the results for both yaw angles turned out to be very similar (the only difference appears to be in the magnitude of the load variations, which is obviously smaller for a yaw angle of 10°). Measurements at very large yaw angles (greater than 30°) were taken, but these are not investigated here.

As mentioned in Section 5.1, the aim of ECN's study on yawed flow was to investigate the load variations that result from two effects: the variation in induced velocity caused by the skewed (asymmetric) wake geometry, and the advancing and retreating blade effect in combination with dynamic stall effects. The first effect plays a role mainly at low tunnel speeds (i.e., high axial induction factors), and the second effect is particularly important at high tunnel speeds.

The minimum tunnel speed for the yawed campaigns was similar to the one for the nonyawed cases (5 m/s), where the maximum tunnel speed was slightly lower (16 or 17 m/s). As explained in Section 5.2.1, the low rotational speed of the present configuration makes the tip speed ratio relatively low, which in turn leads to a low induction factor and a high angle of attack.

With these considerations in mind, measurements have been selected at V_{tun} = 5, 10, and 15 m/s for all sequences. The measurements at V_{tun} = 5 m/s are expected to be useful for the investigation of the skewed wake effect on the inflow because the averaged angle of attack is below 5° and the axial induction factor is approximately 0.2 for Sequence H and 0.3 for Sequence I (see Section 5.2.1). These axial induction factors are sufficiently high to expect at least some effect from the variation in induced velocity at yawed conditions, where the low angle of attack limits the "disturbance" from dynamic stall effects.

The measurements at higher tunnel speeds are expected to provide information on the advancing and retreating blade effect in combination with dynamic stall effects because of the high angles of attack and the low induction.

28

The definitions of yaw angle and azimuth angle used in this study differ from the NREL definitions. The actual rotor placed in the NASA-Ames tunnel rotated counterclockwise and applied the 0 azimuth angle at the 12 o'clock position. The measurement data have been transformed to a clockwise rotating turbine with 0° azimuth at the 6 o'clock position and a yaw angle with sign opposite to the NREL yaw angle.

5.2.3 Selected Dynamic Inflow Measurements

For dynamic inflow analyses, NREL measured time series at fast stepwise pitch changes, similar to the ones measured by the Technical University of Denmark in the European Dynamic Inflow projects; see Snel and Schepers (2004).

NREL performed the pitching steps at different tunnel speeds, but dynamic inflow effects become more prominent at high induction factors. As explained earlier, a high induction factor is associated with a low tunnel speed, and for this reason, the time series at the lowest tunnel speed of 5 m/s (with NREL identification Q0500000) was obtained from NREL.

Figure 5-3 shows the measured time series of the pitch angle at his tunnel speed. The measurement period is 600 s, and within this period 20 pitch angle steps are performed. The pitch angle was repeatedly increased with a fast pitching speed from a pitching angle of approximately -5.9° to 10.02°, after which it remains constant for some 15 s. Thereafter it decreases again to a pitch angle of -5.9°.
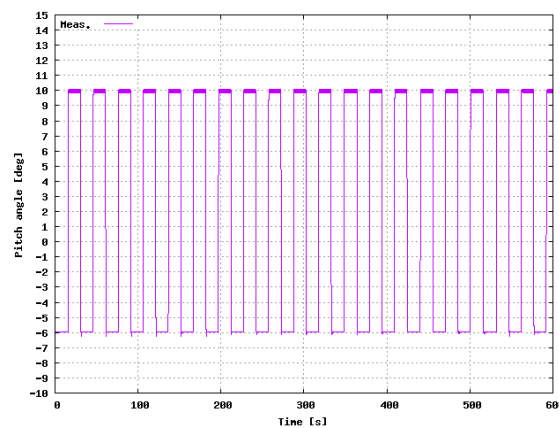
Figure 5-3. Pitch angle variation during dynamic inflow transient

The axial induction factors (at the instrumented section 30% to 95% span) have been calculated with ECN's aero elastic code PHATAS. The results are shown in Table 5-1 for the five instrumented sections.

Table 5-1. Axial induction factor at fast pitching step

Pitch angle(°)	a_{30}	a_{47}	a_{63}	a_{80}	a_{95}
-5.9	0.32	0.42	0.58	0.68	1.06
10.02	0.039	0.005	0.008	-0.017	-0.03

The rotor is heavily loaded at a pitch angle of –5.9°, but very lightly loaded at a pitch angle of 10.02°. As such, the pitch angle steps should be considered artificial, but they are suitable for validation.

To smooth the load signals, ECN applied an averaging procedure, similar to the one used by the Technical University of Denmark in the Dynamic Inflow project (see Snel and Schepers, 1994). The different pitching steps are synchronized by initializing them to the start of the pitching step transient. The synchronized time series are then averaged to filter out as many of the fluctuations as possible. Figure 5-4 shows the resulting time series of the pitch angles of both blades for the upward and downward step.
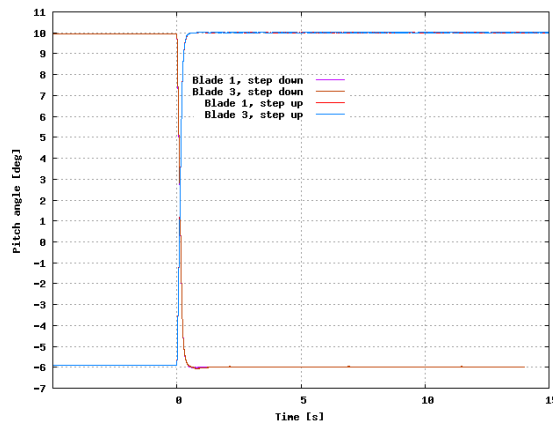
Figure 5-4. Pitch angles of both blades, averaged over all transients, for upward and downward pitching step

5.3 Methods Employed

ECN's main activities consisted comparing the NASA-Ames measurements with calculated results from two of ECN's codes:

- The aeroelastic wind turbine design code PHATAS. This code has been used to calculate all the measurement cases.

- The free wake lifting line code AWSM. This code has been used to calculate the cases only at low tunnel speeds because for high tunnel speeds (say tunnel speeds > 10 m/s) the angle of attack exceeds the stall angle of attack, where, in principle, AWSM does not account for stall effects. Furthermore, the potential advantage of AWSM lies in its calculation of induction. As such, comparing AWSM and the measurements makes most sense for conditions where the induction is relatively large, i.e., for low tunnel speeds; see Figure 5-2.

5.3.1 PHATAS
The calculations described here were performed with PHATAS release "Apr-2005". Lindenburg (2005) described this version of the code. The following remarks can be made about the PHATAS simulations:

- The input on the NREL wind turbine is based on the description given in Lindenburg (2003). Several degrees of freedom are taken into account, e.g., blade flexibility in the

edgewise and flatwise direction, blade torsion, shaft torsion, and dynamics of the tower. Furthermore, the asynchronous generator has been modeled.

- The tunnel speed is assumed to be homogeneous and constant in time. Tower shadow has been included.

- The pitch angle is assumed to be constant (except for the dynamic inflow transients, where the measured time series of the pitch angle is prescribed).

- The calculations were performed over a period of 20 s (except for the dynamic inflow transient where the measured time series is simulated).

- The aerodynamic modeling of PHATAS is based on the blade element momentum theory. This requires tables of aerodynamic characteristics [i.e., $c_l(\alpha)$, $c_d(\alpha)$, and $c_m(\alpha)$]. The airfoil section along the blade is the NREL S809 profile.

- The 2D, stationary (nonrotating) aerodynamic characteristics of this airfoil were constructed by combining wind tunnel measurements from the University of Delft with wind tunnel data from Ohio State University. The data were extended to deep stall according to the method described in chapter 2 of Lindenburg (2003). Figures 5-5 and 5-6 present the resulting 2D aerodynamic characteristics.

- In subsequent work, much attention will be paid to the modeling of three-dimensional effects in stall. These effects are accounted for by the model from Snel et al. (1993), where a factor f_{cl} is used to correct the available 2D lift coefficients $c_{l,2D}$. The factor f_{cl} is the ratio of the actual increase in c_l (i.e., $c_{l,3D} - c_{l,2D}$) and the difference d_{c_l} between the nonviscous lift coefficient $c_{l,potential}$ (with "potential" slope $dc_l/d\alpha = 2\pi\,\alpha$) and the 2D value of $c_{l,2D}$. Hence:

$$c_{l,3D} = c_{l,2D} + f_{cl}\,(c_{l,potential} - c_{l,2D}); \text{ the factor } f_{cl} \text{ is given by } f_{cl} = 3\,(c/r)^2.$$

- Note that the method corrects only the lift coefficients and not the drag and the moment coefficients.

- Dynamic stall is modeled with the first order dynamic stall model from Snel (1997). Again only the lift is corrected.
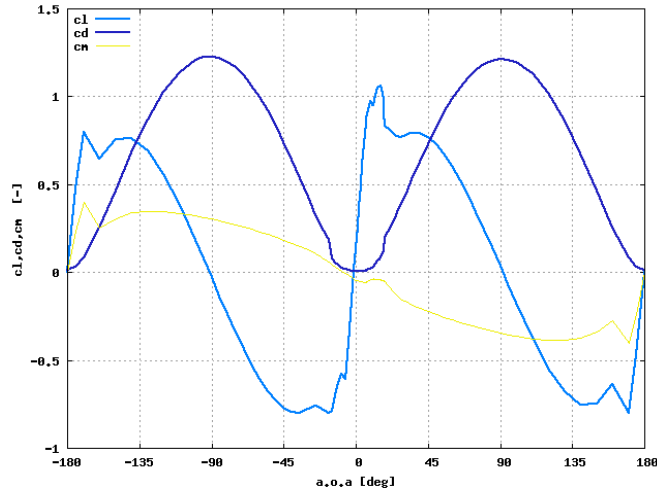
Figure 5-5. S809 airfoil: Basic 2D aerodynamic coefficients for –180 < α < 180
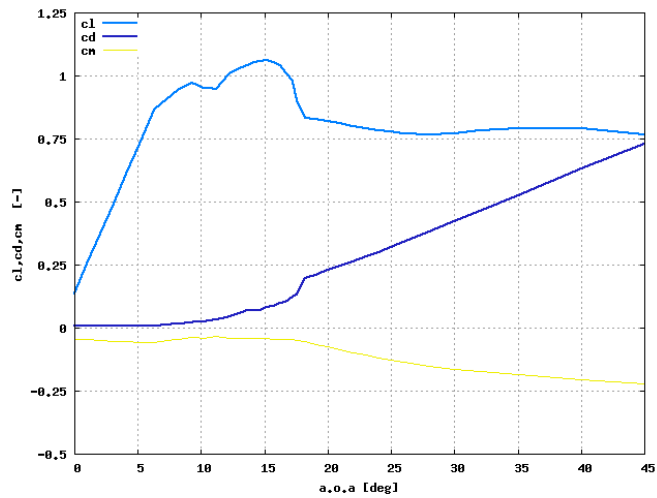
Figure 5-6. S809 airfoil: Basic 2D aerodynamic coefficients for 0 < α < 45

5.3.2 AWSM

The AWSM code (van Garrel 2003) is based on a nonlinear lifting line vortex wake theory. The code is of a free wake character, but for distances greater than four rotor diameters downstream of the rotor, the wake is assumed to be "frozen."

The blades are modeled as lifting lines. This implies that, similar to the PHATAS code, aerodynamic profile data should be prescribed as a function of the angle of attack. The same airfoil data as used in PHATAS have thus been applied. 3D and dynamic stall corrections are not taken into account (although instationary effects that result from the shed vorticity are modeled).

In principle, a 3D stall correction could be added to the airfoil characteristics, but AWSM has been used to simulate only low tunnel speed cases, for which stall corrections are less relevant.

The AWSM calculations were made under the following assumptions:

- The construction is assumed to be rigid and mass-induced loads are neglected.

- The wind speed is constant in time and homogenous; the aerodynamic tower shadow effect has been neglected.

- The rotor speed and pitch angle are constant (except for the dynamic inflow transient where the measured pitch angle is prescribed).

- The calculations have been performed for a period of 11 s (except for the dynamic inflow transient where the measured time series is simulated).

5.3.3 Comparison between Calculated and Measured Results

The comparisons between calculations and measurement at nonyawed conditions are mostly made in terms of mean blade segment loads (normal and tangential forces), flatwise moments at the blade root, and the rotorshaft torque; i.e., the values are averaged over the calculation or measurement time. Such comparison is based on dimensional quantities that are calculated at given external conditions [although the comparison on normal and tangential forces is of c_n (c_t) $0.5\rho V^2$, which differ from the actual forces through the (constant) value of the chord]. Such comparison avoids the uncertainty in the measured angle of attack and dynamic pressure experienced when the comparison is of dimensionless aerodynamic characteristics such as function of the angle of attack; see, e.g., Schepers et al. (2002).

The comparison at yawed conditions is mostly made in terms of azimuthally binned averaged values. The comparison of the dynamic inflow cases is made on basis of time series, where the averaged measured pitch angle step has been prescribed to PHATAS and or AWSM.

5.4 Research Results

5.4.1 Nonyawed Conditions

The results at nonyawed (stationary) conditions led to the conclusions described in this section. Most investigated loads are predicted well with ECN's aeroelastic code PHATAS as long as the tunnel speed is relatively low (e.g., less than 10–12 m/s, which corresponds to an angle of attack below the stall angle of attack). The most pronounced exception is the overprediction of the normal force at 95% span. Figures 5-7 and 5-8 show the ratio between calculated and measured normal forces at 30% and 95% span as a function of tunnel speed for the three different pitch angles (a ratio of 1 corresponds to an optimal agreement).
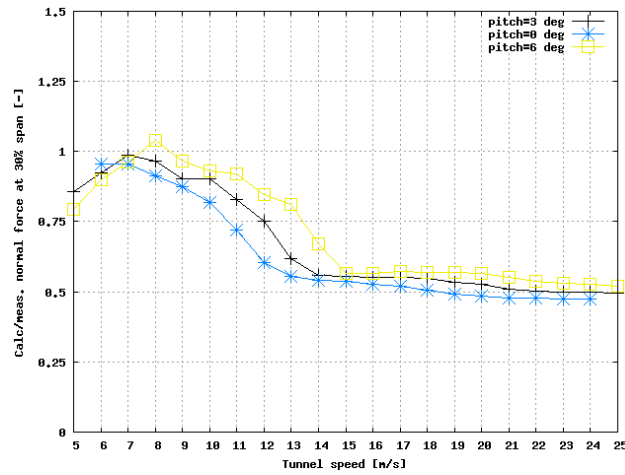
Figure 5-7. Nonyawed conditions: Ratio between calculated and measured normal force at 30% span for three different pitch angles
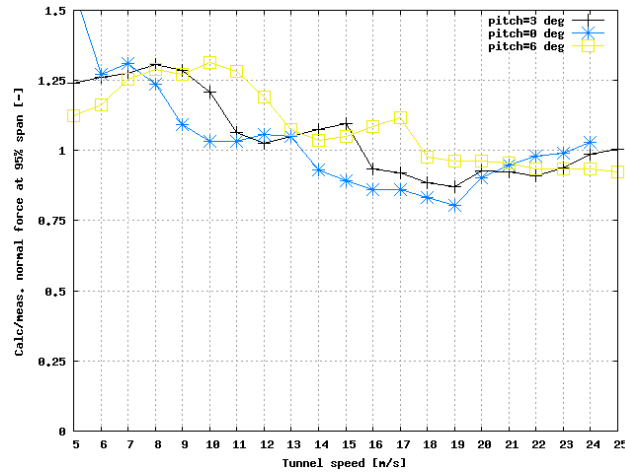
Figure 5-8. Nonyawed conditions: Ratio between calculated and measured normal force at 95% span for three different pitch angles

At higher tunnel speeds, the PHATAS code underpredicts the normal forces and overpredicts the tangential forces. The latter observation implies the prediction of too strong a force toward the leading edge. These deficiencies are most likely caused by 3D effects in stall. It implies that the 3D correction from Snel et al. (1993), as implemented in PHATAS, yields a too low increase in lift coefficient, where at the same time the drag should be increased. The Annexlyse project (Schepers 2004), which analyzed field measurements on different turbines, made similar observations. The empirical corrections derived from those measurements, however, lead for the present configuration to an "overcorrected" lift increase and drag increase.

The overpredicted tangential force is reflected by an overprediction of the rotor shaft torque at the high tunnel speeds. The underpredicted normal force is reflected by an underpredicted flatwise moment;

34

The calculations from the free wake lifting line code AWSM (which are performed only for low tunnel speeds) show good agreement with the measured loads. Even at the 95% span the agreement is reasonable and better than the agreement from the corresponding PHATAS calculation. Figure 5-9 shows the measured normal force for a tunnel speed of 5 m/s ($\theta = 3°$) as function of radial position compared to the normal forces predicted by PHATAS and AWSM.
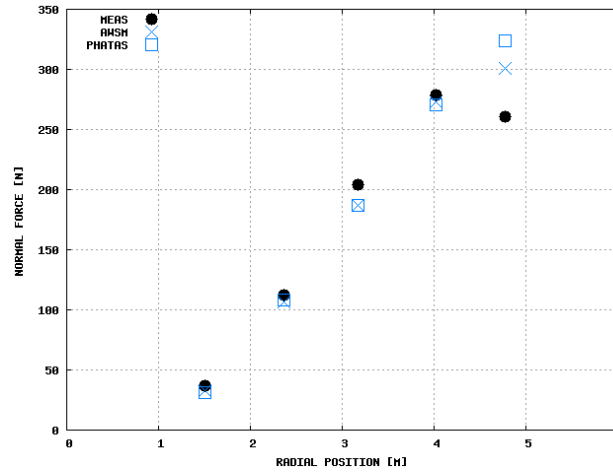
Figure 5-9. Comparison of measured normal force and normal forces calculated by AWSM and PHATAS

5.4.2 Yawed Conditions

At yawed flow, the investigation put particular emphasis on the azimuthal variation of the normal forces by (1) the advancing and retreating blade effect and (2) the variation in induced velocity from the skewed wake geometry, where the second effect is expected to be dominant at a low tunnel speed of 5 m/s and the first effect is expected to be dominant at higher tunnel speeds.

Figure 5-10 shows the measured normal force variation at the five instrumented sections, for the case with the highest induction ($\theta = 0°$) at a tunnel speed of 5 m/s. At this wind speed, the variation of the normal forces is clearly influenced by the skewed wake effect, which leads to a strong radial dependency on the azimuthal variation of the normal forces. At the outboard part of the blade, the normal force varies more or less sinusoidally such that the maximum force occurs at the upwind part of the rotor plane (which is between an azimuth angle of 0° and 180°). Such load variation leads to a stabilizing yawing moment. The variation is in line with the outcome of a conventional wake model for calculating induced velocities, which assumes that these velocities are induced by tip vortices only; see Schepers and Snel (1995).
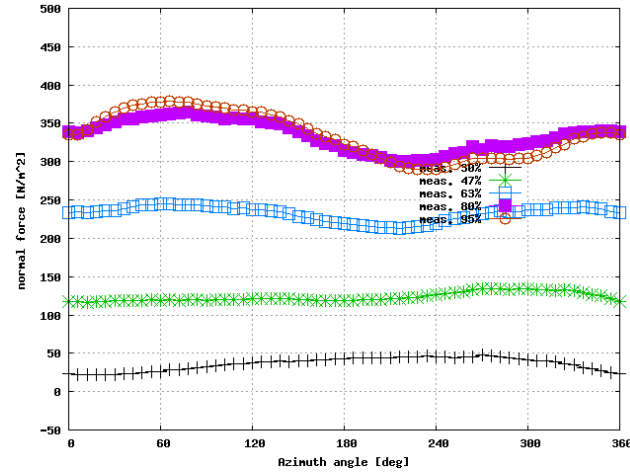
Figure 5-10. Azimuthally binned averaged normal force at V$_{tun}$ = 5 m/s (θ = 0°) and a yaw angle = 30°: Measured data at five radial positions

At the inboard sections of the blade, however, the maximum value of the normal force shifts toward the downwind side of the rotor plane. This is consistent with previous wind tunnel measurements of the inflow velocity, which showed the inflow velocity at the inboard station to reach a maximum at the downwind side of the rotor plane; see Schepers (1999). The shift can be explained by the velocities induced by the root vortex, where conventional yaw models consider only the tip vorticity. The resulting load variation leads to a destabilizing yawing moment.

The AWSM code predicts the above-mentioned radial dependency in azimuthal variation of the normal force very well. Figures 5-11 and 5-12 illustrate this, showing the normal forces at 47% and 95% span. The agreement between the AWSM results and the measurements is excellent in the shape of the normal force distribution (the shape determines the yawing moment and the offset in level at 95% span is consistent with the overpredicted normal force as discussed in Section 5.4.1). The agreement from the PHATAS code is slightly poorer but opposite to common (engineering) yaw models; it predicts a destabilizing yawing moment near the inboard part of the blade in agreement with the measured results.

36
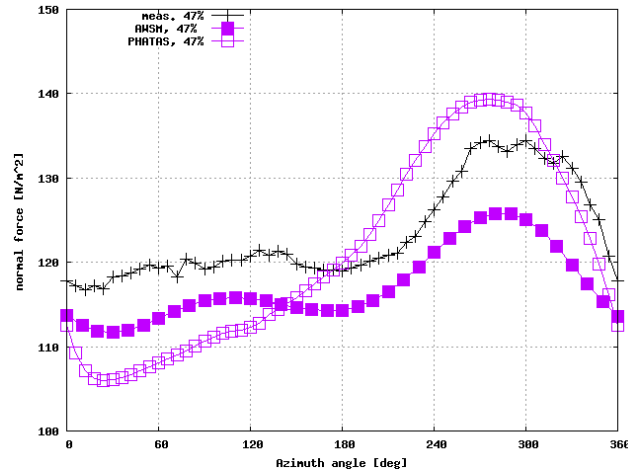
Figure 5-11. Azimuthally binned averaged normal force at 47% span at V$_{tun}$ = 5 m/s (θ = 0°) and yaw angle = 30°: Measured result compared with calculated results
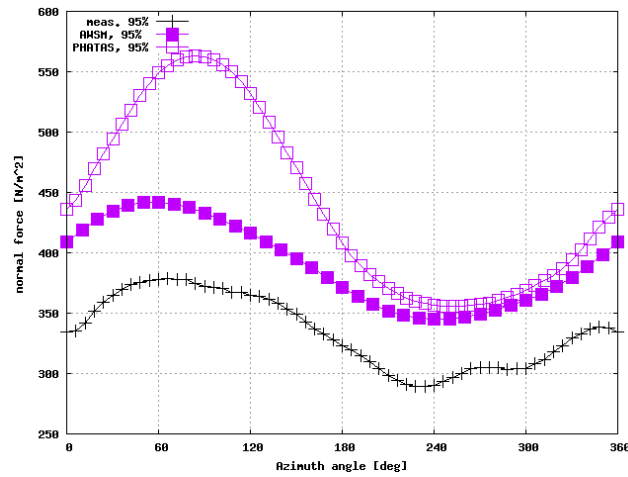
Figure 5-12. Azimuthally binned averaged normal force at 95% span at V$_{tun}$ = 5 m/s (θ = 0°) and yaw angle = 30°: Measured result compared with calculated results

To quantitatively assess the prediction of the skewed wake effect, researchers compared the calculated and measured "sectional yawing moments" were compared. The n(ϕ_r) curves are thus transformed into their contribution to the yawing moment: $M_{yaw} = -n_1(\phi_{r,1})\sin(\phi_{r,1}) - n_3(\phi_{r,3})\sin(\phi_{r,3})$. In this equation, index 1 denotes blade 1 and index 3 denotes blade 3. The blade numbering here is kept similar to the NREL blade numbering, in which blade 3 is the instrumented blade. Hence $\phi_{r,1} = \phi_{r,3} + 180$. Obviously the $n_1(\phi_{r,1})$ curve has not been measured, but it is assumed to be similar to the measured $n_3(\phi_{r,3})$. The equation indicates whether or not the normal force distribution yields a stabilizing yawing moment contribution: a negative value indicates a stabilizing yawing moment and a positive value indicates a destabilizing yawing moment. Table 5-2 lists the (rotor averaged) yawing moment contributions (for the scenario with θ = 0°). The results are consistent with the qualitative observations:

37

- The measured yawing moment contribution stabilizes at the outboard sections (63% to 95% span), and is destabilizing at the inboard sections. PHATAS and AWSM also predict this.

- The AWSM calculated yawing moment and the measured values have good agreement. The AWSM calculated yawing moment is generally closer to the measured values than the PHATAS calculated yawing moment.

In addition, the induced velocities—as calculated by the PHATAS and AWSM codes—generally show a good mutual agreement, even though the underlying models have very different bases.

The calculated results at yawed flow and higher tunnel speeds show much poorer agreement with the measurements (Figure 5-13). Differences occur in amplitude and phase of the normal force variation. The deviations seem to increase with angle of attack. The most likely cause for these differences is dynamic stall effects, which are known to be a source for deviations between calculations and measurements. Using a dynamic stall model leads to only a minor improvement in results. As such, a more detailed analysis of dynamic stall effects should be done, using measurements recently taken in the MEXICO project. These measurements were taken on a model rotor with a diameter of 4.5 m in the German Dutch Wind Tunnel (DNW). Among others, pressure measurements at a very high sampling rate (5 kHz effectively) have been taken together with measurements of the flow field around the blade.

Table 5-2. Contribution to sectional yawing moment, measured and calculated by AWSM and PHATAS at V_{tun}= 5 m/s, yaw angle = 30°, and pitch angle = 0°

	$dM_{yaw,30}$	$dM_{yaw,47}$	$dM_{yaw,63}$	$dM_{yaw,80}$	$dM_{yaw,95}$
Measurements	6.9	6.3	-6.6	-24.0	-39.8
AWSM	3.9	4.7	-4.9	-27.9	-41.0
PHATAS	8.0	15.0	5.7	-34.1	-102.0
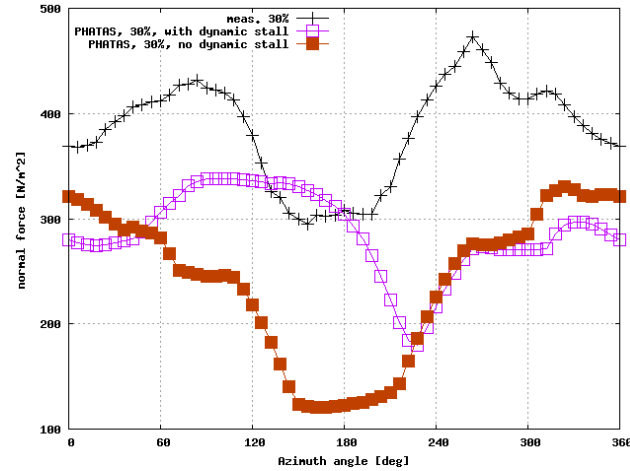
Figure 5-13. V$_{tun}$ = 15 m/s, θ = 0°, and yaw angle = 30°: Normal force at 0.30R as function of azimuth angle: Calculated by PHATAS with and without dynamic stall

The study on dynamic inflow considered fast pitching steps from –5.9° to 10° (i.e., an upward pitching step) and vice versa. At a tunnel speed of 5 m/s, strong dynamic inflow effects appear in the normal forces at all radial positions. Figure 5-14 shows a clear overshoot followed by a gradual approach of the new equilibrium values. As explained in Snel and Schepers (1994), such behavior is typical for dynamic inflow.
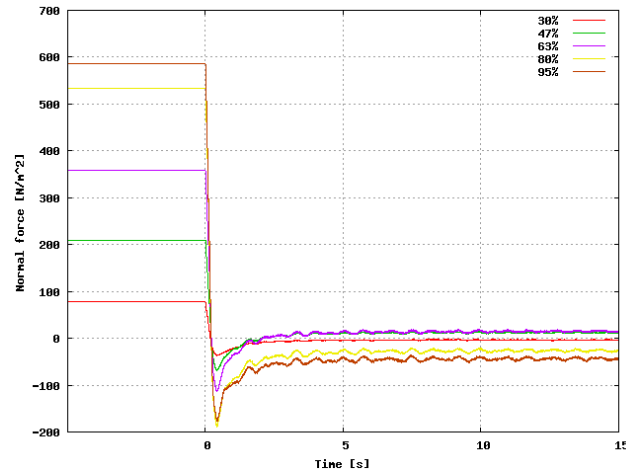
Figure 5-14. Measured normal force at five radial positions for the upward pitching step

The upward pitching step is much more suitable for studying dynamic inflow effects than the downward pitching step. For the downward pitching step, the angle of attack exceeds the stall angle of attack. The analysis of dynamic inflow effects is then complicated by the uncertainties that result from the stall effects.

The agreement between the measured results and the calculated results from the newly developed free wake lifting line model AWSM (for the upward pitching step) was excellent in terms of equilibrium values, overshoots, and time constant. Figure 5-15 compares measured normal force during upward pitching step and normal force calculated by AWSM for the 47% and the 80% span.
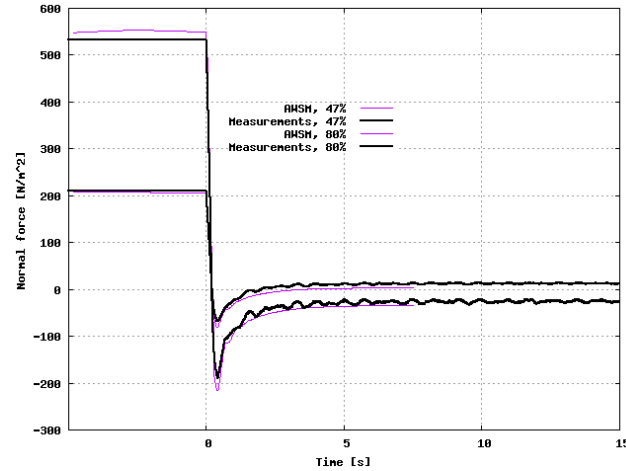
Figure 5-15. Comparison between AWSM calculated and measured dynamic inflow transient

Because dynamic inflow effects were measured at different radial positions, the present measurements allowed, for the first time ever, an assessment of the radial dependency on the dynamic inflow effect. Table 5-3 shows the time constants as derived from the measured transients in normal force, the AWSM calculated transients, and the engineering model implemented in PHATAS. The time constant in the measured and AWSM results hardly reduces toward the tip. This is opposite from the expectations from previous projects on dynamic inflow (Snel and Schepers, 2004) and from the results from the engineering model. A similar study on the recent MEXICO measurements should investigate the radial dependency of the time constant for that configuration. Thereafter, if necessary, the time constants in the engineering models on dynamic inflow need to be adjusted.

Table 5-3. Time constant for different radial positions at dynamic inflow transient

Radial Position	f_{meas} [s]	f_{AWSM} [s]	$f_{engineering\ model}$ [s]
30%	0.94	1.12	0.93
47%	0.83	1.04	0.83
63%	0.76	1.04	0.68
80%	0.73	1.00	0.44
95%	0.77	1.03	0.14

5.5 Conclusions and Future Work

NREL's measurements in the NASA-Ames tunnel presented a unique opportunity to investigate different aerodynamic aspects and to validate wind turbine design codes. Local aerodynamic quantities (pressure distributions, normal forces, and tangential forces) were obtained at different radial positions under controlled and stationary conditions. The present analysis examined nonyawed conditions, yawed conditions, and dynamic inflow effects at fast

pitching steps. The measurements at these conditions were compared with the wind turbine design code PHATAS and the free wake lifting line code ASWM. To recap the results,

- At nonyawed conditions, the agreement between PHATAS calculated results and measurements is generally good, as long as the tunnel speed is low (< 10 m/s), although some differences appeared at the outer part of the blade (95% span). Furthermore, differences appeared at high angles of attack (high tunnel speeds). Although the 3D model on the lift coefficient, as implemented in PHATAS, does improve the agreement with the measurements, this correction needs to be "amplified." Furthermore, a correction on the drag is needed.

- At yawed conditions (and low tunnel speeds), a clear influence from the skewed wake on the induced velocity appears, which in turn affects the normal forces variation with azimuth angle.

- At yawed conditions and low tunnel speeds (i.e., relatively high induction factors), some discrepancies appear between the PHATAS results and the measurements, but opposite to common engineering models, PHATAS does predict a destabilizing yawing moment contribution at the inner part of the blade in agreement with the measured results.

- At yawed conditions and high tunnel speeds, the agreement between the PHATAS results and the measurements is poor. Using the dynamic stall model as implemented in PHATAS does not improve the results.

- At fast pitching steps, clear dynamic inflow effects were observed as an overshoot in the measured normal force, followed by a gradual approach of the new equilibrium value.

- The results from the AWSM code are very similar to the results of the PHATAS code, and therefore the agreement between AWSM results and the measurements can generally be considered good as well. Where the PHATAS code performs more poorly and where the induction is significant (e.g., at the outer part of the blade, at yawed conditions or at dynamic inflow), however, the agreement from the AWSM code is much better and sometimes even excellent.

The present study considered data only at the default configuration with a rotor radius of 5 m and a rotational speed of 72 rpm. Some measurements, however, were also taken on an extended blade (radius 5.5 m) and at a higher rotational speed (90 rpm). These measurements are still unexplored. The measurements at an extended blade can help derive better tip correction models, and the measurements at a higher rotational speed may provide additional information on phenomena that are related to high induction factors. Related work should also use the recently available MEXICO measurements. These measurements are taken on a 4.5-m diameter rotor in the DNW wind tunnel (Snel et al. 2007). Absolute pressure measurements around the blade at 5 kHz were taken along with PIV (particle image velocimetry) measurements on the flow field. These measurements will provide additional insights on, e.g., dynamic inflow, dynamic stall, yawed conditions, and tip effects.

5.6 Bibliography

Lindenburg, C. (2003). *Investigation into Rotor Blade Aerodynamics: Analysis of the Stationary Measurements of the UEA Phase IV Rotor in the NASA-Ames Wind Tunnel.* ECN-C-03-025. Petten: ECN.

Schepers, J.G. (1999). "An Engineering Model for Yawed Conditions Developed on the Basis of Wind Tunnel Measurements." Presented at the ASME Wind Energy Symposium, Reno, Nevada, American Institute for Aeronautics and Astronautics, January.

Schepers, J.G. (2007a). *IEA Annex XX: Comparison between Calculations and Measurements on a Wind Turbine in the NASA-Ames Wind Tunnel.* ECN-E-07-066. Petten: ECN.

Schepers, J.G. (2007b). *IEA Annex XX: Comparison between Calculations and Measurement on a Wind Turbine in Yaw in the NASA-Ames Wind Tunnel.* ECN-E-07-072. Petten: ECN.

Schepers, J.G. (2007c). *IEA Annex XX: Dynamic Inflow Effects at Fast Pitching Steps on a Wind Turbine Placed in the NASA-Ames Wind Tunnel.* ECN-E-07-085. Petten: ECN.

Schepers, J.G.; Snel, H. (1995). *JOULE2: Dynamic Inflow: Yawed Conditions and Partial Span Pitch.* ECN-C-95-056. Petten: ECN.

Schepers, J.G. et al. (1997). *Final Report of IEA Annex XIV Field Rotor Aerodynamics.* ECN-C-97-027. Petten: ECN. Available at http://www.ecn.nl/wind/other/IEA/index.en.html.

Schepers, J.G. et al. (2002). *Final Report of IEA Annex XVIII Enhanced Field Rotor Aerodynamics Database.* ECN-C-02-016. Petten: ECN. Available at http://www.ecn.nl/wind/other/IEA/index.en.html.

Schepers, J.G.; Snel H.; van Garrel A. (2005). "Dynamic Inflow Effects in NASA-Ames Measurements; Radial Dependency and Comparison with Free Wake Lifting Line Model AWSM." Presented at IEA Annex 11/20 meeting, Pamplona, Spain, May.

Schepers, J.G.; Feigl, L.; Van Rooij, R.; Bruining A. (November 2004). "Analysis of Detailed Aerodynamic Field Measurements using Results from an Aeroelastic Code." *Journal of Wind Energy* (7:4); pp. 357–371.

Snel, H. (1997). "Heuristic Modelling of Dynamic Stall Characteristics." Pages 429–433 in *Proceedings of the EWEC 1997 Conference, Dublin, October.*

Snel, H.; Schepers, J.G. (December 1994). *JOULE1: Joint Investigation of Dynamic Inflow Effects and Implementation of an Engineering Method.* ECN-C-94-107. Petten: ECN.

Snel, H.; Schepers, J.G.; Montgomerie, B. (2007). "The MEXICO Project (Model Experiments in Controlled Conditions): The Database and First Results of Data Processing and Interpretation." In *Proceedings of EAWE conference on The Science of Making Torque from the Wind.* Available at http://www.iop.org/EJ/toc/1742-6596/75/1.

Snel, H.; Houwink, R.; Bosschers, J. (May 1993). *Sectional Prediction of Lift Coefficients on Rotating Wind Turbine Blades in Stall.* ECN-C-93-052. Petten: ECN.

van Engelen, T.G.; van der Hooft, E.L. (November 2004). "Dynamic Inflow Compensation for Pitch Controlled Wind Turbines." In *Proceedings EWEC conference, London, 22–25 November 2004* (on CD-ROM).

6.0 Research Summary—The Netherlands, Delft University of Technology

Organization: Delft University of Technology

Researchers: R.P.J.O.M. van Rooij, R.P.J.O.M.vanRooij@tudelft.nl
E.A. Arens
G.J.W. van Bussel, G.J.W.vanBussel@tudelft.nl
G.A.M. van Kuik, G.A.M.vanKuik@tudelft.nl
F. Meng, F.Meng@tudelft.nl
T. Sant, tonio.sant@um.edu.mt

6.1 Background and Motivation

Motivation concerning the National Aeronautics and Space Administration (NASA) Ames database and this International Energy Agency (IEA)Annex XX is twofold: first, to research the flow around the blade and its corresponding loads and second, to validate numerical approximations of blade and rotor loads.

The first approach starts with carefully unraveling the characteristics to understand the flow behavior. Then determining a proper inflow angle plays a key role. A simple adjustment of the measured flow probe angle is proposed, but also a more comprehensive method was derived using a free vortex wake model. The method could be of great value in particular for stalled and yawed conditions. The newly obtained blade characteristics are compared with other model measurements like field experiments (part of IEA Wind Annexes XIV and XVIII) but also Sweden's FOI wind tunnel experiments (in the CARDC (China Aerodynamics Research and Development Center)) and the recent measurements from the MEXICO (Model Rotor Experiments In Controlled Conditions)partners (EU project) in the DNW [Au: please define], Netherlands. Such gives insight in aeroelastic behavior and shows dependencies in the rotor configuration (rpm and pitch angle), blade geometry (chord and twist distribution), and airfoil characteristics. Delft University of Technology investigated rotating and nonrotating configurations.

Most studies, however, focus on validating and developing numerical tools. The blade element momentum (BEM) methods are still the most common methods used to predict the aerodynamics loads of wind turbine blades. These codes rely on proper input characteristics. The database helps to understand and approximate rotational augmentation and in verifying the constants in "classical" stall models. Delft University also investigated validating the results from more sophisticated aerodynamic methods such as full Navier-Stokes codes with proper physical description .

The contributions of Delft University of Technology are described briefly and three areas are highlighted:

1. Investigating the Unsteady Aerodynamics Experiment (UAE) measurements (abbreviated hereafter as "UAE")

2. Estimating Angle of Attack from Blade Pressure Measurements on the NREL Phase VI Rotor using a Free-Wake Vortex Model (abbreviated as "Free-Wake Vortex Model")
3. Engineering Models versus CFD Methods with respect to augmented lift caused by blade rotation (abbreviated as "Engineering versus CFD")

All research under the Annex XX has been published in conference proceedings, expert meeting, and journals, and listed in the bibliography of this section.

6.2 The UAE Measurements

This study investigated the rotating experimental data from the UAE experiment designated as B, H, and S series. The analyses examined the steady-state conditions and a selection was made from these data containing for Yaw = 0^0 and U = all wind speeds with special emphasis on 5, 6, 8, 10, 12, 13, 14, 15, and 20 m/s.

The study of the parked conditions (not described here) was based on the nonrotating data. These campaign data were more detailed than those available on the website and sent by the Annex XX Operating Agent Representative S. Schreck. The study was extended with the nonrotating configuration of the FOI measurements carried out on a STORK WP5 blade in the LT1 low speed wind tunnel (in Stockholm, Sweden).

6.2.1 UAE Research Results
The research on the rotating measurements focused on the variation in flow behavior and quality of the dataset. This was combined with finding the most representative average steady-state data. The effects of the test set-up were one of the first issues to be investigated. To quantify these effects, the rigid blade conditions (H sequence) at a relatively low wind tunnel speed were chosen because the corresponding attached flows respond promptly to small variations in tunnel speed, revolution speed, and pitch changes. This procedure, however, does not give any information on the accuracy of the measurement system itself.

Researchers investigated all segment sections, and the 30% and 80% span locations represent the overall findings quite well. Within one measurement campaign the rotor speed was (almost) constant at 72 rpm and the effect of tunnel speed variations were relatively small. The fluctuations in pitch angle were limited to approximately ±0.4°, representing a variation of about ±0.04 in Cn in an attached flow.

With the installed pressure system, researchers collected information about the local flow angles and pressure distributions. From this the stagnation pressure, normal and tangential force coefficients could be derived, giving information on variation in flow behavior.

Figure 6-1 shows the variation in C_n with tunnel speed, and the error bars represent the minimum and maximum values of the binned averages. Variation in C_n increases with tunnel speed, and beyond a velocity of 12 m/s the error bars become quite considerable. This is in particular true at the inboard segment where the flow is dominated by large turbulent separated areas. This is consistent with the pressure distributions, which indicate leading edge separation at the inboard segment starting at 12 m/s tunnel speed. Also the accompanying large LFA (local inflow angle) values indicate that large inflow angles can be expected.
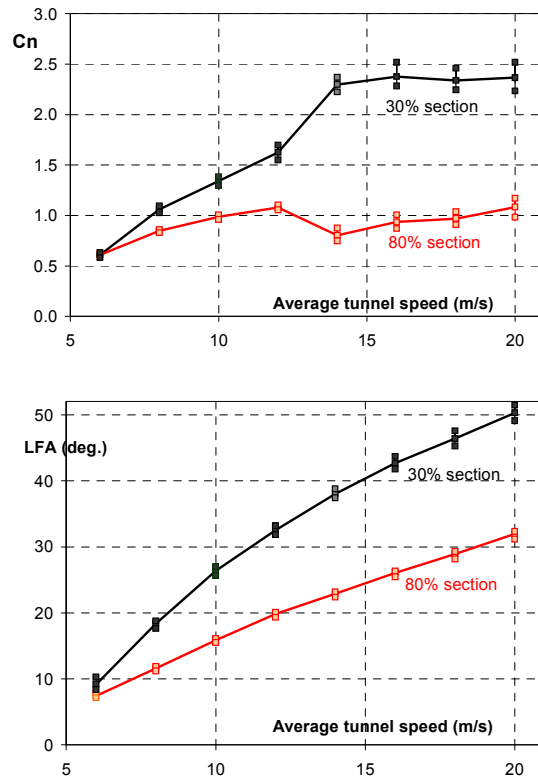
Figure 6-1. Variation of C$_n$ and local flow angle (LFA)

The variation in normal force coefficient can largely be attributed to the set-up, and Figure 6-2 shows a representation along the azimuth angle. An inquiry with an FFT procedure show the dominant 1P (1.2 Hz) in the power spectra and corresponds with the blade passing frequency of the instrumented blade.
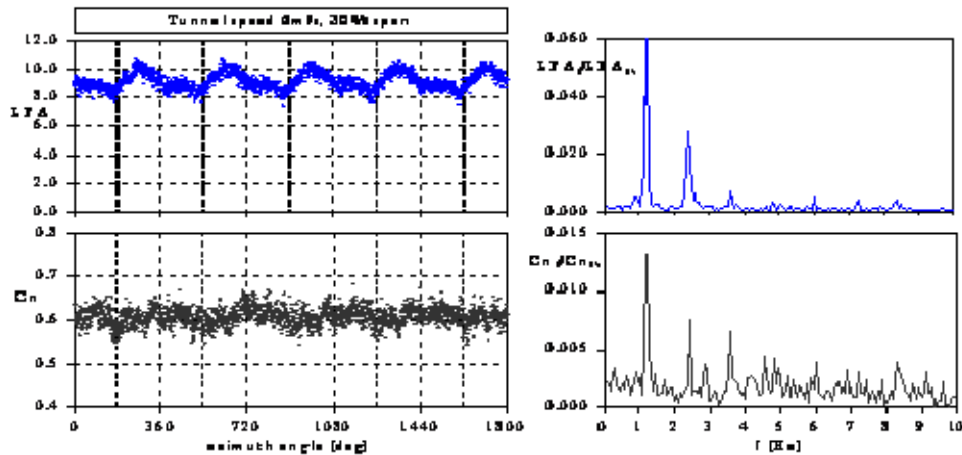
Figure 6-2. Behavior of local flow angle and Cn with azimuth angle (a period) and as power spectra for inboard span position

A 2P peak is also very clear at the inboard segment, and this represents the blade passing frequency of the rotor, which has two blades. This suggests that the instrumented blade is affected by the noninstrumented blade passing the tower. Structural quantities of the rotor or the control system, which could not fully switched off, could have provoked this. The influences of the tower are smaller, less pronounced, and toward the outboard span locations. Higher local velocities and a smaller shadow area probably cause this behavior. At tunnel speeds beyond 12 m/s, the variations in C_n and LFA are more random and no clear resonance frequency in the power spectra could be observed. This indicates that flow disturbances caused by flow separation are dominating the flow.

The preceding analysis clearly shows that the set-up affects the acquired data and that representative characteristics for the steady-state nonyawed conditions are not easy to distinguish. Arranging the measurements along the azimuth angle show some alarming behavior, in particular for LFA between 270° and 360° azimuth angle at the inboard segment (Figure 6-3). This is surprising because only the area coinciding with the tower was expected to be disturbed, which is more or less true at the outboard span position. Comparable behavior was detected for the other segments as well and was consistent for all tunnel speeds. It seems that steady behavior of the local flow angle and normal force coefficient, the most important parameters of the characteristics, is achieved in the first quadrant of the rotor plane only.
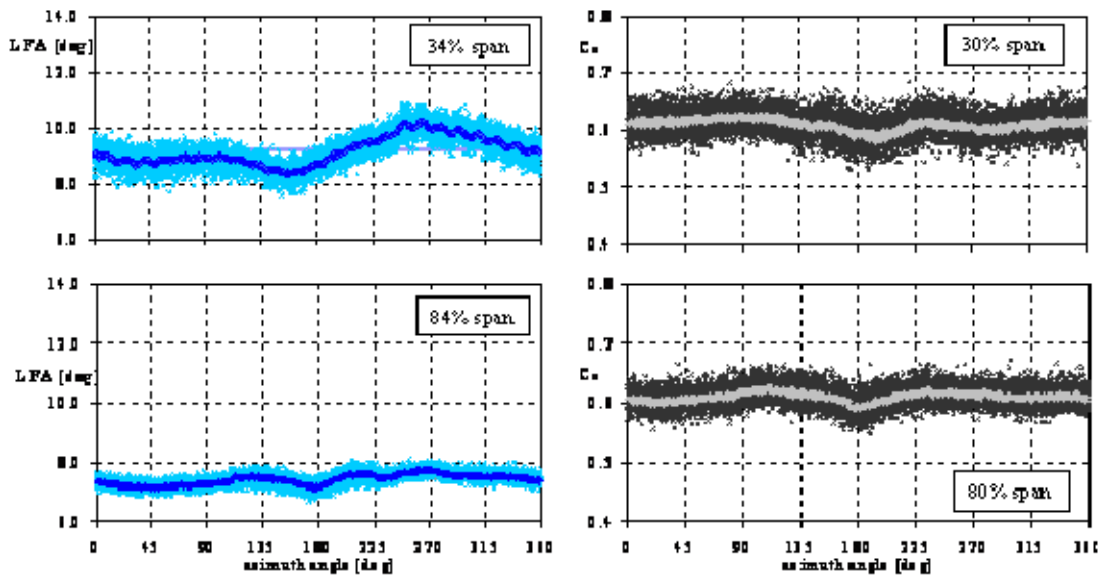
Figure 6-3. The behavior of the local flow angle and normal force coefficient averaged per azimuth angle for the inboard and outboard position

6.2.2 UAE Conclusions and Future Work
Analysis of the UAE data series in the configuration with rigid blade, no cone angle, no yaw, and upwind rotor on the attached blade flow revealed the following:

- The 1P and 2P blade passing frequencies can be observed in almost all aerodynamic parameters for the four investigated span locations and is caused by the downwind tower. The variations are most pronounced at the inboard segment.

- The first quadrant of the rotor plane showed the most steady average aerodynamic behavior and should be used by preference to distinguish the characteristics at the span locations along the blade.

Applying the recommendations still left some doubts concerning the inflow angle at the 47% and 63% span locations. Further investigations of the normal force coefficient in the nonrotating, parked configuration showed similar deviations at those locations, and so an additional correction for LFA at these two segments is proposed: 3° at the 47% span segment –and 1°at the 63% span segment.

6.3 The Free-Wake Vortex Model

6.3.1 Estimating the Angle of Attack from Blade Pressure Measurements on the NREL Phase VI Rotor using a Free-Wake Vortex Model

This study used the experimental data collected from the NREL Phase VI rotor when operating in the S configuration in the NASA Ames wind tunnel. The analysis was performed at various wind speeds, yielding attached and stalled flow conditions over the blades. Both axial and yawed rotor conditions were studied, as follows:

- Yaw = $0°$ and $U = 5, 7, 10, 13, 15, 20$, and 25 m/s

- Yaw = $30°$ and $U = 5, 7, 10, 13$, and 15m/s

A novel and comprehensive method involved using the blade pressure measurements with a free wake vortex model to estimate the angle of attack (definition given in Figure 6-4) at the blades more accurately, together with the induced velocity distributions at the rotor plane and the wake geometry.

$$C_l = C_n \cos \alpha + C_t \sin \alpha$$
$$C_d = C_n \sin \alpha - C_t \cos \alpha$$

Figure 6-4. Blade section aerodynamic load coefficients

This method consisted of the following sequence of steps: Initially, a spanwise distribution for the angle of attack was assumed as well as C_n and C_t, which were used to determine the lift coefficients at the blades. Using the Kutta-Joukowski law, the bound circulation distribution at the b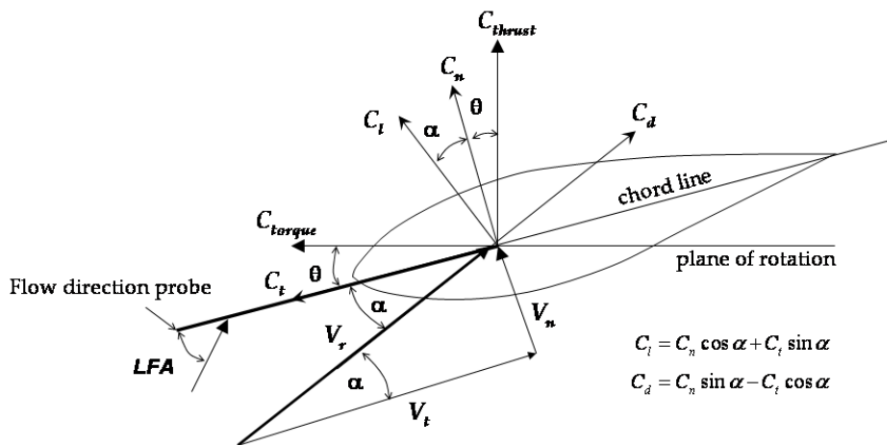lades was determined and prescribed to the free wake vortex model to generate the free vortical wake. The induced velocity at the blades was estimated and used to calculate a new angle of attack distribution. The process was repeated until convergence in the angle of attack was achieved. One advantage of this method is that the solution is itself unsteady and could be readily applied to yawed conditions, under which complex aerodynamic phenomena are known to occur (e.g., dynamic stall and unsteady induction). A second advantage is that because the wake geometry is inherently part of the solution, it is possible to derive the pitch and expansion of the helical wake from the measured C_n and C_t.

Delft University of Technology created the free wake code. The code models rotor wakes in both axial and yawed conditions from knowledge of the aerodynamic loads on the blades. The input to the code is a prescribed spanwise distribution of bound circulation instead of the usual airfoil characteristics. From this prescription, the code generates the lifting line values and the vortex wake sheets and calculates the 3D induced velocities at the rotor plane. The near wake consists of vortex sheets, one per blade, modeled as a mesh of straight line vortex filaments to account for trailing and shed vorticity. The far wake model consists of a helical tip vortex at each blade, representing the fully rolled up tip vortices. Each helical tip vortex is attached to the outboard end of the corresponding near wake. It is assumed that, at the transfer of the near to the far wake model, each near wake vortex sheet rolls up immediately into a concentrated tip vortex. This assumption is not physical but yielded accurate predictions for the inflow at the rotor plane and near wake geometry in a validation study on the subject free wake vortex model.

6.3.2 Free-Wake Vortex Model Research Results

Figure 6-5 shows the converged angle of attack distributions for axial conditions at yaw $0°$. The figure also shows experimental values for the local inflow angles at the probe tips at each wind speed, as well as the large differences between the computed angle of attack and the measured LFA results.
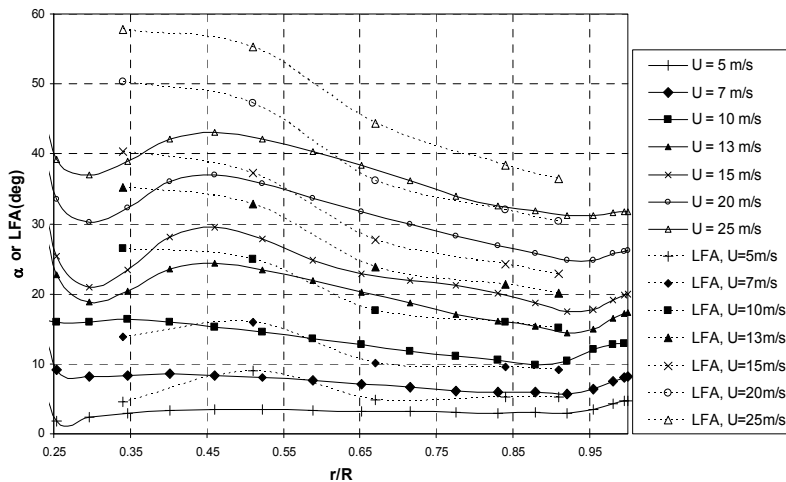
Figure 6-5. Converged angle of attack distributions at different wind speeds for Yaw $0°$. The LFA values measured with the probes are also shown.

49

Figure 6-6 summarizes the aerofoil data derived from the measured values of C_n and C_t and the angle of attack distributions of Figure 6-5. Both the lift and drag coefficients depend on the radial location. The 2D Delft wind tunnel data for the S809 aerofoil are plotted for a Reynolds number of 1 million.
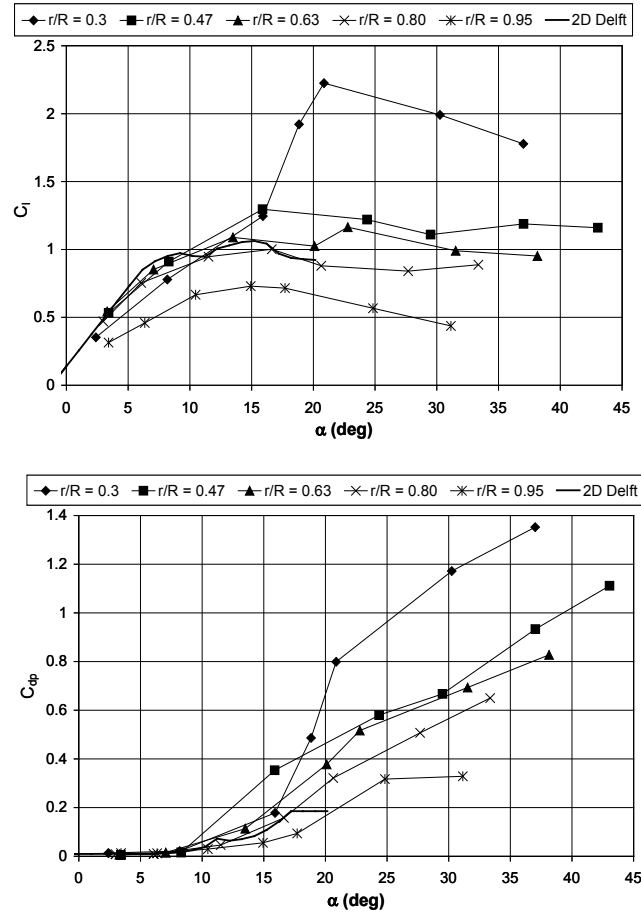
Figure 6-6. Derived lift and drag coefficients for different radial positions for Yaw 0°

The derived lift and drag coefficients were used together with the calculated induced velocities at the blades to calculate the low-speed shaft torque (LSSTQ) and the blade root-edge moments (RFM and REM). These were compared with those measured experimentally using strain gauges (Figure 6-7a–c). The latter are plotted together with the corresponding ±1 standard deviations. The cyclic gravitational loads caused the large standard deviations in the REM. The aerodynamic loads were also derived directly from the pressure measurements by calculating the torque and thrust coefficients at each blade element and integrating across the whole blade. These compared very well with those calculated by the free wake code but not so well with those measured with strain gauges. Most probably this is mainly the result of errors in the measured values of C_t.

50
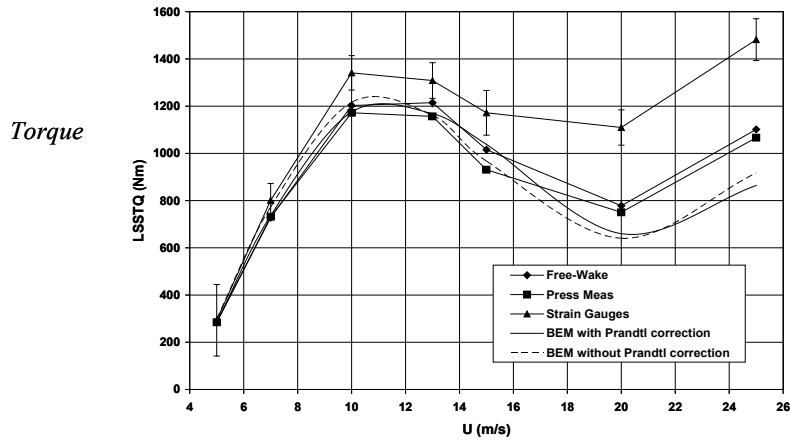
Fig. 4(a): Variation low speed shaft torque with wind speed
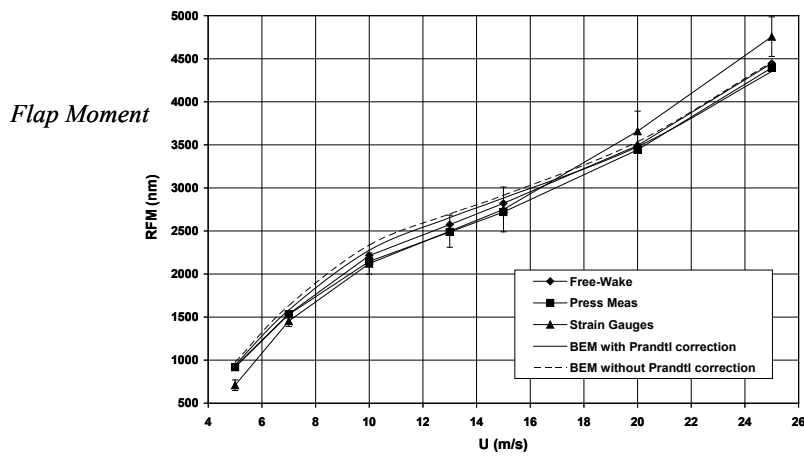
Fig. 4(b): Variation of blade root flap moment with wind spee
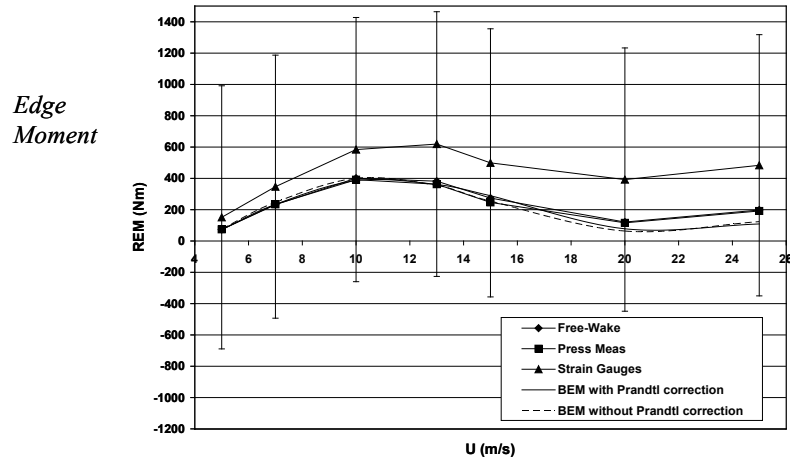
Figure 6-7. Torque, flapping moment, and edge moment in relation to tunnel speed

Finally, the derived C_l-α and C_d-α data were used in a BEM model to compute the same global loads. Whether to include the Prandtl tip/root loss factor or not did not have a significant difference on the global load predictions.

51

For yawed conditions at 30°, Figure 6-8(a,b) illustrates the converged angle of attack variations with the blade azimuth angle at $U = 10$ m/s and the measured LFA values. Large differences exist between the angle of attack and the corresponding LFA values at all azimuth positions of the blades, similar to what was noted in axial conditions. Yet in yawed conditions, the probe was subjected to highly unsteady flow situations. At $U = 10$ m/s, the
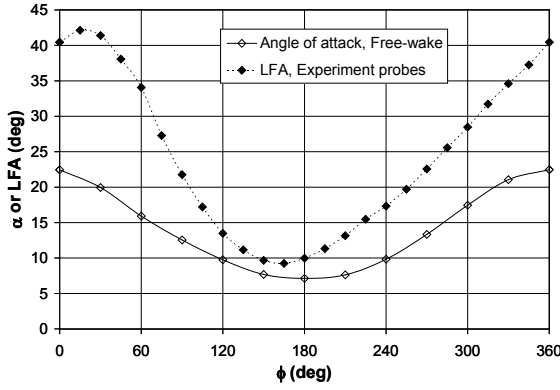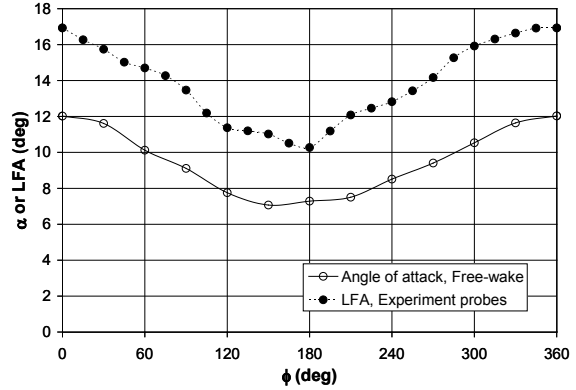
Fig. (a): r/R= 0.34   Fig. (b): r/R= 0.84

Figure 6-8. Derived angle of attack variations derived for U = 10m/s, yaw 30˘. The LFA values measured using the probes are shown.

free wake model estimated that the time rate of change of angle of attack reaches a peak of about ±78°/s at the inboard sections. Further work is required to establish the accuracy with which five-hole pressure probes manage to measure the LFA at such high levels of unsteadiness.

From the variations of C_n and C_t obtained from the blade pressure measurements and the results for the angle of attack presented in Figure 6-8, researchers could derive the unsteady aerofoil hysteresis loops for C_l-α and C_{dp}-α. Figure 6-9(a–d) illustrates the hysteresis loops for different radial locations at $U = 10$ m/s, yaw 30°. The figure also shows 2D steady aerofoil data obtained from the Delft wind tunnel experiments and the 3D steady aerofoil data were derived from the blade pressure measurements for nonyawed conditions together with the free wake code. In a yawed rotor, these loops are not only a result of the cyclic angle of attack variations but also caused by a cyclic variation of the flow velocity relative to the blades. Each hysteresis plot includes the reduced frequency k - ($k = \Omega c/(2V_r)$). The hysteresis loops often change direction from counterclockwise to clockwise when moving outboard from $r/R = 0.3$ to 0.95 (see Figure 6-9).

6.3.3 Free-Wake Vortex Model Conclusions and Future Work
A free-wake vortex model can be used to derive the angle of attack at the blades from blade pressure measurements in both axial and yawed conditions. Using the derived angle of attack and the measured C_n and C_t values can help generate complete three-dimensional (3D), steady and unsteady aerofoil data.
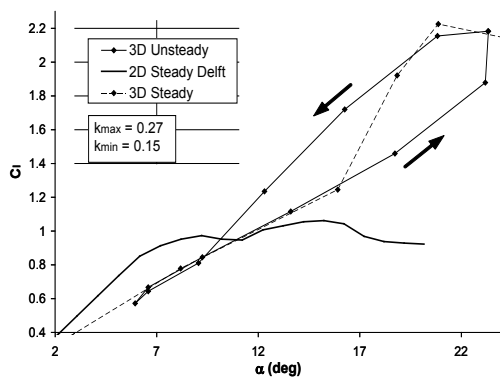
Fig. (a): r/R= 0.3
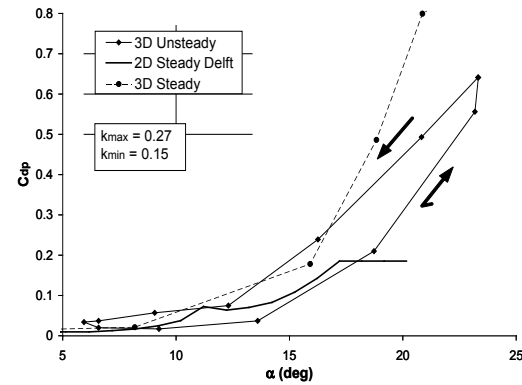
Fig. (b): r/R= 0.3
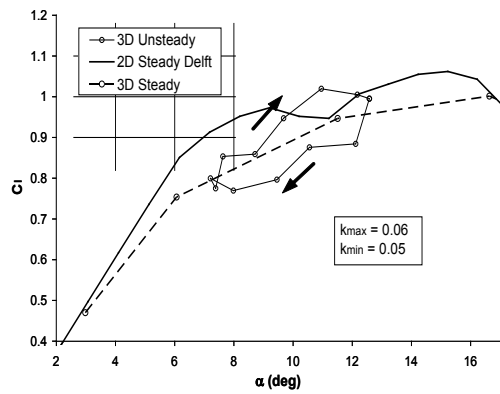
Fig. (c): r/R= 0.8
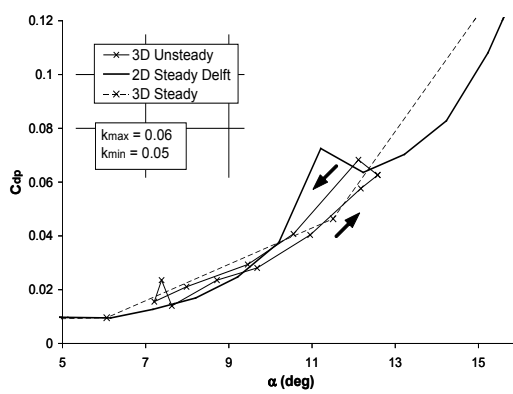
Fig. (d): r/R= 0.8

Figure 6-9. – C_l-α and C_d-α hysteresis loops for U = 10 m/s, yaw = 30°

For axial conditions in which the angle of attack is steady, the following conclusions could be made:

- For small angles of attack (less than the 2D static stalling angle), the new 3D aerofoil data are very close to the 2D aerofoil data except at the tip and root region. In the latter regions, the new 3D lift coefficient was lower than the 2D aerofoil data.

- For larger angles of attack, the new 3D aerofoil data were considerably different than the 2D data and the presence of stall-delay was evident, especially at the inboard sections of the blades. The increase in lift coefficient caused by stall delay was accompanied by an increase in drag coefficient.

For yawed conditions in which the local angle of attack is unsteady and a function of the blade azimuth angle, the following conclusions could be drawn:

- The 3D unsteady coefficients could well exceed the corresponding steady values derived for axial conditions.

- The unsteady C_l-α and C_{dp}-α hysteresis loops were in general closer to the 3D steady values than to the corresponding 2D steady data. This was observed at both attached and stall conditions, and it implies that 3D effects (in particular stall-delay) have a significant role in the unsteady flow behavior of wind turbine blades.

A free-wake vortex model can also derive the complex 3D induction at the rotor plane together with the wake geometry and circulation distribution from the blade pressure measurements. These are vital for a better understanding of a wind turbine's aerodynamic behavior in both steady and unsteady environments.

With reliable 3D aerofoil data, BEM predictions for wind turbines improve significantly, even for conditions of deep stall and rotor yaw. In many situations, BEM results for the blade aerodynamic loading distributions are unreliable, not necessarily because the BEM theory is deficient but because incorrect aerofoil data are used.

When using 3D lift and drag aerofoil data derived directly from the blade pressure measurements, the BEM calculations no longer require the tip/root loss correction model. This is because the tip/root loss effects are already accounted for in the 3D aerofoil data.

This study clearly demonstrated the considerable potential to improve the accuracy of BEM-based aerodynamic models. Wind turbine designers urgently need more reliable engineering models that predict 3D aerofoil data. Research efforts should focus on a better understanding of the flow physics locally around the rotating blades. More extensive blade pressure measurements would be indispensable to reaching this aim and further validating CFD models. The limited availability of accurate 3D aerofoil data for wind turbine applications restricts not only BEM-based models from being more accurate but also the more comprehensive models such as lifting-line free-wake vortex models and lifting-line/actuator-disk CFD models.

6.4 Engineering versus CFD

This work applied the rotating UAE data designated as H and S series, in particular, the first quadrant of the rotor plane for yaw $= 0^{\circ}$ and $U =$ all wind speeds with special emphasis on 5, 8, 10, 12, 13, 14, 15, and 20 m/s.

Blade loads and rotor performances of wind turbines in the rotating case can be approximated with engineering methods and sophisticated aerodynamic codes. The engineering methods are based on 2D aerodynamic performances and result in a spanwise related adjustment. The newly generated segment performances can than be used to calculate blade loads and performances via BEM theory or vortex lattice-like techniques. The aerodynamic calculations include at least local blade shape and (local) flow physics. A well-known program, the panel code RFOIL, has an integral boundary layer description and includes a cross-flow model. It can be regarded as a quasi-3D code and the calculated segment characteristics are still independent of neighboring span sections. Full Navier-Stokes codes (or full CFD like FLUENT), however, include a full description of the blade geometry and the entire flow field and simulate the rotor environment properly. Aerodynamics influences in spanwise direction are considered and nacelle layout and tower presence can be modeled.

This comparison looked at the experimental data of the steady-state NREL Phase VI blade configuration versus some engineering models and CFD methods; several articles in the bibliography of this section describe results of other blade configurations.

6.4.1 Engineering Models versus CFD Research Results

Most engineering stall models adjust the 2D airfoil characteristics for rotation and are based on the idea of Snel et al., in which the (c/r) dependency plays a dominating role. They express the 3D correction of, for example, the lift coefficient as a fraction of the difference in C_l between the inviscid or extended linear 2D lift. Chaviaropoulos and Hansen included twist and pitch in their base equation for the rotational characteristics, which reads as:

$$C_{x,3D} = C_{x,2D} + A\ (c/r)^B * \cos^n(\text{twist+pitch}) * C_x$$

where x is the lift (or normal force coefficient):

$$C_x = C_{l,INV} - C_{l,2D}$$
or
$$C_d = C_{d,2D} - C_{d,2D\text{-min}}$$
$$C_m = C_{m,2D} - C_{m,INV}$$

The most important approaches are given by:

- Snel: A = 3, B = 2, n = 0

- Chaviaropoulos and Hansen: A = 2.2, B = 1, n = 4

- Schepers and van Rooij: A=2.93, B=1.18, n=6

These constants were calculated from a limited amount of measurements, and therefore the applied experiments could play a rather dominant role in the value of these parameters. Figure 6-10 shows the results for the three engineering models compared with the UAE measurements for two span locations.
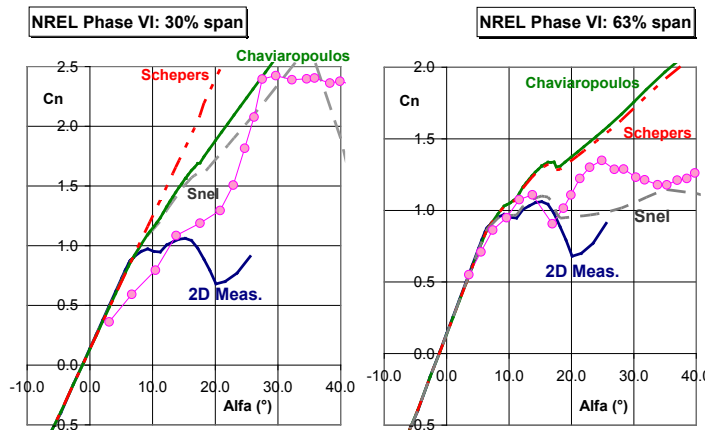
Figure 6-10. The NREL wind tunnel results for tapered and twisted blade compared with the stall model predictions for two sections (circles are UAE measurements)

55

At the inboard segment the approximated normal force coefficient extends (by definition) from the 2D measurements, and the measurements strongly deviate. This could be caused by the influence of the transition piece toward the hub, which is very close to the measured segment. For the midspan position, two engineering methods show a huge increase in C_n compared with the measurements, but the Snel option does not show such behavior. In general, the prediction of the maximum normal force coefficient is exaggerated, and the methods fell short, leading to an improper prediction of the actual loads and accompanying power performances. These observations are similar for the other blade sections.

The CFD code RFOIL is a modification of panel code XFOIL extended for radial flow based on the Snel-Houwink model for blade rotation, and therefore includes the 3D velocity profile of Johnson. This velocity model, however, cannot handle negative velocities and separation cannot be modeled adequately. To activate "rotation," the local solidity parameter c/r serves as input and two thirds of the geometric value gives the best approximations. Figure 6-11 gives the results compared with the wind tunnel measurements of phase VI. The normal force predictions are fairly good except for the r/R=0.30 segment, and local flow influences from the transition piece could obscure the measurements. The sharp nose in combination with the integral boundary layer solution leads to convergence problems near the nose, and this hampers calculation up to large angles of attack. Thicker airfoils, which are common at inboard segments, improve convergence, and characteristics up to 35° are in general possible.
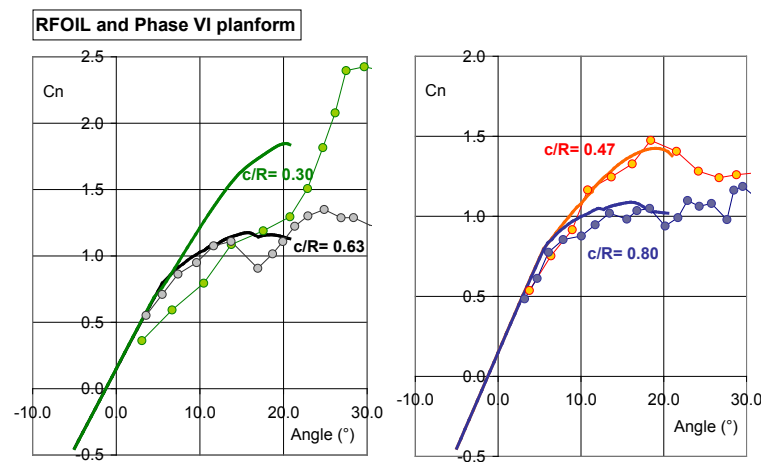
Figure 6-11. The RFOIL predictions compared with the wind tunnel results at four span sections

Investigators used full Navier-Stokes codes to model the rotating blade without nacelle and tower. Risoe and the Delft University of Technology performed the calculations with, respectively, EllipSys3D and the commercial code FLUENT. The conditions were as follows:

- EllipSys3D:
  - Grid: 3.1×10^6 cells, domain is half sphere with radius of 6R
  - Turbulence model: fully turbulent and unsteady k-ω SST model, with maximum y^+ = 2

- FLUENT:
  - Grid: 3.6×10^6 cells, domain is half sphere with radius of 6R
  - Turbulence model: fully turbulent and k-ω SST model, with maximum $y^+ = 2$

Risø always applied the unsteady k-ω SST model, and Delft used the steady description for wind speeds less than 12 m/s and the unsteady k-ω SST model up to 15 m/s. The differences between the steady and unsteady result turned out to be small for the range of wind speeds considered. The huge difference in limited streamlines at a tunnel speed of 10 m/s (Figure 6-12) is thus remarkable. Most interesting is the curved vortex shape near the 47% segment. Both front parts of the blade indicate an attached flow, and turbulent separation is about 50%–55% with EllipSys3D and slightly more in front with FLUENT.

Phase VI, 10m/s

EllipSys3D
Unsteady k-w SST

FLUENT
Steady k-w SST
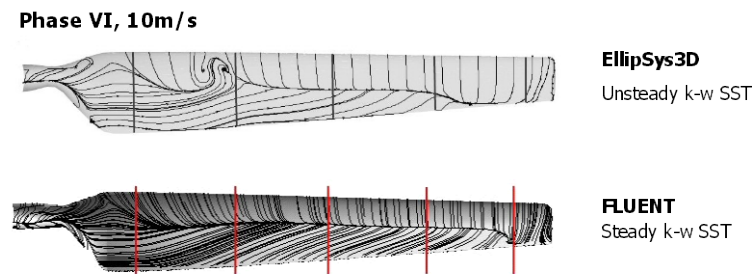
Figure 6-12. Limited streamlines on the suction side of the Phase VI blade. Vertical lines indicate the measured sections.

This explains why the differences in normal force coefficient, derived from the pressure distributions, do not deviate much between the two codes. Figure 6-13 shows a comparison of the normal force coefficients for several wind speeds (10, 13, and 15 m/s) along the blade span. Behavior and deviations in values and trends are very similar. The calculated and measured pressure distributions (not shown here) show that integral information such as C_n can be misleading because variation and deviations in pressure distributions near the nose can be cancelled out by the differences at the tail. Most of the calculated pressure distributions are quite comparable, however, and comparing the normal force coefficient with the measurements gives a fair indication of the quality of nowadays CFD codes.

To get around the uncertainty of the inflow angle, the tunnel speed is chosen as reference; Figure 6-14 depicts the development of the normal force coefficient for the five span segments. The prediction of C_n at segment r/R=0.30 is remarkably good, but the segments at midspan (r/R=0.47 and r/R=0.63) are quite surprising. The dip in the FLUENT results at 13 m/s at r/R=0.80 cannot be observed in the experiment, and it is not clear why. The calculated outboard performance at r/R=0.95 was mostly larger than the measured performance. An explanation could be the shaping of the tip, which is slightly approximated in the CFD modeling.

Comparison with other methods requires inflow angle and lift values. They are related, and uncertainties in the measured inflow angle must be accepted. The same inflow angles are also

used to calculate the CFD lift coefficients. Figure 6-15 compares the CFD results, RFOIL and FLUENT, with the experimental data in.
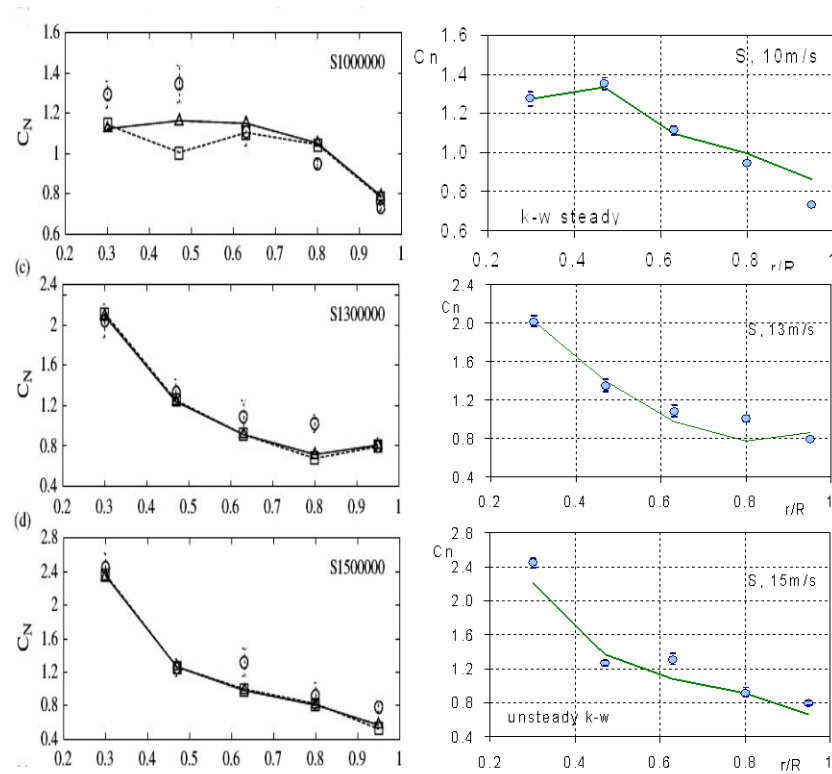
Figure 6-13. Spanwise distribution of C_n for three tunnel speeds for EllipSys3D (left) and FLUENT. Circles are measurements and the solid line represents CFD results.
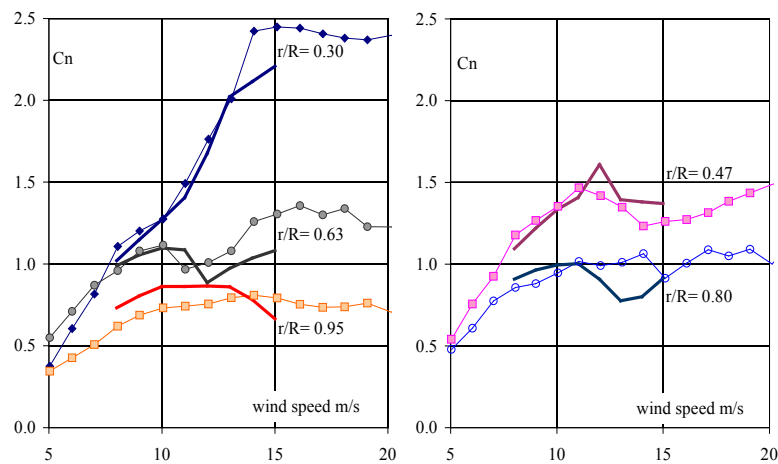
Figure 6-14. The normal force coefficients from the experiment and the full CFD results (full curves are k-ω SST model)
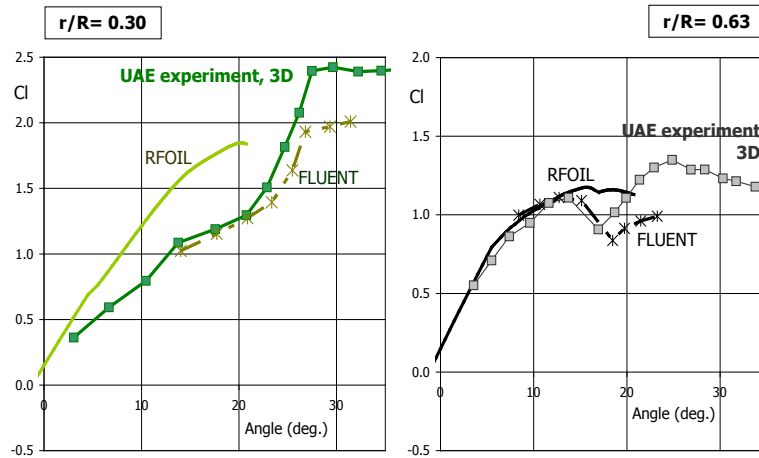
Figure 6-15. Comparison of two CFD results with the measurements

As already demonstrated in Figure 6-14, the approximations of the lift with FLUENT at the r/R=0.30 segment are very good and much better than with RFOIL, and FLUENT modeling of the inboard transition piece seems to be very important. Still, the maximum lift prediction is some 20% off. At the 63% span location, the differences are small and both CFD results seem to be quite good. The predictions of both codes at the segments r/R= 0.47 and r/R= 0.80 are comparable with UAE measurements.

6.4.2 Engineering versus CFD Conclusions and Future Work

The comparisons of the rotational flow characteristics for the NREL Phase VI rotor blade having the S809 airfoil show the following:

- Approximations of lift or normal force coefficient with engineering methods are far from satisfactory. Tuning the function constants could improve the result, but then the result would depend on the applied case.

- The results of the CFD methods RFOIL and FLUENT (or EllipSys3D) are in general quite good and have to be preferred. The panel code RFOIL is fast, but at the inboard and tip sections the influence of the transition piece or tip shape could cause large deviations. Full CFD codes do not have this drawback.

6.5 Conclusions and Future Work in All Three Areas

Taking rotor measurements in a wind tunnel reduces uncertainties at the rotor plane to almost negligible values and is a huge improvement over field measurements. This UAE produced a large, good-quality database. Like other experiments, however, some uncertainties still exist and measurement devices are often the cause. This cannot be neglected, and investigations showed that these influences are quite small and the given suggestions secure reliable segment characteristics. Most fluctuations in the flow around the blade are caused by the inevitable

dynamic of the experiment, and defining stationary flow is then by definition impossible. The smallest variation in the segment characteristics was in the first quarter of the rotor plane, and this part should be used as reference for stationary flow. This counts only for the nonyawed flow.

Most of the University of Delft investigations focused on determining proper rotational segment characteristics, in particular for the stationary flow, and determining the correct inflow angle is of vital importance. A new method derived the inflow angle and it is a unique option in the yawed flow. Local characteristics can be predicted with engineering methods or more advanced aerodynamic codes. Including other rotor geometries such as the NREL field experiments resolved that classical engineering methods are not well suited to predict the segment performances. The best (and easiest) alternative seems to be the RFOIL code. Additional validation is needed, especially for other airfoil profiles and wind tunnel experiments.

Future research must include other wind tunnel experiments like the one carried out by FOI (CARDC tunnel, China) and the MEXICO partners (DNW tunnel, Netherlands). The focus on stationary segment characteristics is needed as a base, but the unsteady characteristics will become more important. A more elaborate study of the many yawed cases in the UAE serves perfectly for these investigations. The huge UAE database contains more interesting measurements with respect to unsteady flow like several fast pitching campaigns. Only a small part is studied so far, and this is true for all partners involved in the Annex XX. Many opportunities to research rotor flow properties from the database exist, and we have a long way to go before we can properly quantify the loads on the wind turbine rotor.

6.6 Bibliography

Meng, F.; van Rooij, R.P.J.O.M. (2007). "CFD Investigations with Respect to Model Sensitivity for the Non-rotating Flow around the NREL Phase VI Blade." *Proceedings of the 2007 European Wind Energy Conference and Exhibition, 2007 European Wind Energy Conference and Exhibition in Milan, May 7–10, 2007*. Brussels: EWEA.
Sant T. (January 2007). "Improving BEM-based Aerodynamic Models in Wind Turbine Design Codes." ISBN: 978-99932-0-483-1. Ph.D. Thesis, Delft University of Technology, 451 pp.

Sant, T.; van Kuik, G.A.M.; van Bussel, G.J.W. (2006). "Estimating the Angle of Attack from Blade Pressure Measurements on the NREL Phase VI Rotor using a Free-Wake Vortex Model: Axial Conditions." *Wind Energy* (9:6); pp. 549–577.

van Kuik, G.A.M.; van Rooij, R.P.J.O.M.; Imamura, H. (2004). "Analysis of the UAE Phase VI Wind Tunnel Results in the Non-yawed Flow." *Proceedings of the 2004 European Wind Energy Conference and Exhibition, 2004 European Wind Energy Conference and Exhibition in London, November 22–25, 2004*. Brussels: EWEA.

van Rooij, R.P.J.O.M. (2004). "The Effect of the Test Set-up on the Segment Performance." Pages 125–139 in *Proceedings of the 2004 Joint Meeting of IEA R&D Wind Annex XI: Joint*

Action on the Aerodynamics of Wind Turbines and IEA R&D Wind Annex XX: HAWT Aerodynamics and Models from Wind Tunnel Measurements, June 17, 2004.

Rooij, R.P.J.O.M. van. (2005). "The effect of the test set-up on the steady state data." *Proceedings of the 2005 Joint Meeting of IEA R&D Wind Annex XI: Joint Action on the Aerodynamics of Wind Turbines and IEA R&D Wind Annex XX: HAWT Aerodynamics and Models from Wind Tunnel Measurements, Pamplona, Spain, May 25–26, 2005.* Golden, CO: NREL.

Rooij, R.P.J.O.M. van. (2007). "Engineering Models vs. CFD Methods with Respect to Augmented Lift Caused by Blade Rotation." *Proceedings of the 2007 Joint Meeting of IEA R&D Wind Annex XI: Joint Action on the Aerodynamics of Wind Turbines and IEA R&D Wind Annex XX: HAWT Aerodynamics and Models from Wind Tunnel Measurements, Roskilde, June 13–15, 2007.* Golden, CO: NREL.

Rooij R.P.J.O.M. van, Meng F.. (2008). "Analysis of the Flow Characteristics of Two Non-Rotating Rotor Blades." *Journal of Solar Energy Engineering, In Press.*

van Rooij, R.P.J.O.M.; Arens, E.A. (2007). "Analysis of the Experimental and Computational Flow Characteristics with Respect to the Augmented Lift Phenomenon Caused by Blade Rotation." *Journal of Physics, Conference Series, The Science of Making Torque from Wind, Lyngby, Denmark, August 28–31.*

van Rooij, R.P.J.O.M.; Meng, F.Z. (2006). "The steady state parked configuration." *Proceedings of the 2006 Joint Meeting of IEA R&D Wind Annex XI: Joint Action on the Aerodynamics of Wind Turbines and IEA R&D Wind Annex XX: HAWT Aerodynamics and Models from Wind Tunnel Measurements.* Golden, CO: NREL.

Rooij R.P.J.O.M. van, Meng F.. (2007). "Analysis of the Flow Characteristics of Several Non-Rotating Rotor Blades." *AIAA-2007-625, Proceedings from the 45th AIAA Aerospace Sciences Meeting and Exhibit, Reno, Nevada, January 8–11.*

van Rooij, R.P.J.O.M.; Schepers, J.G. (2005). "The Effect of Blade Geometry on Blade Stall Characteristics." *Journal of Solar Energy Engineering* (127); pp. 496–502.

Rooij, RPJOM van, J.G. Schepers. (2005). "The Effect of Blade Geometry on the Normal Force Distribution of a Rotating Blade." Pages 289–299 in *A Collection of the 2005 ASME Wind Energy Symposium. 2005 ASME Wind Energy Symposium at the 43rd AIAA Aerospace Sciences Meeting and Exhibit,* January 10–13. New York: ASME.

7.0 Research Summary—Norway

Organizations:	Institute for Energy Technology (IFE)
	Norwegian University of Science and Technology (NTNU)
Researchers:	Andreas Knauer, andreask@ife.no
	Geir Moe, geir.moe@ntnu.no

7.1 Background and Motivation

Norway, with its moderate level of wind energy development, has an official target of increasing annual wind energy production to 3 TWh by 2010. Furthermore, Scanwind AS and StatoilHydro have industrial initiatives. The strategic Norwegian wind energy program (2003–2007) was launched to support development through strengthening the nation's wind energy research competence. Rotor aerodynamics and aeroelastics are a vital part of the research, and Annex XX activities are the focus of international cooperation.

ENOVA SF financed the Norwegian participation in Annex XX. The Annex XX activities were initiated at the Institute for Energy Technology (IFE) (A. Knauer), and national research activities were conducted in cooperation with the Norwegian University of Science and Technology (NTNU) (G. Moe).

7.2 Data Used and Methods Employed

The research activities consisted of the UAE database exploitation and analysis (Annex XX focus area 2), model subcomponent construction/modification (focus area 3), and subcomponent integration and model validation (focus area 4). The main focus was investigating 3D-behavior of the flow and analyzing steady/unsteady behavior of flow patterns at different rotor sections.

IFE performed the basic research activities, focusing on 3D effects and stall phenomena on the rotor blades. To estimate stall onset and 3D effects, IFE developed a method using parts of the pressure distribution at the rotor blade (trailing edge pressure) combined with a Fourier transformation. The Unsteady Aerodynamics Experiment (UAE) experimental data were sampled with high frequency; this allowed using FFT on the results and transforming measured time series into the frequency plane. Spanwise stall onset was estimated for the turbine working in upwind conditions. The behavior of stall onset for yawed flow conditions was analyzed further. The FFT-based method allows the stall onset identification and gives a limited frequency spectrum induced by turbulent flow structures in different operational phases with distinctive maxima.

IFE also used the UAE test results to modify aeroelastic codes. A tower wake model was developed for the FLEX5 code. Using tower wake measures, IFE estimated tower wake shapes. In the ongoing activity, potential theory is used to model suitable wake shapes. The modified aeroelastic model is used to investigate floating offshore wind turbine concepts.

7.3 Research Results

At NTNU, Moe and two Ph.D. candidates analyzed data from the Ames wind tunnel tests for consistency. The work appears in EWEA 2007 conference papers and in a paper to appear in the journal *Wind Energy* (see Bibliography). The group is still working with the NREL UAE Phase VI database and writing two conference papers.

Further activities at NTNU investigated different stall delay models. The stall models were incorporated in the prescribed wake model HAWTDAWG, which comprises a more detailed rotor wake modeling than conventional Blade Element Momentum (BEM) methods. Comparing simulation results with UAE test data, the researchers identified variations in the prediction of power and thrust of the turbine for the stalled operation of the rotor at higher wind speeds. They concluded that, e.g., a combination of different stall delay models for distinct ranges of the angle of attack may give better results.

7.4 Conclusions and Future Work

Annex XX participation effectively supported Norwegian research efforts in rotor aerodynamics and aeroelastics . The UAE test database contains valuable information for testing, validating, and modifying various aerodynamic and aeroelastic models and will be used further.

The well-organized Annex meetings contributed further to effective scientific information exchange and good discussions in rotor aerodynamics and aeroelastic wind turbine modeling. The main result of the Norwegian participation in Annex XX was the strengthened competence in rotor aerodynamics and aeroelastic modeling. These scientific areas have an important role in the ongoing national development of new offshore wind turbine concepts. Such concepts may consist of different design solutions where especially aeroelastic modeling is a key issue, and Annex XX research results and the knowledge gained are of great value.

7.5 Bibliography

Breton, S. P.; Coton, F.N.; Moe, G. (2007). "A Study on Different Stall Delay Models Using a Prescribed Wake Vortex Scheme and NREL Phase VI Experiment." *Proceedings of EWEC 2007, Milan, Italy.*

Breton, S. P., Coton, F.N, Moe, G.. "A Study on Rotational Effects and Different Stall Delay Models Using a Prescribed Wake Vortex Scheme and NREL Phase VI Experiment." *Wind Energy*. In press.

Knauer, A. (2003). "Wind Energy in Norway." *Proceedings of IEA Annex XX Meeting 2003, Boulder, Colorado.*

Knauer, A. (2004a). "Aeroelastiske simuleringer/Aero-Elastic Simulations." Presented at the Norwegian Wind Seminar, Trondheim, Norway.

Knauer, A. (2004b). "Rotorblade Stall Investigations." *Proceedings of IEA Annex XX Meeting 2004, Montreal, Canada.*

Knauer, A. (2005). "Tip Design Issues." *Proceedings of IEA Annex XX Meeting 2005, Pamplona, Spain.*

Knauer, A. (2007). "Initial Investigations of Offshore Wind Turbine Concept." *Proceedings of IEA Annex XX Meeting 2007, Risø, Denmark.*

Knauer, A., Hanson, T.D. (2007a). "Undersøkelse av en ny drifttsstrategi for vindturbiner / Analysis of a New Operation Strategy for Wind Turbines." Presented at the Norwegian Wind Seminar, Trondheim, Norway.

Knauer, A.; Hanson, T.D.. (2007b). "High Speed Operation of Wind Turbines." *Proceedings of EWEC 2007, Milan, Italy.*

Knauer, A.; Hanson, T.D.; Skaare, B. (2006). "Offshore Wind Turbine Loads in Deep Water Environment." *Proceedings of EWEC 2006, Athens, Greece.*

Moe, G.; Breton, S.-B.; Long, H.; Schreck, S. (2007). "Assessment of Motions and Forces in the NREL NASA Ames Wind Tunnel Tests." *Proceedings of EWEC 2007, Milan, Italy.*

8.0 Research Summary—Spain

Organization: National Renewable Energy Centre (CENER)
Researchers: Xabier Munduate, xmunduate@cener.com
              Alvaro González, agonzalez@cener.com
              Esteban Ferrer, eferrer@cener.com
              Sugoi Gomez, Sugoi.Gomez-Iradi@liverpool.ac.uk
              George Barakos, G.Barakos@liverpool.ac.uk

8.1 Background and Motivation

CENER, the National Renewable Energy Centre of Spain, started its wind energy activities in 2002, at the same time as the onset of the International Energy Agency (IEA) Wind Annex XX. This project represented a unique opportunity for developing and improving knowledge on wind turbine aerodynamics. In the ensuing years, researchers have overcome limitations on engineering modeling and acquired physical understanding of complex flow phenomena.
At CENER, this work focused on acquiring reliable knowledge about aerodynamic effects in horizontal axis wind turbines (HAWTs) and understanding the physical phenomena involved. In addition, in 2005, computational fluid dynamics activities began at CENER, focusing on wind turbine airfoil analysis and on 3D blade simulations using full Navier-Stokes solvers (Fluent and recently CENER's in-house CFD code). The National Renewable Energy Laboratory (NREL) Phase VI data have been valuable for validating CFD codes and developing methods.

CENER's work related to Annex XX has focused on the following issues:
- Analyzing 3D stall delay for rotating blades: To obtain a better physical understanding.
- Predicting dynamic stall on parked blades: To gain a better physical understanding of the onset and three-dimensionality of the process and to asses Beddoes-Leishman model for the prediction of wind turbine dynamic stall.
- Validating the Navier-Stokes tools for rotating blades: The NREL phase VI data set has been used to validate the commercial and the in-house Navier-Stokes solvers and to create new methods for using CFD techniques at CENER.

8.2 Data Used and Methods Employed

The experimental analysis of data used sequences H (yaw = 0 all velocities), S (yaw = 0 all velocities), L (v = 20 m/s, pitch step 5°), and O of the NREL Unsteady Aerodynamics Experiment (UAE) Phase VI database, in addition to the steady data for the S809 airfoil from the Ohio State University, Colorado State University, and Delft Uuniversity of Technology wind tunnels. The dynamic stall investigation used unsteady oscillating tests of the S809 airfoil on the OSU wind tunnel.

CENER researchers compared CFD simulations of parked and rotating rotors to the NREL Phase VI wind turbine data. The parked cases used sequence L at a wind speed of 20 m/s and at various pitch angles. The rotating cases used sequences S and H in a nonyawed configuration and were compared for various wind speeds: 5, 7, 10, 13, 15, 20 and 25 m/s.

8.3 Experimental Analysis

To investigate the rotational effects, researchers analyzed the differences on the aerodynamic response between the S809 airfoil and the parked blade, and later performed the same comparison between the parked blade and the rotating blade. This method was employed to understand and separate the effects related to the 3D geometry of those related to the rotation. The NREL data are extensive, and Matlab was used to extract the data to useful figures or graphics suitable for the study. The c_p and pressure data were carefully analyzed, and a PSD frequency study analyzed the parked and rotating blade behavior. Force and moment coefficients in blade sections were also revised. The c_p data were used to characterize flow separation and reattachment for the rotating and parked blade, and researchers compared the flow topology.

For the dynamic stall study, the researchers used a similar procedure. Figures and graphics were extracted using data files containing information of unsteady oscillation cases of the S809 airfoil and the NREL parked blade sections. The force and moment coefficients for the unsteady cases were compared between the airfoil and the parked blade sections to understand the difference of the dynamic stall behavior related to the 3D geometry. In addition, the unsteady cases were compared with the steady data to establish the relation between them. But supporting the conclusions of the previous analysis required implementing the Beddoes-Leishman model and carrying out dynamic stall computations of the airfoil and 3D parked blade sections.

8.4 CFD Computations

Finally, for the CFD work, Fluent 6.2 was used to compute blade loads and c_p distributions on the NREL phase VI blade. To create the grids, Gambit (Fluent's mesher) was used. Nonstructured grids were created using tetrahedral and prismatic elements containing approximately 3 million elements. Simulations used the Moving Reference Frame (MRF) capability of Fluent. Modeling flow periodicity required modeling only one blade and using periodic boundary conditions. The NREL phase VI validation case (two-bladed rotor) used a 180° sector. Second-order discretization schemes were used for all variables and the SIMPLE algorithm selected to solve the pressure-velocity coupling. Even though the resolution of the boundary layer (and viscous sublayer) is always recommended, reasonable results have been obtained when using wall functions in conjunction with the k-ω Shear-Stress Transport (SST) model for attached flow conditions. The results are fully turbulent converged steady-state runs using the k-ω SST model. All simulations were run at CENER's cluster (36 computers exclusively for CFD use) using Fluent parallel capability in not fewer than four machines. Simulations with CENER's in-house CFD solver together with grids were generated using ICEM-CFD Hexa with genuinely multiblock grids. The number of available processors for parallel execution mainly dictates the number of blocks. A typical calculation involves about 250 blocks per blade computed on 16–128 processors according to the employed grid density. The current topologies combine an H-type structure away from the blades with a C-type structure attached to them. The compressible unsteady Navier-Stokes equations are discretized on a curvilinear multiblock body conforming mesh using a cell-centered finite

volume method. The convective terms are discretized using Osher's upwind scheme. MUSCL variable extrapolation confers second-order accuracy with the Van Albada limiter. A central discretization method is used for the viscous terms. The solver includes a variety of linear and nonlinear eddy-viscosity models, though for this work the standard k- ω model of Wilcox has been used. Menter's SST version of the k- ω model [3] was also employed for some of the cases. A dual-time stepping method is employed for time-accurate simulations, where a second-order backward difference approximated the time derivative. Integrating in pseudo-time using a first-order backward difference solves the resulting nonlinear system of equations .

8.5 Research Results

First, the work on rotational effects generated many figures showing mainly c_p and C_n related to the aerodynamic behavior of the S809 airfoil and the NREL parked and rotating blade. Analyzing and comparing the figures extracted some results about the 3D geometry and rotational effects on the aerodynamic behavior. The importance of rotation and 3D geometry on the aerodynamic behavior of the NREL blade has been clearly revealed, changing the flow topology over the blade and consequently changing the aerodynamic loads. For the parked blade, separation in one blade location may affect the flow details in the nearest locations, such as the formation of a leading edge separation at sections close to the blade root. This leading edge separation might be related to the trailing edge separation delay process and responsible of a smoothed and delayed stall. C_n values are not amplified as a result of the leading edge separation. But for the rotating blade, researchers observed leading edge separation at inner span stations with total suppression of trailing edge separation. Within this separated region, a strong radial flow forced by rotation is generated, connected with the extra lift observed for the rotating blade. The new flow topology for inboard stations is reminiscent of a leading edge vortex-like structure that does not convect into the free stream remaining attached to the surface. Figure 8-1 shows, for the parked and rotating blade, an example of the extracted separation and impingement points of the flow for the 30% blade span station when incidence is increasing. The figure shows the change in flow topology.

The work on the dynamic stall phenomenon analyzed the aerodynamic behavior of the S809 airfoil and different parked blade sections undergoing the same unsteady oscillating tests. The comparison between the unsteady airfoil behavior and the steady data showed the existence of a relationship between the dynamic stall behavior and the steady data for a 2D airfoil. The same comparison for the parked blade, using the unsteady and steady data of the blade span stations, showed that the dynamic stall behavior of a 3D parked blade seems to be managed by the steady behavior of the different sections just as the steady behavior of the profile manages the dynamic stall behavior of a 2D aerofoil.. After the experimental analysis, researchers implemented a Beddoes-Leishman model and the computations confirmed the previous conclusions. Figure 8-2 shows an example of computation with the Beddoes-Leishman model compared with the experimental data. The case selected is a sinusoidal oscillation of the angle of attack for the 30% blade span station, with reduced frequency 0.075, mean angle 20º, and amplitude of oscillation 10º. The figure shows the C_l response versus the angle of attack for the experimental data and for two computations of the Beddoes-Leishman model with different input data. One computation is performed with the
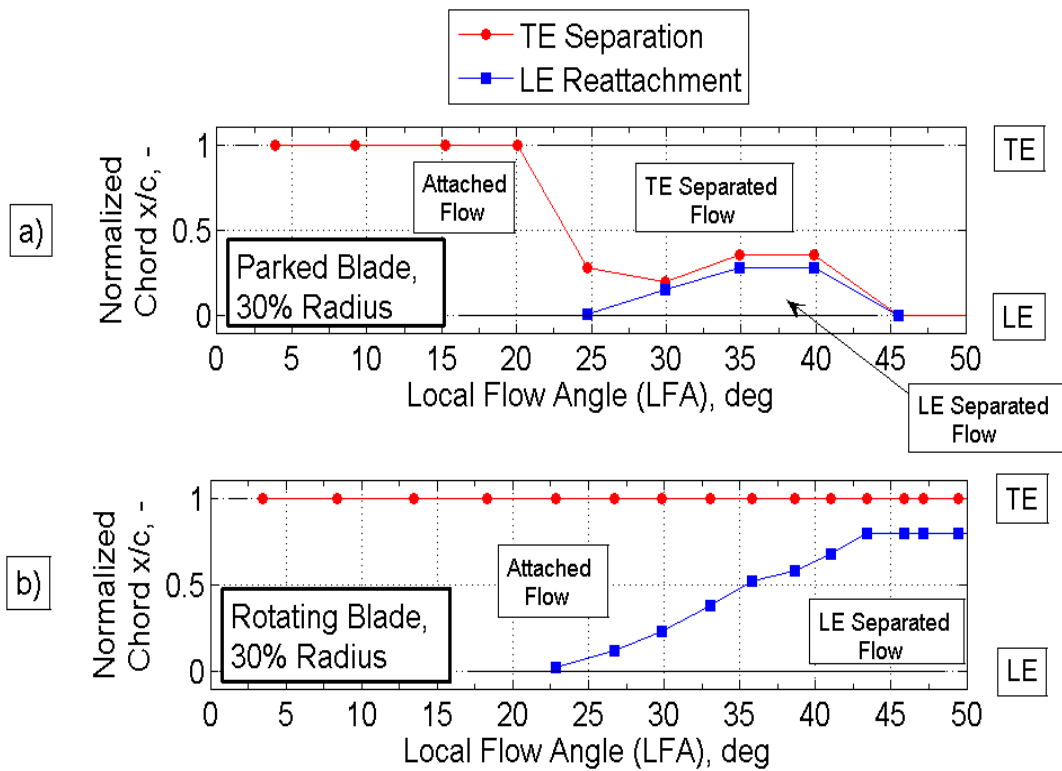
Figure 8-1. Trailing edge separation and leading edge reattachment points on the parked (a) and rotating (b) blade 30% span station
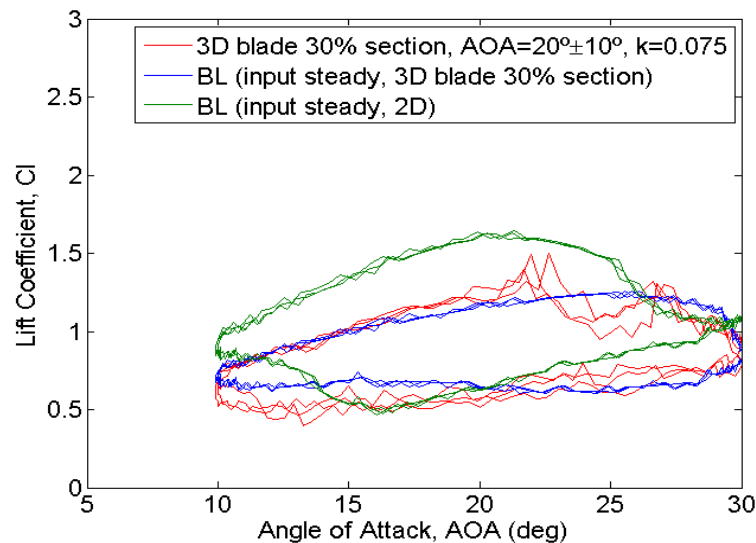
Figure 8-2. Unsteady oscillation for the 30% blade section, comparison between experimental data (red line), Beddoes-Leishman computation with the 2D steady data (green line), and computation with the 3D blade section steady data (blue line)

2D airfoil steady data, and the agreement with the experimental data is not very good. The other computation used the steady data of the 30% span station, and agreement with the experimental data is quite good.

Finally, the CFD results with Fluent (Figure 8-3a, top) and CENER's in-house solver (Figure 8-3b) showed that for low wind speeds (7 m/s) corresponding to moderated local flow angles, the flow can be well predicted. The depicted results correspond to the S sequence with a free stream velocity of 7 m/s and a rotational speed of 71.9 rpm. These figures show the c_p comparison between CFD and experimental data for the 47% radial station. The compared c_p values were calculated using the sectional stagnation pressure. The computations predict quite accurately the experimental c_p values at these locations.

Figure 8-3 top and bottom shows the comparison of the normal force coefficient along the blade. Discrepancies in the 30% and 95% station are thought to be related to the modeled geometry (e.g., tip not properly modeled, root-blade transition). Reasonable agreement is found for the intermediate stations. The results Figure 2 top show that the k-ω SST model, combined with wall functions and Fluent's MRF capability, gives reasonable results for rotating blades as long as the flow remains attached. For higher wind speeds, when separated flow arises on the suction side of the blade, simulations are not as accurate when predicting the pressure distributions. These inaccuracies seem to be related to the mesh density, the turbulence modeling, and the transient nature of the flow.

Figure 1 - Pressure distribution for 47% radial location for the NREL phase VI blade	Figure 2 - Normal force coefficient vs r/R for the NREL phase VI blade
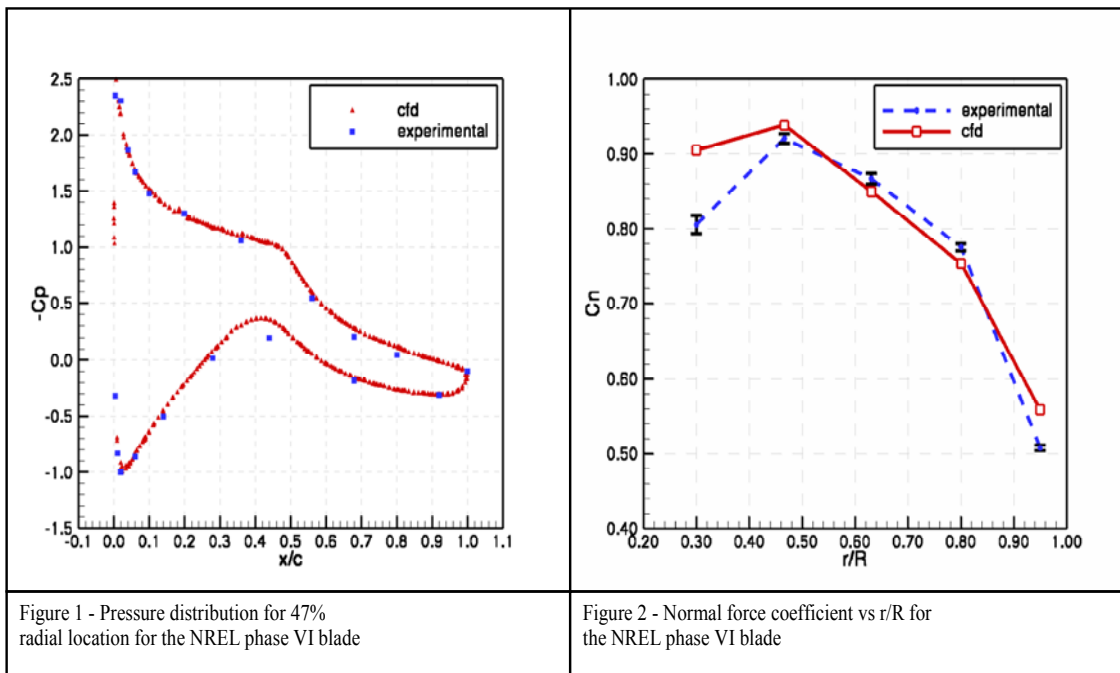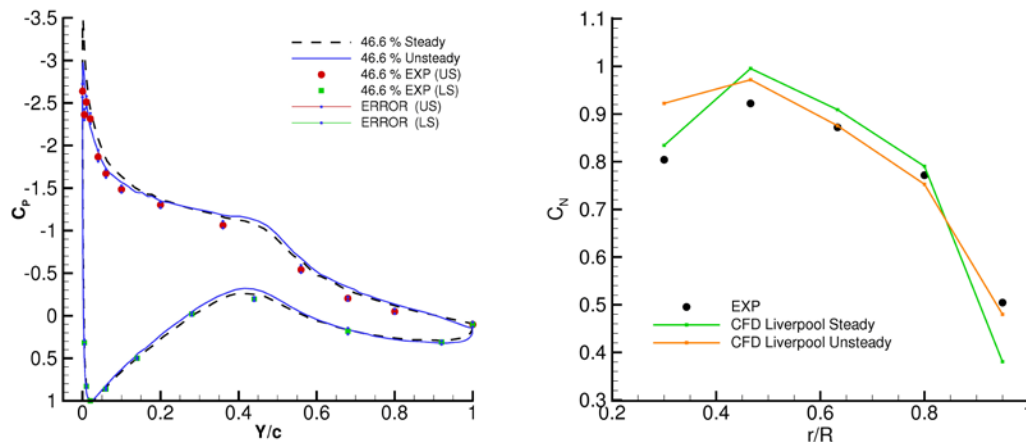
Figure 8-3. Surface pressure and normal force coefficient distributions, comparing data from experiment with data from CFD models.

8.6 Conclusions and Future Work

In general, the coarse spanwise instrumented locations measured over the blade experiment is not densely arrayed enough for the 3D analysis, mainly in the radial direction. In addition, data are acquired only at the blade surface, and therefore it has not been possible to analyze the flow behavior above the blade surface. Future flow visualizations might help researchers understand the complete flow topology.

The rotation study analyzed c_p and C_n using mainly mean values. The flow behavior for rotating blades, however, was extremely unsteady and complex. Therefore, further examination of the instantaneous measurements might offer more insight into the phenomena.

The study of the dynamic stall on the NREL 3D parked blade sections reached one of the most important practical conclusions, related to the possibility of modeling the dynamic stall behavior of a 3D parked blade through a 2D modeling, and considering appropriate inputs related with the steady data of the blade sections. Analyzing dynamic stall for a 3D parked blade and the knowledge acquired could improve dynamic stall modeling on real 3D parked blade applications. Future work should investigate 3D rotating blade dynamic stall and develop improved modeling tools.

Finally, the Annex XX allowed CENER to produce the necessary methods and capabilities to compute rotor simulations using CFD. Analyzing CFD results and comparing them to experimental data helped CENER engineers understand complex flow phenomena on a rotating blade. CENER's in-house CFD code is currently being validated and compared to experimental data and Fluent results. Future work will investigate 3D rotational effect and spanwise flow components.

8.7 Bibliography

Cabezón, D.; Ferrer, E. (2005). "Modelling Wake Effects Using Two CFD Techniques." EUROMECH Colloquium 464b: Wind Energy, October 04-07, Oldenburg, Germany.

Ferrer, E.; Munduate, X. (2005). "CFD Activities at CENER." IEA Annex XX Symposium, Pamplona, Spain, May 2005.

Ferrer, E.; Munduate, X. (2006). "Preliminary CFD Simulations of the NREL Phase VI Rotating Blade." EWEC 2006.

Ferrer, E.; Munduate, X. (2007). "Wind Turbine Blade Tip Comparison Using CFD." *J. Phys.: Conf. Ser.* 75, 012005 - 10 pp.

Gomez-Iradi, S.; Barakos, G.N.; Munduate, X. (2007). "Development of a CFD Method for Aerodynamic Analysis of Large Diameter Horizontal Axis Wind Turbines." IEA Annex XX, June 2007, Risoe, Denmark.

Gonzalez, A.; Munduate, X. (2006). "Flow Development on the NREL UAE Phase VI Rotating Blade." IEA Annex XX, Kiel, Germany.

Gonzalez, A.; Munduate, X. (2007). "Three-Dimensional and Rotational Aerodynamics on the NREL Phase VI Wind Turbine Blade." 45th AIAA Aerospace Sciences Meeting and Exhibit, Reno, NV, EEUU.

Gonzalez, A.; Munduate, X. (2007). "Experimental Analysis of Dynamic Stall on the NREL Phase VI Parked Blade." IEA Annex XX, Risoe, Roskilde, Denmark.

Munduate, X. (2003). "Research Summary IEA Annex XX HAWT Aerodynamics and Models from Wind Tunnel Measurements." IEA Annex XX. Golden, CO: EEUU.

Munduate, X.; Gonzalez, A. (2004). "Aerodynamic Analysis from Three Dimensional Wind Turbine Blade Measurements at Zero Yaw Angle." IEA Annex XX, Montreal, Quebec, Canada.

Munduate, X.; Gonzalez, A. (2005). "3D Blade Geometry Stall at Parked and Rotating Conditions on the NREL Phase VI at Zero Yaw Angle." IEA Annex XX, Pamplona, Navarra, Spain.

9.0 Research Summary—Sweden

Organizations: Gotland University and the Royal Institute of Technology

Researcher: Stefan Ivanell, stefan.ivanell@hgo.se

9.1 Background and Motivation

Knowledge about wind power technology has increased over the years. Lanchester and Betz were the first to predict the maximum power output of an ideal wind turbine. The major breakthrough was achieved by Glauert, who formulated the Blade Element Momentum (BEM) method in 1935.
The BEM method still underlies today's design codes. It has, however, been extended to allow for dynamic events with patchwork and ad hoc engineering methods, sometimes of doubtful quality.

Therefore, aerodynamic research today is shifting toward a more fundamental approach because the basic aerodynamic mechanisms are not fully understood and the importance of accurate design models increases when turbines are larger. Recently completed Navier-Stokes calculations and supercomputers open new possibilities.

Annex XX has focused on evaluating existing aerodynamic simulation methods to allow simulations that give results that would make it possible to evaluate the flow field behind the turbine, i.e., the wake. These simulations support the study of the physical behavior of the wake. The work can be divided into three groups:

1. **Simulation Method.** The first aim was to find a suitable method to simulate the flow field around the turbine and also resolve the wake so that it would be possible to evaluate the flow field behind the turbine. Particular attention was given to the circulation directly behind the blades to give a better understanding of the physics close there.

2. **Stability Analysis.** The second aim was to understand the basic mechanisms underlying the breakdown of the flow structure in the wake. This becomes especially important when looking at interactions between two or more wakes. Optimizing the number of turbines and their positions in parks requires knowledge about the length of the wake behind the turbines. Therefore knowledge about the basic mechanisms underlying the breakdown of the distinct tip vortex is important.

3. **Park Simulation.** The overall aim is to be able to simulate an entire park. A suitable method, limitations in that method, basic mechanisms behind breakdown of the flow structure, and so on is, however, necessary knowledge before setting up an advanced simulation model for a park. When that is achieved and a simulation model for an entire park exists, researchers can study how to optimize not only one or two turbines but also clusters of many turbines. This opens possibilities to studying how changing the local energy extraction, turbine spacing, yaw angle, and park design affect total park efficiency. The results of interaction between the wakes will also be important from a fatigue load point of view.

9.2 Data Used and Methods Employed

All Actuator Line Method (ACL) simulations used data from the Tjaereborg turbine. The Tjaereborg turbine was operational between 1988 and 1998, when researchers made extensive measurements and tests on the turbine. The turbine was 9 km southeast of the city of Esbjerg in western Denmark. Tjaereborg was a three-blade, upwind horizontal axis turbine. The blade profiles were NACA 4412-43 with a blade length of 29 m giving a rotor diameter of 61 m. The chord length was 0.9 m at the tip, increasing linearly to 3.3 m at hub radius 6 m. The blades are twisted 1± per 3 m. The tip speed was 70.7 m/s and the rotor solidity was 5.9%. The rated power was 2 MW, and a continuously variable pitch operating between 0° and 35° degree in production mode controlled the output. The hub height is 60 m.

Researchers used the EllipSys3D code for all simulations. EllipSys3D is a general purpose, three-dimensional (3D) solver developed by N.N. Sørensen and J. Michelsen. The blades are represented by volume forces. The ACL method, introduced by Sørensen and Shen was used. The limitation in the actuator-disk method, where the influence of the blades is taken as an integrated quantity in the azimuthal direction, has now been overcome using techniques in which volume forces are distributed along lines representing each blade. A full CFD simulation would require a great number of nodes at the blades to resolve the boundary layer. With this method, node points could be saved at the blades. This method therefore opens new possibilities for turbine simulations with a well-resolved wake. But the drawback is that the method still is based on tabulated data from which C_L and C_D are functions of alpha; therefore, they depend on the quality of these experimental data. R. Mikkelsen implemented this method with the EllipSys3D code.

9.3 Research Results

The simulations resulted in flow fields corresponding to expected flow according to experiments and experience. Verifications of the results by comparison with measurements data have, however, not been performed in this project. Recent data are, however, available from wake measurements from the MEXICO (Model Rotor Experiments In Controlled Conditions)project. When the work was performed, no model scale wake data were available to verify the simulated results against.. The result, however, was as expected, and Helmholtz' law is valid in the wake flow (Ivanell et al. 2005).

The conclusion can therefore be made that CFD simulations using volume force approaches can simulate complicated wake flow. The importance of the possibility of performing relatively fast studies will increase with the challenge of accurate calculations of the performance and the fatigue load of tomorrow's large-scale wind turbine parks. The work can also be used for further studies of basic flow features in the wake. The simulated flow fields could also be used as initial conditions for stability studies or as inlet in other studies of features such as fatigue loads. Also, Ivanell and others (2006) carried out an initial numerical stability study of the tip vortex.

9.4 Conclusions and Future Work

This study examined detailed wake flow using the ACL technique, but less time-consuming methods such as ACD (actuator disk) methods could also be used to simulate larger turbine parks because the ACD method is based on the same idea of representing the blades by volume forces that correspond to the energy extraction.
The initial stability study summarized herein gives background knowledge to the full numerical stability study of the tip vortex.
After a stability study, full park simulations could be performed using the actuator-disk methods. Future work will therefore concentrate on further stability investigations and later on full park simulations.

9.5 Bibliography

Ivanell, S. (2005). Numerical Computations of Wind Turbine Wakes. Licentiate thesis, ISSN 0348-467X, KTH.
Ivanell, S.; Sørensen, J.N.; Mikkelsen, R.; Henningson, D. (2006). "Numerical Analysis of the Tip and Root Vortex Position in the Wake of a Wind Turbine." *Journal of Physics*, Conference Series Volume 75, Springer.

10.0 Research Summary—United States

Organizations: NREL's National Wind Technology Center (NWTC)

Researcher: Scott Schreck, scott_schreck@nrel.gov

10.1 Background and Motivation

Horizontal axis wind turbines (HAWTs) routinely experience unanticipated aerodynamic loads. Elevated aerodynamic loads impose high stresses on blades and structural components, appreciably shortening machine service life. In addition, aerodynamic load fluctuations produce torque variations that adversely impact power quality and degrade transmissions. These and other factors arising from unpredicted and excessive aerodynamic loading drive up the overall cost of energy. Failure to reliably predict aerodynamic loads derives from the complex nature of wind turbine blade aerodynamics and incomplete comprehension of the fluid dynamics that govern them. Flow fields elicited by HAWT blades are highly complex because of the simultaneous presence and interaction of three-dimensionality, unsteadiness, separation, and rotational influences. At zero yaw, rotational augmentation is the main increment to blade aerodynamics.

Using Unsteady Aerodynamics Experiment (UAE) data acquired in during the NASA Ames wind tunnel test, early analyses concluded that rotational augmentation was associated with distinctive chordwise and spanwise pressure signatures that varied in an orderly manner in response to changes in radial location and inflow conditions (Schreck and Robinson 2002). Subsequent work exploited rotating blade surface pressure data to characterize boundary layer separation and shear layer impingement, and flow field structure evolution with rotational augmentation of the flow field (Schreck and Robinson 2003a).

Closely related research correlated experimentally and computationally derived surface flow topologies for the rotating blade, finding excellent agreement and significantly generalizing comprehension of the flow field (Schreck and Robinson 2003b; Schreck, Sørensen, and Robinson 2007). Other work isolated tip speed ratio as an independent variable, and quantified the influence of tip speed ratio on aerodynamic forces and underlying flow field structure (Schreck and Robinson 2004).

Prior to the inception of Annex XX, analyses of UAE data had isolated several of the main flow field structures and processes principally responsible for the most prominent steady state aspects of rotational augmentation. The U.S. effort in connection with Annex XX thus concentrated on the time-varying components of rotational augmentation, which ultimately were found to be significant in magnitude and thus important to the field of wind turbine aerodynamics. In particular, these analyses were directed toward revealing relationships between the mean and unsteady components operating in the rotationally augmented blade flow field.

10.2 Data Used and Methods Employed

10.2.1 Rotating Blade Data

U.S. research in support of Annex XX used zero yaw data extracted from the H and S sequences. In these sequences, all data were collected with the turbine rotating at a constant speed of 71.6 RPM. For the zero yaw data, the turbine blade plane of rotation was maintained orthogonal to the test section centerline, yielding a yaw angle of 0°. Blade pitch angle was held constant at 3.0°. Test section velocity was varied between 5 and 25 m/s, in nominal increments of 1 m/s. At each test section velocity, a 30 second data record was acquired.

For sequence H, the five hole probes and stalks were mounted on the blade, and LFA was measured concurrently with other blade aerodynamic properties. For sequence S, the probes and stalks were removed and measurements were repeated using an otherwise identical machine configuration and virtually identical inflow conditions. This approach allowed accurate measurement of LFA while maintaining the blade flow field free of any possible intrusions caused by the stalks or probes.

10.2.2 Parked Blade Data

To isolate the effects of rotational influences, a baseline was established wherein these effects were excluded. This was accomplished by halting turbine blade rotation and acquiring pressure data for the stationary (parked) blade in sequence L. To achieve stationary blade conditions, the instrumented turbine blade was first fixed at the 12 o'clock azimuth position. Then, turbine blade pitch was incremented in 5° steps, from 90° to –15° and –15° to 90°. Blade pitch was incremented in both negative and positive directions to disclose any hysteresis in blade aerodynamic force response. This process was repeated twice, once at U_∞ = 20 m/s and once at U_∞ = 30 m/s.

Blade pitch angle was defined as the angle between the blade tip chord line and the blade rotation plane, and pitching that moved the leading edge upwind was defined as positive. One 13 second data record was acquired at each pitch angle. At each pitch angle, appropriate delays were included to allow time for pitching, blade flow field equilibration, and wake relaxation. Time records of c_p were integrated over the sectional chord to obtain time records of C_n. Finally, time records of c_p and C_n were time averaged to yield mean values for these quantities.

The 30 second time records of c_p from the H and S sequences were integrated over the sectional chord to obtain time records of C_n at r/R = 0.30, 0.47, 0.63, and 0.80. Data were available at 0.95R, but were not analyzed because of the potentially confounding influence of the blade tip vortex. At these radial locations, time records of c_p and C_n were processed to obtain means and standard deviations for c_p and C_n. To separate time variations caused by rotational flow physics from tower wake influences, only those data corresponding to the upper half of the rotor disk were extracted and analyzed.

Surface pressure coefficient (c_p) mean and standard deviation data were exploited to infer the blade flow field topology. Based on a large body of prior research, a surface pressure distribution exhibiting significant chordwise pressure gradient (dp/dx) was deemed to indicate attached flow and an attenuated pressure gradient was considered indicative of separated flow.

In addition, boundary layer separation and shear layer impingement elicit localized surface pressure fluctuations significantly greater than those observed at locations occupied by attached flow (Schreck and Robinson 2003a). To increase confidence in inferences of blade surface flow topology, and to generalize analyses above the blade surface, computations were used following validations involving UAE H and S sequence zero yaw data (Schreck, Sørensen, and Robinson 2007). These relationships were used to identify the locations and movements of boundary layer separation and shear layer impingement on the turbine blade suction surface.

10.3 Research Results

10.3.1 Flow Field Topology

Figure 10-1 shows standard deviation in C_n versus local inflow angle (LFA) for r/R = 0.30, 0.47, 0.63, and 0.80. At all four radial locations, C_n standard deviation exhibited values between 0.01 and 0.03 at low LFA. In the range $17.6° \leq LFA \leq 26.4°$, however, C_n standard deviation increased rapidly with LFA and reached maxima ranging from 0.16 to 0.21. In Figure 10-1, C_n standard deviation increased abruptly from low values characteristic of nonrotating blade levels to elevated values that substantially exceeded those observed on the nonrotating blade. Further, although the four radial locations were separated by significant distances, the abrupt C_n standard deviation increase occurred over a relatively constrained LFA range. This sudden, substantial shift in aerodynamic loading, confined to a narrow LFA range but enveloping most of the blade radius, implies a radical shift in the rotating blade flow field structure.

Figure 10-2 shows schematics of separating and impinging blade flow field topologies, determined in previous work (Schreck and Robinson 2003a; 2003b; Schreck, Sørensen, and Robinson 2007). The upper portion of Figure 10-2 depicts boundary layer separation, with the separation site represented by the filled circular symbol. Flow is attached upstream of the separation, and a streamline emanates from the separation site. The notation L_{SEP} shows the length of the
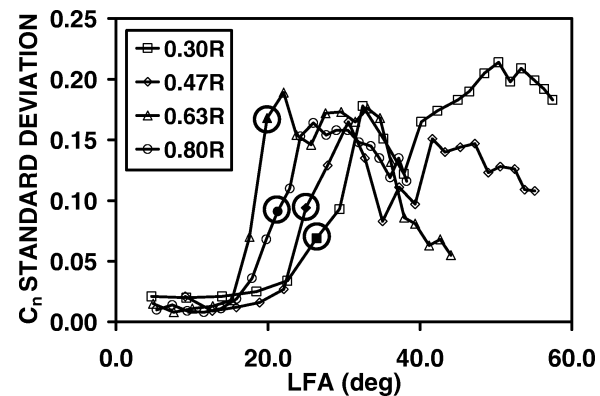

Figure 10-1. C_n standard deviation vs. LFA for rotating blade at r/R = 0.30, 0.47, 0.63, and 0.80
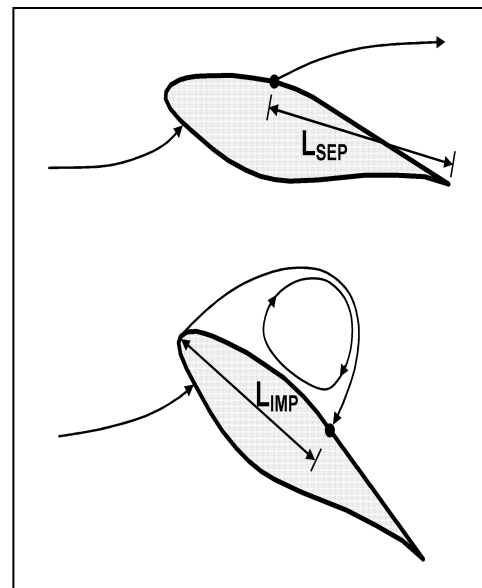

Figure 10-2. Mean flow field topologies for boundary layer separation (upper) and shear layer impingement (lower)

77

separated region. The boundary layer separation flow state occurs at moderate LFA levels, which are below or near LFA corresponding to two-dimensional stall.

The lower part of Figure 10-2 shows shear layer impingement, in which the boundary layer initially separates from the surface near the leading edge. Thereafter, the shear layer arches over the blade and impinges on the surface aft of the leading edge, indicated by the filled circular symbol. Presumably, appreciable concentrations of vorticity reside within the region enclosed by the shear layer, producing a circulating flow structure. The notation L_{IMP} shows the length of the region encompassed by impingement. The shear layer impingement flow state generally occurs at elevated LFA, at LFA levels that substantially exceed LFA corresponding to two-dimensional stall.

In Figure 10-1, the LFA at which the separation point reached the blade leading edge is indicated by the single filled symbol (circled for clarity) on each of the four plots. Notably, these four solid symbols are confined to a narrow LFA range of $19.9° \leq LFA \leq 26.4°$. Further, these data points are centered in the steeply rising portion of the C_n standard deviation curve. This implies that forward separation point movement was responsible for increasing C_n standard deviation. This also implies that the highest C_n standard deviation levels were produced by an impinging flow field structure.

10.3.2 Unsteady Load Magnitudes

The linkage between Figures 10-1 and 10-2 implies that a consistent relationship exists between C_n standard deviation levels and mean separation/impingement length. C_n standard deviation was thus correlated with separation length in Figure 10-3 and with impingement length in Figure 10-4. Figure 10-2 defines separation length (L_{SEP}) and impingement length (L_{IMP}).

In Figure 10-3, for $L_{SEP} = 0.0$ c (separation at trailing edge), C_n standard deviations for all four radial locations are grouped tightly around a value of approximately 0.02. As separation moved toward the leading edge and separation length increased, C_n standard deviation increased in steady, monotonic fashion for all four radial stations. The solid line extending diagonally across the lower part of the plot is an aggregate linear least squares fit to all plotted data points and thus represents an average correlation across all four radial locations. Slope of this linear fit is 0.100.

Clearly, data points corresponding to the four radial locations deviate from the linear fit. Irregular deviation from the linear fit can be partially attributed to comparatively coarse chordwise pressure tap resolution over the aft portion of the blade surface. Careful examination of Figure 10-3, however, reveals that the points for the 0.47R and 0.63R locations assume a consistently steeper slope than those for 0.30R and 0.80R. Thus, three-dimensional
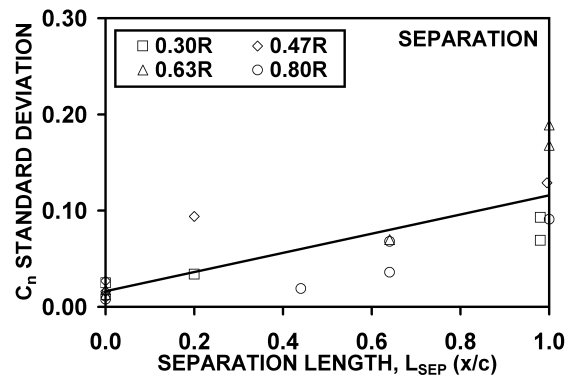

Figure 10-3. Correlation between C_n standard deviation and separation length (L_{SEP})

aerodynamic interactions also are a likely source for systematic deviations from the aggregate linear fit.

For separation lengths of 1.0, corresponding to the arrival of separation near the leading edge, C_n standard deviation levels averaged approximately 0.1. Previous buffet research using 2D airfoils reported similar maximum C_n standard deviation levels (Coe and Mellenthin 1954; Polentz, Page, and Levy 1955). These efforts did not measure separation location or extent. Stabilization of C_n standard deviation at elevated loading conditions, however, presumably indicated separation arrival in the leading edge vicinity.

In Figure 10-4, for $L_{IMP} = 0.0$ (impingement at leading edge) to 1.0 c (impingement at trailing edge), C_n standard deviation for all four radial locations was confined to a range of approximately 0.1 to 0.2. As before, a linear least squares fit was applied to all data points in the Figure 10-4 plot and is shown by the solid line extending across the center of the plot. The slope of this aggregate linear fit is 0.023, which is significantly shallower than the slope of 0.100 for the line fit to the separation length data in Figure 10-3.

As in Figure 10-3, data points in Figure 10-4 deviate visibly from the linear fit. Sporadic deviation from the linear fit is partially attributable to sparse chordwise pressure tap spacing over the aft blade chord. Strong aerodynamic three-dimensionality has, however, previously been identified in the UAE operating range corresponding to the Figure 10-4 data (Schreck, Sørensen, and Robinson

Figure 10-4. Correlation between C_n standard deviation and impingement length (L_{IMP}).

2007). This flow field change causes spanwise flow components that alter impingement length and modify the physics of unsteady aerodynamic force generation.
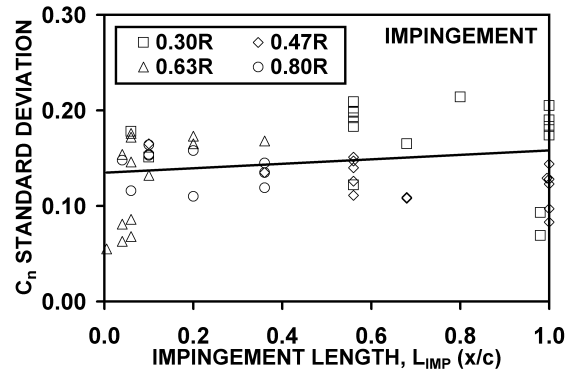
Comparing the aggregate linear least squares fit for separation (Figure 10-3) with that for impingement (Figure 10-4) leads to two clear observations. First, time-varying aerodynamic force levels are, with only isolated exceptions, significantly higher for an impinging flow field than for a separated flow field. Second, the slope of the linear fit for separation (0.100) is four times steeper than that for impingement (0.023). This indicates that above-surface fluid dynamics responsible for time-varying aerodynamic force production respond more actively to surface flow state during separation than during impingement.

10.3.3 Unsteady Load Severity
Thus far, the only C_n standard deviations considered have been those produced by interactions occurring spontaneously in separated and impinging blade flow fields. This exclusion was enabled by the NASA Ames 80 ft ×120 ft wind tunnel, which provided an inflow environment free of significant inflow turbulence or velocity gradients (Zell 1993). To quantify C_n standard deviations that would occur in response to turbulent atmospheric inflow, the UAE was

modeled using the YawDyn (Laino and Hansen 2003) and AeroDyn (Laino and Hansen 2002) models in conjunction with turbulent inflow files from TurbSim (Jonkman and Buhl, 2006).

Figures 10-5 and 10-6 show C_n standard deviation data from the UAE wind tunnel test along with C_n standard deviation data extracted from YawDyn/TurbSim model output files. "UAE Test Data" in these figures are the same as those in Figure 10-1, except that the test data in Figures 10-5 and 10-6 are plotted as a function of U_∞ to maintain consistency with the model data. For each radial location, C_n standard deviation data were extracted from model output files for three turbulence intensities (5%, 10%, and 15%) for each of five mean wind speeds (U_∞ = 5, 10, 15, 20, and 25 m/s).

Figure 10-5 shows C_n standard deviation test measurements and model predictions for the 0.30R radial location. The C_n standard deviation levels for the test data exhibit subdued levels for low U_∞ and increase steadily with U_∞. The three modeled turbulence intensity levels produce three widely separated C_n standard deviation levels, all of which are significant in magnitude. UAE test data points representing a separated flow field reach C_n standard deviation levels corresponding to turbulence intensities of 5 to 10 percent. Some UAE test data points for an impinging flow field lie between the 10 and 15 percent turbulence intensity curves, and several more reach C_n standard deviation levels exceeding those elicited by
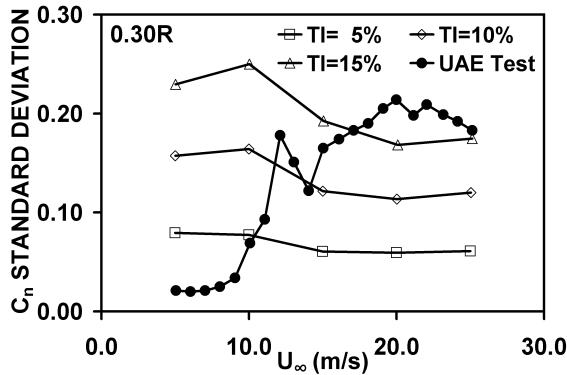

Figure 10-5. C_n standard deviations measured by UAE and predicted by YawDyn/TurbSim at 0.30R.
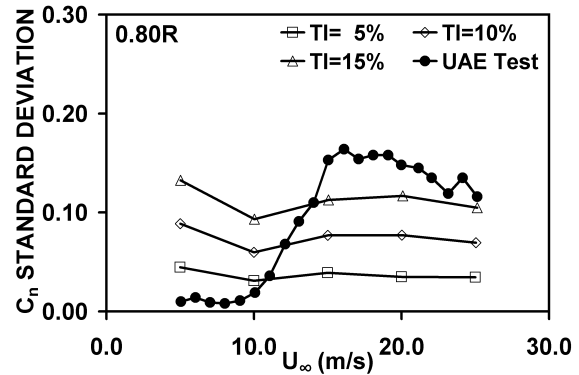

Figure 10-6. C_n standard deviations measured by UAE and predicted by YawDyn/TurbSim at 0.80R.

turbulence intensities of 15 percent.

Figure 10-6 shows C_n standard deviation test measurements and model predictions for the 0.80R radial location. As in Figure 10-5 for 0.30R, test data C_n standard deviation levels assume attenuated levels for low U_∞ and increase substantially with U_∞. The three modeled turbulence intensities of 5, 10, and 15 percent yield three clearly delineated C_n standard deviation levels. Although the magnitudes of these curves are lower than those at 0.30R, all three nonetheless remain significant in magnitude. UAE test data points for separated flow fields reach C_n standard deviation levels represented by turbulence intensities of 10 to 15 percent. All the UAE test data points representing impinging flow fields lie above the 15 percent turbulence intensity curve, with many of these points lying significantly above this curve.

Figures 10-5 and 10-6 clearly show that blade operation in either the stalled regime in stable, uniform inflow or in the unstalled regime in turbulent inflow produces C_n standard deviations of comparable and substantial magnitude. The turbulence intensity range of 5 to 15 percent in Figures 10-5 and 10-6 approximates the turbulence intensity range of 13 to 20 percent encompassed by various design standards (Burton et al. 2001). Similar data were analyzed for 0.47R and 0.63R, revealing trends consistent with those shown by Figures 10-5 and 10-6. It is important to note that these data and analyses are not intended to predict C_n standard deviation levels that could be expected for a blade operating in the stalled regime in a turbulent inflow.

10.4 Conclusions and Future Work

Blade surface pressure data were acquired from the NREL Unsteady Aerodynamics Experiment horizontal axis wind turbine tested under axisymmetric conditions in the NASA Ames 80 ft ×120 ft wind tunnel. Records of time-varying surface pressure and normal force were analyzed to extract mean separation and impingement location and normal force coefficient standard deviation during operating conditions that included rotational augmentation. Complementary model predictions of time-varying normal force coefficient standard deviation also were used for turbulent inflow conditions. These data and analyses support the following conclusions regarding unsteadiness associated with rotational augmentation.

Before the onset of rotational augmentation, boundary layer separation advances forward over the blade in response to increasing local flow angle. After separation arrival at the blade leading edge, shear layer impingement commences in the same vicinity. Subsequently, the impingement site advances aft on the blade chord in response to increasing local flow angle.

Forward movement of the separation point from the leading edge amplifies aerodynamic force standard deviations. Aerodynamic force standard deviations are most significantly amplified, however, as the separation point reaches the leading edge and the flow field transitions to an impinging flow field mediated by shear layer impingement.

Normal force coefficient standard deviation correlates well with mean flow field spatial scales at the blade surface, specifically mean separated length and mean impingement length.

Normal force coefficient standard deviation responds more sensitively to blade surface mean flow field state for separating flow fields than for impinging flow fields.

Normal force coefficient standard deviations observed for stable, uniform inflows are of the same magnitude as normal force coefficient standard deviations produced by routine turbulent inflows.

This work characterizes previously undocumented physical relationships that govern aerodynamic force time variations that take place in connection with rotational augmentation on rotating wind turbine blades. These analyses have concentrated on the principal structures underlying rotational augmentation and examined the amplitudes of aerodynamic force unsteadiness. To further improve this understanding, future work will need to dissect these structures in more detail using combined experimental and computational approaches. To gain

better resolution of physical processes through measured data, it is likely that spectral and statistical techniques could be productively applied.

10.5 Bibliography

Burton, T.; Sharpe, D.; Jenkins, N.; Bossanyi, E. (2001). *Wind Energy Handbook.* Chichester, UK: John Wiley and Sons, p. 22.

Coe, C.; Mellenthin, J. (1954). "Buffeting Forces on Two-Dimensional Airfoils as Affected by Thickness and Thickness Distribution." NACA RM A53K24.

Jonkman, B.; Buhl, M. (September 2006). *TurbSim User's Guide.* NREL/TP-500-39797. Golden, CO: NREL.

Laino, D.; Hansen, A.C. (December 2002). *AeroDyn User's Guide.* Available at http://wind/designcodes/simulators/aerodyn/AeroDyn.pdf.

Laino, D.; Hansen, A.C. (April 2003). *YawDyn User's Guide.* Available at http://wind/designcodes/simulators/yawdyn/YawDyn.pdf.

Polentz, P.; Page, W.; Levy, L. (May 1955). "The Unsteady Normal-Force Characteristics of Selected NACA Profiles at High Subsonic Mach Numbers." NACA RM A55C02.

Schreck, S.; Robinson, M. (2002). "Rotational Augmentation of Horizontal Axis Wind Turbine Blade Aerodynamic Response." *Wind Energy* (5:2/3); pp. 133–150.

Schreck, S.; Robinson, M. (2003a). "Boundary Layer State and Flow Field Structure Underlying Rotational Augmentation of Blade Aerodynamic Response," *J. of Solar Energy Eng.* (125); pp. 448–456.

Schreck, S.; Robinson, M. (2003b). "Structures and Interactions Underlying Rotational Augmentation of Blade Aerodynamic Response." AIAA-2003-0520.

Schreck, S.; Robinson, M. (January 2004). "Tip Speed Ratio Influences on Rotationally Augmented Boundary Layer Topology and Aerodynamic Force Generation." AIAA-2004-0663.

Schreck, S.; Robinson, M. (January 2005). "Unsteadiness in HAWT Blade Aerodynamic Forces and Flow Field Structures During Rotational Augmentation." AIAA-2005-0776.

Schreck, S.; Sørensen, N.; Robinson, M. (2007). "Aerodynamic Structures and Processes in Rotationally Augmented Flow Fields." *Wind Energy* (10:2); pp. 159–178.

Zell, P. (1993). "Performance and Test Section Flow Characteristics of the National Full-Scale Aerodynamics Complex 80- by 120-Foot Wind Tunnel." NASA TM 103920.

11.0 Report Conclusion

Annex XX was established in 2003 to exploit the data acquired during testing of the National Renewable Energy Laboratory (NREL) Unsteady Aerodynamics Experiment (UAE) wind turbine in the National Aeronautics and Space Administration (NASA)Ames wind tunnel. Completion of this test constituted a fundamental advance because it furnished accurate and reliable experimental measurements having high spatial and temporal resolution, for a realistic rotating blade geometry, under closely matched conditions of dynamic similarity, and in the presence of strictly controlled inflow conditions.

Over the four four year life of Annex XX, these data were used by dozens of researchers representing the eight participating countries of Canada, Denmark, Greece, The Netherlands, Norway, Spain, Sweden, and the United States. By the time Annex XX concluded in 2007, a broad variety of high quality documentation dealing with diverse aspects of wind turbine aerodynamics had been produced. The breadth of research would be difficult to capture in a reasonably brief summary. Nonetheless, some brief observations are noted here.

Canadian researchers at ETS combined a Navier-Stokes solver with the actuator disk approach. In the resulting actuator-surface model, singular surfaces are used to represent the action on the flow of the rotor blades. The recent application of the model to the case of a wind turbine using rotating surfaces demonstrated that the new model increases accuracy in the determination of the wake induction on the blade aerodynamics when compared with models based on the actuator disk representation.

In Denmark, work at Risoe National Laboratory and DTU was balanced between engineering models and CFD methods. Further refinement of the aeroelastic codes HAWC and HAWC2 considered modeling aspects including inboard stall delay, dynamic stall, yawed flow induction, and tip correction. CFD work centered around the Navier-Stokes model Ellipsys-3D, and included both Reynolds Averaged Navier-Stokes and Detached Eddy Simulation (DES) methods. CFD was applied to parked blade conditions, axisymmetric operation, correction of 2D airfoil loads to 3D, yawed flow involving dynamic stall, operation with step pitch, and downwind operation.

In The Netherlands, ECN compared UAE measurements with predictions from two codes, the aero-elastic code PHATAS and the free wake lifting line code AWSM. UAE measurements used corresponded to non-yawed flow, yawed flow and fast pitching actions. Under axisymmetric conditions for lower wind speeds, PHATAS agreed well with the measured data, as did AWSM. At higher wind speeds, PHATAS displayed some discrepancies that were attributed to three-dimensionality in the flow field, while AWSM was not used at these higher wind speeds. The investigation at yawed flow emphasized azimuthal variation of normal force due to advancing/retreating blade effect and variation in induced velocity from the skewed wake. The AWSM code does predict the above mentioned radial dependence in the azimuthal variation of the induced velocity. The resulting azimuthal variation in normal force and the consequent yawing moments agree very well with the measurements at all radial positions. The PHATAS code is slightly less accurate, but comparison of the induced

velocities, as calculated by the PHATAS and AWSM codes generally shows good agreement, even though the underlying models use different methodologies.

Also in The Netherlands, the Technical University of Delft undertook work in three related areas: 1) Analysis of the UAE measurements, 2) Angle of attack estimation from blade pressure measurements using a free-wake vortex model, and 3) Evaluation of engineering models versus CFD methods for blade rotational augmentation. In the first area, subtle but inevitable errors in UAE measurements were detected and methods were formulated for minimizing adverse impacts when analyzing the data. In the second set of studies, it was found that by using a free-wake vortex model it is possible to more accurately derive the angle of attack at the blades from blade pressure measurements in both axial and yawed conditions. In the third area, it was concluded that CFD methods, like RFOIL and FLUENT generally are reliable if carefully used and are to be preferred to conventional engineering methods.

In Norway, work focused on the investigation of 3-D behavior of the flow and analysis of steady/unsteady behavior of flow patterns at different rotor sections. To estimate stall onset and 3-D effects, a method using parts of the pressure distribution at the rotor blade (trailing edge pressure) combined with a Fourier transformation was developed. The UAE experimental data were sampled with high frequency; this allowed the use of FFT on the results and transformation of measured time series into the frequency plane. In addition, the UAE test results were further used in the modification of aero-elastic codes, which were used in the investigation of floating offshore wind turbine concepts.

At CENER in Spain, Annex XX research focused on three issues. The first was achieving an improved physical understanding of rotational augmentation for rotating blades. The second was predicting dynamic stall on parked blades, including the onset and three-dimensionality of the process, and assessment of the Beddoes-Leishman model. Finally, validation of Navier-Stokes computational tools for rotating blades was pursued, to validate commercial and in-house CFD solvers, and to create new methodologies for the use of CFD techniques at CENER.

Research in Sweden involved evaluation of existing aerodynamic simulation methods to evaluate wake flows generated by operating turbines, especially the circulation immediately downstream of the blades. A supporting objective was improved comprehension of the basic mechanisms responsible for wake breakdown, which becomes especially important when considering interactions between two or more wakes. Ultimately, the overall aim is to simulate an entire wind park. However, knowledge about suitable method, limitations in that method, basic mechanisms behind breakdown of the flow structure are necessary before setting up an advanced simulation model for a park.

Finally, in the United States, analyses of time varying surface pressure and normal force were analyzed to extract mean separation and impingement location and normal force coefficient standard deviation during axisymmetric conditions that included rotational augmentation. Complementary model predictions of time varying normal force coefficient standard deviation also were provided for turbulent inflow conditions. These results confirm that, prior

to the onset of rotational augmentation, boundary layer separation advances forward over the blade, and then impingement advances aft on the blade chord, both in response to increasing local flow angle. Forward movement of the separation point from the leading edge amplifies aerodynamic force standard deviations, but aerodynamic force standard deviations are most significantly amplified as the separation point reaches the leading edge and the flow field transitions to an impinging flow field mediated by shear layer impingement. Finally, normal force coefficient standard deviations observed for stable, uniform inflows are of the same magnitude as normal force coefficient standard deviations produced by routine turbulent inflows.

During the four year lifetime of Annex XX, participants productively used the UAE wind tunnel database in support of research that significantly improved physical comprehension of turbine flow fields. The same data were effectively exploited to enhance the accuracy and reliability of a broad range of turbine aerodynamics models. However, given the extremely complex nature of wind turbine flow fields, important opportunities remain for better understanding wind turbine fluid mechanics and for achieving more accurate and reliable modelling capabilities. Further research is needed to address these challenges, and to support the continued growth of wind energy worldwide.